Advanced modeling approaches for CFD simulations of coal combustion and gasification

Christian Hasse [a,*], Paulo Debiagi [a], Xu Wen [a], Klaus Hildebrandt [b], Michele Vascellari [b], Tiziano Faravelli [c]

[a] *Simulation of Reactive Thermo-Fluid Systems, TU Darmstadt, Otto-Berndt-Str. 2, 64287, Darmstadt, Germany*
[b] *previously Numerical Thermo-Fluid Dynamics, TU Bergakademie Freiberg, Reiche Zeche, Fuchsmühlenweg 9, 09599, Freiberg, Germany*
[c] *CMIC Department, Politecnico di Milano, Piazza Leonardo Da Vinci 32, 20133, Milano, Italy*

ARTICLE INFO

ABSTRACT

Coal is the most abundant fossil fuel and is widely used as an energy source for combustion and gasification. Both experimental methods and computational tools are required for the development of new advanced, innovative clean coal technologies and systems. In particular, 3D computational fluid dynamics (CFD) simulations can provide detailed local and global information on the interaction of fluid dynamics, mixing, and heterogeneous and homogeneous chemical reactions even for complex systems such as combustors, gasifiers, or chemical reactors. The predictive capabilities of CFD simulations depend directly on appropriate models and their mutual interactions. The current state of modeling is reviewed in this paper and the need for further improvements of both individual models and their respective coupling is addressed. In addition, to evaluate and validate the models and their interactions, systems with increasing complexity and well-defined boundary and operating conditions are required that can provide suitable experimental data. A number of reference burners and combustors, developed especially at universities and research institutions, are also presented and recent simulation data for these systems is reviewed.

1. Introduction

The industrial revolution which started in the 18th century sharply increased the demand for fuels, both in transportation and due to the mechanization of industrial activities. As a substitute for wood, coal was established as the main energy resource, primarily burned for the production of heat (and later electricity), but also essential for other industrial purposes, such as steel production.

In 2019, coal was still one of the largest sources of primary energy, making up about 22 % of the total primary energy consumption, right behind oil (30 %) and natural gas (25 %) [1]. In 2020, the global pandemic and the consequent economic crisis resulted in significant decrease in energy demand, which is expected to rise again as the world economy recovers. In particular, coal demand in 2020 is expected to have fallen 25% in the USA, 20% in Europe, 8 % worldwide and 5 % in China [2]. Nevertheless, coal remains the main source for producing electricity, generating about 36 % of the total TWh produced in 2019 [3], reaching 29–35 % by 2025 [4]. It was also one of the largest

anthropogenic energy-related sources of carbon dioxide releases in the world, responsible for about 42–44 % [5,6]. The extraction of coal, its use in energy conversion and its byproducts are all associated with effects on health and the environment, including climate change [7]. Various scenarios [8] forecast that, despite the continuous increase in renewable energy sources, coal will remain one of the main primary sources of energy in the near future (2030), making up about 20–24 % of the world usage, and its use will only decrease notably (to 5–17%) in the more remote future (2050–2070) [5,9].

Consequently, a great deal of effort has been made to develop new technologies for converting coal in a cleaner way, and further efforts will be required in the future to accompany the long transition to the new energy scenarios. The design and development of so-called *clean coal technologies* requires advanced, comprehensive tools which are able to accurately predict the performances and emissions of such systems [10, 11]. These tools can provide insights into the reaction and transport processes in the solid and gaseous phases.

Numerical simulations and especially 3D-Computational Fluid

Dynamics (CFD) can significantly contribute to this. In combination with experiments, it is possible to gain a profound understanding of coal combustion and gasification on many scales, i.e. starting from processes on the single-particle scale and moving on to particle groups, then reactors on the pilot and industrial scale. Another advantage is that different experimental and numerical methods can be systematically combined, e.g. measurements of solid kinetics can be transferred via suitable models into CFD simulations of large reactors.

The simulations' reliability depends largely on the quality of the submodels used and their coupling. Especially for turbulent combustion and gasification three particularly relevant modeling aspects can be identified:

1 Solid phase kinetics and their integration in CFD,
2 The turbulent flow and mixing field,
3 Turbulence – gas-phase chemistry interaction,

all of which are strongly coupled in coal combustion and gasification processes. However, many studies in the literature deal in detail with the development and validation of particular submodels. Only comparatively few studies have investigated the coupling. Other modeling aspects, such as radiation, that are not covered in detail in this review are briefly addressed below in Section 1.1.

The first modeling aspect is concerned with the thermochemical conversion of coal, and pyrolysis and char oxidation/gasification in particular. These are complex and strongly interlinked processes that depend not only on the molecular structure of the parent coal, but also on the gas atmosphere. To this end, a number of detailed phenomenological and empirical models have been developed. These models are mostly based on extensive experimental data.

The conditions under which this thermochemical conversion takes place are directly determined by the surrounding gas phase. While laminar flows with well-defined conditions are often investigated in laboratory setups, the flow in technologically relevant combustion chambers and reactors is turbulent. Turbulence amplifies the mass, momentum and heat exchange between the gas and the solid phase. Predicting such particle-laden reactive flows is a particular challenge, which corresponds to the second modeling aspect mentioned above.

During pyrolysis and char conversion a large number of gaseous molecules (volatiles and char off-gases) are released. These react further in the gas phase and there is a strong coupling of turbulence and gas-phase chemistry, usually referred to as turbulence chemistry interaction (TCI). TCI determines the gaseous combustion/gasification products including the pollutants; this corresponds to the third modeling aspect mentioned above.

This article reviews the current situation and recent trends for the three aspects mentioned above and especially their coupling. The solid fuel kinetics of thermochemical coal conversion is discussed in Sections 2–4. Most kinetic models have been developed separately for pyrolysis and char conversion, therefore these two processes will first be considered separately in Section 2 (pyrolysis) and Section 3 (char conversion). First the physical and chemical processes are described, then the numerical models are discussed. In Section 4, another conceptually different model developed in recent years is presented. Here, pyrolysis and char conversion are treated as fully coupled. Finally, for use in 3D-CFD, the detailed models must be coupled to the CFD; approaches developed to achieve this are reviewed in Section 5.

The second aspect is the description of the turbulent (multiphase) flow and mixing field and the coupling to the gas-phase chemistry. While Reynolds-averaged Navier–Stokes (RANS) is still the most common turbulence modeling approach especially for medium to large-scale reactors, in recent years scale-resolving methods such as large eddy simulation (LES), and in some cases even direct numerical simulation (DNS), have increasingly been used. In principle, these methods allow a better resolution of the physical processes in the gas phase, but their use for coal combustion and gasification is a particular challenge due to the

large number of interacting processes. Recent applications of scale-resolving simulations are reviewed in Section 6. The third aspect of crucial importance is turbulence–chemistry interaction. Similarly to turbulence modeling, there is a significant trend towards using advanced modeling approaches such as flamelet or transported probability density function (PDF) methods. These models were originally developed for turbulent gas-phase combustion, and must be adapted for coal, which is a very active research topic in the current literature. Recent work is reviewed in Section 6.

In addition to the development of the individual models for the solid and the gas phase, their consistent coupling is of crucial importance for reliable 3D-CFD simulations. For this purpose, the models and their coupling must be investigated under controlled and well-characterized conditions and for different scales, i.e. from the single particle scale to laboratory flames and reactors on pilot and industrial scale. The availability of reference data for model validation is crucial here. Experimental reference configurations and reactors have been developed for this purpose and are reviewed in Section 7. Finally, conclusions are given and directions for future research are outlined.

1.1. Brief discussion on additional aspects

As mentioned earlier, this article focuses on solid phase kinetics and its integration into CFD, the turbulent flow and mixing field, interaction between turbulence and gas-phase chemistry, and reference cases to investigate the interactions between the models. There are several other aspects, including radiation, slagging, fouling and fragmentation, that are also relevant to CFD modeling of pulverized coal combustion. Although a detailed discussion on these topics is beyond the scope of this paper, we briefly refer to some work in this area in this subsection.

In confined pulverized coal combustion systems, the accurate modeling of radiative heat transfer between the gas phase and the particle phase is important. Some previous studies [12–15] used the moment method developed by Cheng (i.e., the well-known P-1 model [16]). In some other studies [17–22], the discrete ordinates method (DOM) [23] is employed, in which the absorption coefficient is obtained from the weighted sum of gray gases (WSGG) [24]. Wu et al. [25] recently developed a multiphase Monte Carlo ray tracing (MCRT) radiation solver to simulate the laboratory-scale pulverized coal flame, taking into account the radiative interactions between the coal particle phase and the three major species of CO_2, H_2O and CO. They found that the flame structure and the lift-off height can be significantly affected by the radiative heat transfer.

The presence of alkali metals such as sodium (Na) and potassium (K) in coal can result in serious issues of slagging, fouling and corrosion during the long-term operation of pulverized coal combustion boilers. Many experimental studies [26–31] have been conducted on slagging and fouling characteristics and the performance of supplementary additives and co-firing with Si/Al. Wan et al. [32] conducted DNS for a pulverized coal flame with alkali metal emissions stabilized in a turbulent mixing layer, and the suitability of the flamelet tabulation method for predicting the dynamics of sodium species was evaluated through quantitative comparisons with the DNS dataset. Compared to other fields, there are only a small number of detailed 3D-CFD studies focusing on slagging and fouling.

During pulverized coal combustion, fragmentation shifts the particle size distribution towards small sizes, which affects both the conversion and heat release rates. For char conversion, it is reported that char fragmentation happens in the chemically controlled combustion regime (Regime I) [33], transition regime (Regime II) and diffusion-controlled combustion regime (Regime III) [34,35], for the discussion on the different regimes please refer to section 3.1. Besides, for high-volatile coals, fragmentation is observed in the devolatilization stage [36].

Senneca et al. [37] developed a mathematical model to predict coal fragmentation during combustion, taking into account the volatiles and char combustion within particle pores. This model can also predict the

temperature, porosity and concentration of the main chemical species within the coal particle. The simulation results indicate that the probability of fragmentation is increased when the heating rate is high, while combustion only plays a negligible role in particle fragmentation phenomena at lower and moderate heating rates. Senneca et al. [38] recently adopted the same fragmentation model to predict the fate of Colombian coal particles and the distribution of the particle size under the experimental condition in a drop-tube reactor. It was found that the fragmentation generates a 36 % population of particles with sizes close to 30 μm.

Kreutzkam et al. [39] investigated ash formation and deposition with CFD using a novel char fragmentation model. A deposition model was integrated to investigate the effect of the particle fragmentation on the slagging behavior of fly ash. It was found that the prediction of deposition can be improved with the char fragmentation model.

2. Pyrolysis

Fuel pyrolysis or devolatilization is a key sub-step in the overall conversion process [40–42]. The pyrolysis process is very sensitive to the specific coal sample showing strong variations with coal rank and even for samples of the same rank. Accurate modeling should be able to predict:

1. Pyrolysis rate of the volatiles to determine the pyrolysis duration;
2. Yield and composition of the pyrolysis products;
3. The evolution of the coal morphology toward the initial char morphology.

In the following section, the focus lies on the description of coal pyrolysis modeling, although the same methodology can also be used for the pyrolysis of other organic materials, such as wood or a multitude of waste materials [40,43]. A variety of coal pyrolysis models have been developed. These models differ considerably in their complexity and thus in their ability to predict the named objectives. In general, it can be seen that as complexity increases, the accurate prediction of the listed objectives becomes possible in the above order. Different models are summarized in several reviews [42–48]. A classification of pyrolysis models is shown in Fig. 1. The model proposed by the group from Politecnico di Milano, as discussed in Section 4, is not included here.

After a brief discussion on the physical and chemical processes during pyrolysis in Section 2.1, empirical (Section 2.2) and network pyrolysis (Section 2.3) models are presented in detail. Wherever applicable, a discussion on the specific model's capabilities to predict sulfur and nitrogen release is included.
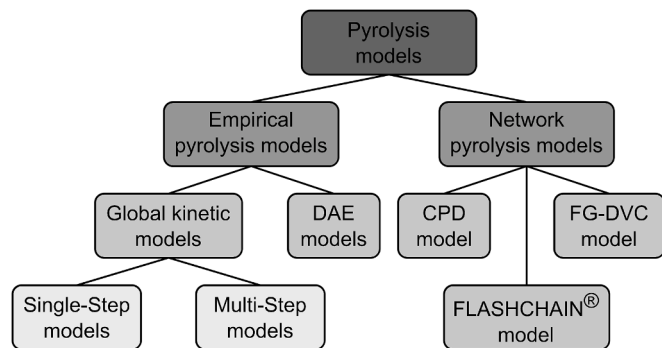

Fig. 1. Classification of pyrolysis models. The abbreviations DAE, CPD and FG-DVC refer to Distributed Activation Energy, Coal Percolation Devolatilization, and Functional Group Depolymerization Vaporization and Crosslinking, respectively.

2.1. Physical and chemical processes during pyrolysis

During the heating process, the moisture evaporates and many chemical bonds are cleaved, generating light gases and heavier fragments of finite molecular weight. Fragments with low molecular weights tend to vaporize and escape from the coal particle as tars. Volatiles with a heavy molecular weight tend to remain longer in the coal, possibly reconnecting to the solid matrix. This process involves overlapping physical and chemical steps, turning coal into a solid/metaplastic substance. In parallel, a fraction of the original coal is converted to char and the process takes place by which these nascent volatile species are transported from the coal particle to the gas phase [44]. Therefore, coal pyrolysis is a complex multi-step problem involving chemistry and transport phenomena that must be accounted for in a general, accurate description [49].

2.1.1. Initial coal structure and metaplast formation

The physical and chemical processes during pyrolysis are highly influenced by the initial coal structure [50]. Therefore, describing the physical processes which take place during coal pyrolysis first requires the initial structure of the coal to be known. A generally representative coal structure is reported in Fig. 2, showing that coal can be considered a macromolecular network structure comprising monomers of different sizes and composition, connected with each other through a variety of chemical bridges (bonds).

During the heating process, these bonds can break and new ones can be formed [44]. Because of the different nature of the monomers and the bridges connecting the parent fuel structure, the rate and the yield of species released in the pyrolysis step differs significantly from one coal to another. This first depolymerization process produces high-molecular-weight species, which are not instantly released to the gas phase [52]. They stay trapped in the coal structure, forming what is also called the metaplastic phase. This can be experimentally confirmed through extraction with pyridine, which is able to dissolve these high-molecular-weight compounds and "wash" the partially pyrolyzed coal. As the devolatilization reaches completion, the number of extractable compounds drops, showing that these compounds are heavy enough to stay trapped in the solid, but are not chemically bonded to the char. The observance of this phase is more evident in low heating rate processes, as the species in the metaplastic phase tend to devolatilize only after a certain temperature is reached. These species can also reconnect chemically to the solid matrix by repolymerization, crosslinking and reticulation reactions, which explains the higher yield of solids in processes with low heating rates. The solid structure that is formed after pyrolysis is richer in carbon and corresponds to the thermally resistant char structure. The devolatilization step leads to an increase in porosity, which depends not only on the initial fuel properties, but also on the operating conditions (heating rate, final temperature, residence time, surrounding atmosphere).

2.1.2. Primary pyrolysis

Many devolatilization models assume that the labile bonds may be broken in the pyrolysis process to yield smaller molecular fragments constituting the light gas and tar fractions [53]. Meanwhile, the formation of stable, non-labile bonds during coal devolatilization corresponds to the formation of char. The length, composition and structure of these bonds define their behavior during the thermochemical conversion. The relative yields of gas, tar, and char are governed by the reaction rates identified with these labile bond-breaking and stable bond-forming processes. After forming, these smaller fragments can remain trapped and in contact with the solid, in the metaplastic phase. The release of these fragments to the gas phase depends on the evaporation process and their transport through the porous structure of the coal. While they are trapped in the solid, repolymerization, condensation and crosslinking reactions can take place which promotes the formation of secondary char. The characteristics of the monomers after the
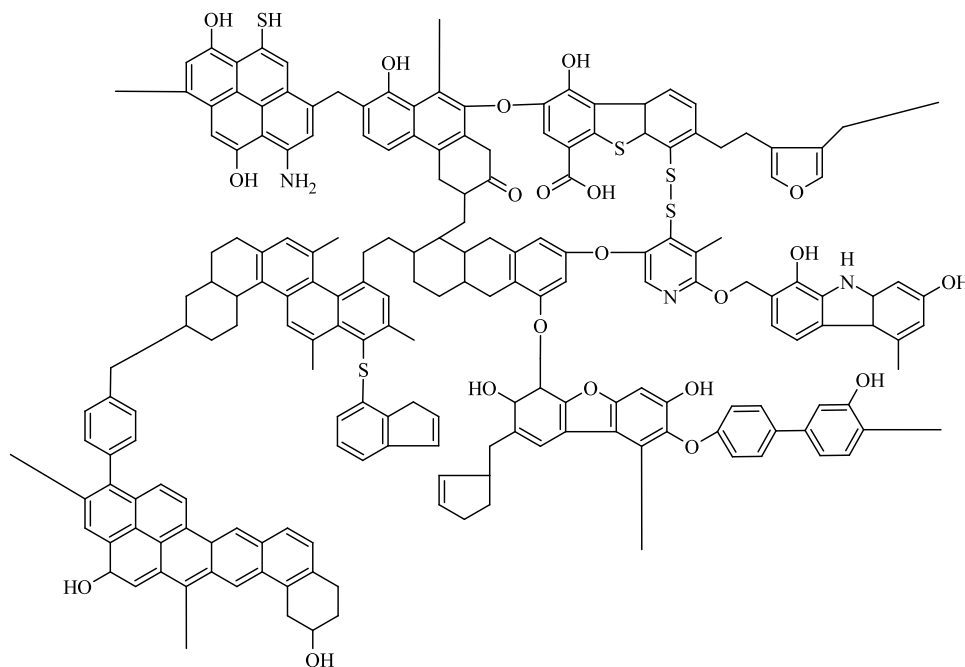
Fig. 2. General coal structure. Adapted from Davidson (1982) [51].

bonds are broken or formed define whether they will be released as volatiles or stay bonded to the char matrix.

During primary pyrolysis, elements such as sulfur and nitrogen linked to the coal structure will also be released due to the process of bond-breaking. Similar to the hydrocarbon fraction of coal, there will also be formation and release of tars and gases containing nitrogen and sulfur. Part of these atoms will also stay linked to the char structure. The release of such species is directly related to the emission of pollutants: SO_x, NO_x, and their precursors.

2.1.3. Secondary pyrolysis

The term "secondary pyrolysis" describes the gas-phase decomposition of the products released during the devolatilization step (primary pyrolysis). A large variety of volatile species are formed during coal devolatilization. Secondary pyrolysis reactions take place when these volatiles face high-temperature conditions in the gas phase. The nature of these reactions and the resulting products are strongly dependent on the temperature, residence time and the surrounding atmosphere.

In inert conditions, weaker bonds that hold large molecules together tend to break, in so-called tar-cracking reactions. From these reactions, lighter species are expected to form from larger tars. In this context, these decomposition products are subject to conditions that allow further condensation or polymerization reactions, leading to the formation of polycyclic aromatic hydrocarbons (PAHs) [54]. Growth in the size of PAH clusters leads to the formation of soot. An extensive review on soot formation in coal combustion systems was published by Fletcher et al. [54].

In oxidizing atmospheres, e.g. in combustion processes, the PAH-growth/soot-formation mechanism can be suppressed by the oxidation reactions. However, in fuel-rich regions soot (particulates) can form, e.g. caused by insufficient local mixing [55].

Also, reactions in the secondary pyrolysis involve SO_x, NO_x, and their precursors. The cracking of tars containing sulfur and nitrogen lead to formation of additional low molecular weight pollutants such as H_2S and HCN. In oxidative conditions, the volatiles containing sulfur and nitrogen primarily convert to species such as SO_2, SO_3, NO, NO_2, N_2O.

2.1.4. Char annealing

After the main devolatilization step (primary pyrolysis), the remaining metaplastic species are released, resulting in further solid mass loss and an increase in carbon content, forming the nascent char.

The remaining char can undergo further physico-chemical changes that are only possible when certain conditions are met. This process is called char thermal annealing, or char deactivation, and it is driven by very high temperatures and residence times [56]. Due to its tight coupling to the pyrolysis process, it is briefly discussed here; more details can be found in Section 3.2.4.

In the early stage, this process includes the release of residual minor elements present in the char, such as hydrogen and oxygen [57]. The late stage of this process is also called graphitization because the amorphous carbonaceous structure of char is reordered into larger ordered, stacked clusters, slowly forming more graphite-like structures, which are less reactive to oxidation and gasification.

The structural variations can be better observed in inert (pyrolysis) thermal treatments, supported by methods such as high-resolution transmission electron microscopy (HRTEM), X-ray diffraction (XRD) and Raman spectroscopy. Oberlin and coworkers [56,58,59] extensively studied this process and identified four stages during annealing until 2900 °C [59]:

- Stage 1 (<700°C): The individual scattering domains [basic structural units (BSUs)] are less than 1 nm in diameter and are isometric. They are also about 1 nm thick with 1 to 3 layers. The BSUs are randomly azimuthally distributed in the fragments. This corresponds to the release of the aromatic CH groups, reducing the hydrogen content.
- Stage 2 (700–1500°C): Begins at the end of heteroatom release. The BSUs coalesce face to face into distorted columns; the lateral coalescence is inhibited by misoriented single BSUs. This stage ends when the misoriented BSUs disappear. The number of layers reaches 8–10.
- Stage 3 (1500–2000°C): This corresponds to the release of in-plane defects. The disappearance of the misoriented single BSUs permits first a considerable increase in thickness, and then the coalescence of adjacent columns. The distortions of the layers progressively anneal. During this stage, the layers inside the columns connect edge to edge.
- Stage 4 (>2000°C): Above 2000°C, all distortions are annealed. The layers are stiff and perfect. The heteroatoms and both the interlayer

and in-plane defects have successively disappeared. Crystal growth begins.

The different stages of reorganization during thermal annealing are shown in Fig. 3. The global loss of reactivity during the reorganization is caused by a continuous reduction in the specific surface area and the destruction of active sites on the char surface, where the heterogeneous surface reactions take place. Holland et al. [60] reviewed published annealing rates developed an annealing model based on temperature and heating rate.

2.2. Empirical pyrolysis models

Empirical pyrolysis models use a small number of simple reaction rates to simulate the pyrolysis process mathematically. As shown in Fig. 1, another distinction can be made between empirical pyrolysis models using a global kinetic approach and those using a distributed activation energy (DAE) approach [48].

2.2.1. Global kinetic approach

This type of pyrolysis model is divided into Single-Step models and Multi-Step models based on the number of reaction equations used. In general, a simple reaction mechanism based on global kinetics is used. The reaction rate constants are either constant or temperature-dependent. The temperature dependency is described using the Arrhenius approach.

2.2.1.1. Single-Step models. The simplest mathematical description of the pyrolysis process is given by a Single-Step model. In this type of model, as proposed by many authors [62–66], coal, as a feedstock, reacts with the pyrolysis products in one reaction step. This simple reaction mechanism is shown in Eq. (1)

$$\text{Coal} \xrightarrow{k} \text{Char} + \text{Tar} + \text{Gas} \tag{1}$$

The simplest approach is to use a Single-Step model for coal pyrolysis, the so-called Single First Order Reaction Model (SFOM) [40] using a Single First Order Reaction (SFOR). SFOM calculates the global pyrolysis rate using Eq. (2) and Eq. (3)
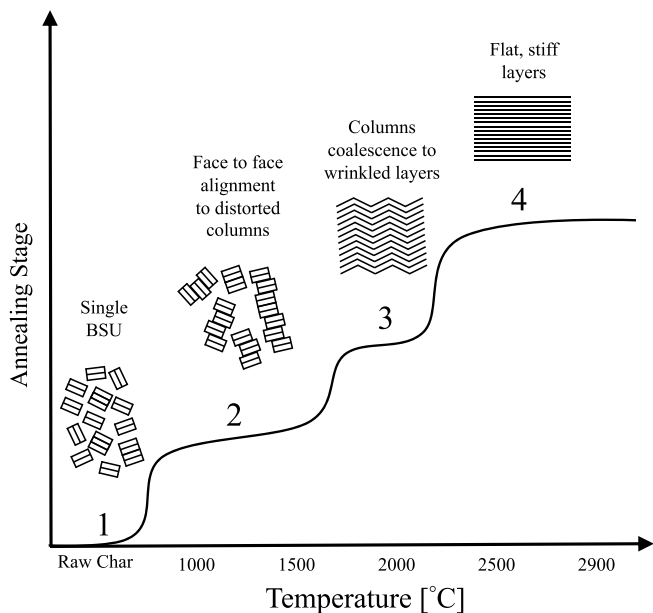
$$R = k(T_P)m_{Coal,0}(Y_0 - Y) \tag{2}$$

$$k(T_P) = AT_P^b exp\left(-\frac{E_A}{R_G T_P}\right) \tag{3}$$

with $m_{\text{Coal},0}$ as the initial raw coal mass, Y and Y_0 as the current and final yield of volatiles and t as the time, A as the pre-exponential factor, also called the frequency factor, T_P as the particle temperature, b as the temperature exponent, E_A as the activation energy and R_G as the universal gas constant.

Although the pyrolysis rate expressions of Single-Step models take into account some temperature dependency of pyrolysis using the Arrhenius approach, they are not capable of accurately reproducing the complex reaction mechanism in the coal particle, e.g. SFOM always gives the same final yield Y_0. The pyrolysis behavior modeled with Single-Step models disagrees considerably with observed pyrolysis behavior in experiments, see Yu et al. [67] and the references included. This shortcoming is caused by:

- Competing reactions activated at different temperature ranges;
- The independence of final volatile yields from distinct boundary conditions during pyrolysis such as:
- Heating rate;
- Maximum pyrolysis temperature;
- Holding time at the maximum pyrolysis temperature;
- System pressure.

2.2.1.2. Multi-step models. By using multiple reactions to describe pyrolysis, it is possible to overcome some shortcomings of Single-Step models. Multi-Step models describe the pyrolysis process using a reaction mechanism consisting of multiple reaction steps, some coupled as parallel or consecutive reactions. There are a number of possible ways to establish arbitrarily complex reaction mechanisms. Several Multi-Step models are summed up by Anthony and Howard [40].

A commonly used Multi-Step model consisting of two competing reactions is the so-called Competing Two Step Model (C2SM) [65], also known as the *Kobayashi* model. The reaction mechanism is shown in Fig. 4.

The two reactions compete with each other on the different temperature levels at which the authors describe the conversion of coal as feedstock into volatile species and char as a solid byproduct. The reaction mechanism can be described by the following two reaction equations

$$\text{Coal} \xrightarrow{k_1} (1 - \alpha_1)\text{Char} + \alpha_1\text{Volatiles} \tag{4}$$

$$\text{Coal} \xrightarrow{k_2} (1 - \alpha_2)\text{Char} + \alpha_2\text{Volatiles} \tag{5}$$

with k_1 and k_2 as reaction rate constants and α_1 and α_2 as mass specific stoichiometric coefficients describing the distribution of coal in volatiles and char. The reaction rate constants are determined using Eq. (3). The current yield of volatiles $Y(t)$ is calculated by

$$Y(t) = \int_0^t (\alpha_1 k_1 + \alpha_2 k_2)\exp\left(-\int_0^t (k_1 + k_2)dt\right)dt \tag{6}$$

The formulation of C2SM in Eqs. (4) uses different activation energies and pre-exponential factors for the two steps. The stoichiometric coefficient α_1 corresponds to the final yield of volatiles at low temperatures and is commonly set to a value comparable to the result of the

Fig. 3. Reorganization of the char structure due to thermal annealing. Adapted from [19,29].
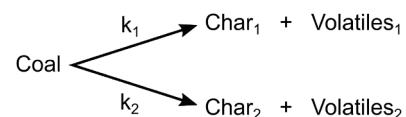

Fig. 4. Multi-Step pyrolysis models. Adapted from Kobayashi et al. [65].

volatile matter content determined by proximate analysis. In contrast, the stoichiometric coefficient α_2 corresponds to the upper border of the final yield for volatiles at high temperatures. In general, its value is close to unity [65].

2.2.2. Distributed activation energy (DAE) models

The DAE approach describes pyrolysis as a number of independent, parallel first-order reactions. Pitt [68] was one of the first to propose this type of model. He assumed that the coal structure consists of several decomposable components. Their respective decomposition reactions occur in parallel with a broad distribution of activation energies. Later, the basic concept of Pitt's approach was adapted by Anthony and Howard [40]. They determined from examination that the coal structure does not consist of different decomposable components, but is based on different decomposable chemical bonds. These chemical bonds also exhibit a broad distribution of activation energies for their decomposition reactions. Furthermore, Anthony and Howard [40] showed that the activation energy can be described by a Gaussian distribution. The advantage of this finding is the possibility of a full mathematical description of the activation energy distribution by its mean value and its standard deviation. The DAE model developed by Anthony and Howard [40] is given by Eq. (7)

$$1 - \frac{Y}{Y_0} = \int\limits_0^\infty \exp\left(-A_0 \int\limits_0^t \exp\left(-\frac{E_A}{R_G T_P}\right) dt\right) f(E_A) dE_A \qquad (7)$$

with Y and Y_0 as the current and final number of formed volatiles, A_0 as the pre-exponential factor and $f(E_A)$ as the activation energy distribution. The DAE model by Anthony and Howard [40] assumes, in addition to the idea that there are independent, parallel reactions, that:

- Every reaction has a defined activation energy with continuous distribution [69];
- The pre-exponential factor A_0 is a constant and equal for all reactions [70,71].

The latter assumption is a simplification used for mathematical modeling and is difficult to justify generally based on physical or chemical reasons.

A large number of pyrolysis experiments are necessary to determine all the required kinetic parameters for the DAE model developed by Anthony and Howard [40]. Therefore, Miura [70] developed a mechanism to reduce the required pyrolysis experiments to a minimum. The improved version of this mechanism required only three pyrolysis experiments, reported in Miura and Maki [71], which enables certain required kinetic parameters to be determined: the pre-exponential factor A_0, and the mean value and the standard deviation of the activation energy distribution. The experiments can be carried out in one experimental setup, with the heating rate changed for the three experiments.

The DAE model is also widely applied to model biomass pyrolysis, as reported by Cai and Liu [72] and Cai et al. [73,74]. Despite the efforts made to estimate the parameters associated with the DAE model, little attention has been focused on the integration step, commonly performed with standard integration algorithms that can produce relatively large integration errors [75]. Therefore, the Gauss-Hermite Quadrature method [76] was used to optimize the DAE modeling [75]. The authors report gains in computing time, the explicit estimation of integration errors and substantially improved results due to the optimization.

A series form of the DAE model was developed which avoids the complexity of the parallel formulation in Eq. (7), which assumes that the reactions with the lowest activation energy occur first, followed by reactions with higher activation energies. The series form of the DAE was first used in a network devolatilization model [44], but later applied to 1-step, 2-step, and DAE-only models [48].

2.2.3. Summary for empirical pyrolysis models

Empirical pyrolysis models are characterized by their simple reaction mechanisms. Within that field, models with different degrees of complexity have been developed. Often, only a few reaction equations are applied when describing the conversion of coal into volatiles and char. Hence, empirical models are restricted to the calculation of the formation rate for volatiles as well as a strongly simplified description of the composition and yield of the pyrolysis products. Another disadvantage of empirical pyrolysis models is the need to determine the required kinetic parameters for the Arrhenius reaction rates (the pre-exponential factor and activation energy) by carrying out pyrolysis experiments. The experimentally determined rates and product compositions are used to adapt the kinetic parameters or to derive correlations. Furthermore, based on the ultimate analysis and the elemental composition of the char, the composition of the volatiles is usually estimated to close the elemental mass balances. Based on the composition of the volatile gases, a corresponding heating value is determined. Combined with the heating value of the parent coal and the char, the heat of pyrolysis should be introduced to close the energy balance.

Therefore, it is difficult to make a generalization regarding the parameters or the correlations for a wide range of operating conditions and coal ranks, or to use them predictively for simulations [11]. One obvious advantage of the empirical pyrolysis models is that reasonable prediction accuracy can be achieved without a significant increase in computational cost. Further, they can be can be easily coupled to existing CFD codes thanks to their simplicity. A number of studies discussed in Section 6 have employed modeling approaches of this kind.

2.3. Network pyrolysis models

To overcome the limitations associated with the use of empirical pyrolysis models, a number of phenomenological approaches, so-called network pyrolysis models, have been developed for the description of coal pyrolysis. These approaches are capable of accurately describing the pyrolysis rate, as well as the yield and composition of the pyrolysis products, for a wide range of operating conditions and coal ranks.

Compared to empirical pyrolysis models, these models exhibit better flexibility, reliability and general applicability [11]. However, the utilization of network structures to describe the coal structure in a more realistic manner results in an increased computational effort because of increased complexity [40]. Therefore, detailed network pyrolysis models are less suitable for direct use in CFD calculations. The most commonly used network pyrolysis models are:

- The Chemical Percolation Devolatilization (CPD) model [44];
- The Flash-Distillation Chain-Statistics (FLASHCHAIN®) model [77];
- The Functional Group-Depolymerization, Vaporization and Cross-linking (FG-DVC) model [78];

These models share a number of common features for pyrolysis modeling including:

- Mechanisms for network modeling;
- Characterization of the coal structure;
- Depolymerization reactions;
- Crosslinking and reticulation reactions;
- Formation reactions for non-condensable gas species, tar and char [11];
- Treatment of the vapor pressure of tar precursors in the metaplast;
- Comparable simplifications to reduce the real coal structure to representative structures, including aromatic nuclei and clusters, stable, labile and charred bridges, and peripheral functional groups [11].

A schematic coal structure including the named representative structures is shown in Fig. 5. In general, the input values for coal
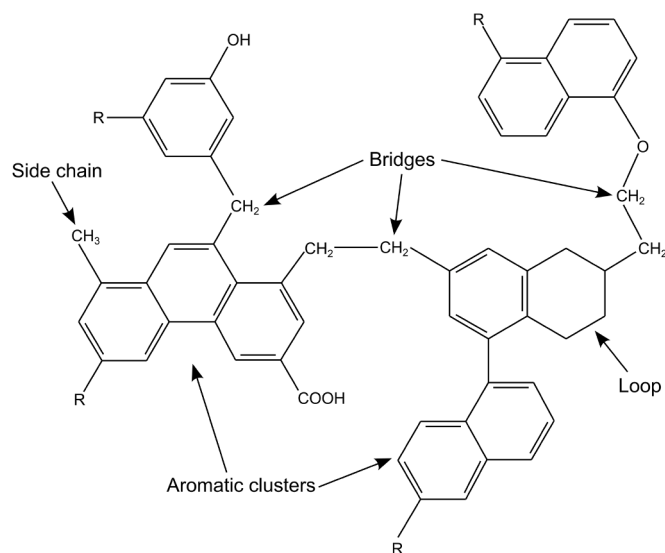
Fig. 5. Representative coal structure for network pyrolysis. Adapted from [50].

composition and structure in the models, such as the:

- Molecular weight of monomers and aromatic clusters, or the
- number of bridges and initial crosslinkings per cluster,

are determined by nuclear magnetic resonance (NMR) spectroscopy, ultimate analysis, experimental detected tar yields and the experimentally detected coal swelling behavior during pyrolysis [11].

Although the models share some similarities, their approaches and details differ concerning their application and how they model the physical and chemical phenomena occurring during pyrolysis. Especially in terms of the network models employed to interpret the interrelationships in the macromolecular lattice statistics of coal, tar and char, considerable differences are found between the individual network pyrolysis models [11].

The network models are generally able to describe devolatilization rates and yields as a function of coal type, temperature, heating rates, and pressure. In the following subsections, the network pyrolysis models are discussed in detail.

2.3.1. Chemical percolation devolatilization (CPD) model

The CPD model was originally proposed by Grant et al. [44]. Later, it was extended and enhanced by Fletcher et al. [50,52,79]. Of the three network pyrolysis models presented here, CPD is the only one distributed as open source code [80]. Percolation theory is used as a statistical method to describe the coal lattice [50,79]. The coal lattice is approximated using a three-dimensional Bethe lattice. Bethe lattices are defined by two parameters:

- The coordination number;
- The fraction of intact bridges [41].

In addition, an extrapolation method taken from Solum et al. [81] is necessary to describe the coal lattice. The standard version of CPD is capable of predicting the formation rates and the yields of char, tar and gaseous species. However, it does not provide information about the compositions of tar and gas species, which are of high relevance for heterogeneous and homogeneous reactions during secondary pyrolysis. Genetti et al. [82] improved CPD by adding empirical correlations derived from data collected by Solomon et al. [83] and Chen and Niksa [84] to estimate the composition of light gases. Further improvements to the prediction of the light gas composition with CPD have been made by Jupudi et al. [85]. They use a more reliable and accurate method

describing the evolution of light gas species from corresponding functional groups during pyrolysis with individual rate equations for each gas species examined, e.g. CO, CO_2, H_2O, HCN, aliphatic hydrocarbons etc. The approach, also used in the FG-DVC model [78], requires a modification of the standard CPD reaction mechanism [85]. In addition, a 2D interpolation method, also taken from the FG-DVC model [78], is implemented in the advanced CPD model to provide the initial functional group composition of the parent coal as an input for the improved reaction mechanism [85]. Another improvement to CPD has been reported by Umemoto et al. [86]. Their extended version of CPD is capable of predicting the yield not only of individual gas species but also of individual tar species. In addition, they couple a detailed gas phase chemistry mechanism to CPD to account for secondary pyrolysis, as well as polymerization reactions in the gas phase. Furthermore, elementary step reaction models or their simplified versions are added to predict hydrocarbon polymerization. The overall goal of Umemoto et al. [86] is to correctly predict the yield of polycyclic aromatic hydrocarbons (PAHs) formed during primary and secondary pyrolysis, because PAHs are soot precursors. Since soot formation decreases the carbon conversion in coal gasification [87], it is important to account for the first steps of the formation mechanism in primary pyrolysis [88].

Although the CPD model was originally developed for coal pyrolysis, in the last two decades it has been extended and applied to other feedstocks such as black liquor, biomass and polyurethane foam, as well as shale oil pyrolysis, which is discussed in a recent review article [47]. In the following, the underlying theory of CPD is presented.

1. Pyrolysis process in CPD

The description of the pyrolysis process in the CPD model follows Eaton et al. [11]. CPD reduces the manifold physical and chemical processes occurring during coal pyrolysis to a simplified model conception. The basic assumption is that the labile bridges between the aromatic clusters decompose. Regardless of whether the bridges are of a linking, movable or breakable type, the conversion of bridges results in the formation of two classes of fragments. This fragmentation of the macromolecular coal structure, also called depolymerization, is mostly thermal in cause.

The first class of fragments consists of tar precursors characterized by a relatively high molecular weight and a correspondingly low vapor pressure. Aromatic clusters unlinked from the coal lattice are in this class, in particular. The tar precursors tend to remain longer in the coal lattice under typical pyrolysis conditions. By contrast, the other class of fragments is characterized by a low molecular weight and an accordingly high vapor pressure. These fragments leave the coal particle immediately as light non-condensable gases.

During the pyrolysis process the coal lattice and the high molecular fragments form a viscoelastic fluid together, the so-called metaplast. The fragments of both classes are transported through the metaplast to the outer surface. Thereby, new connections between fragments and the coal lattice are possible. The softening behavior of the coal particle is defined by the amount and properties of the metaplast formed during pyrolysis. The fraction of the original coal lattice structure remaining after pyrolysis forms the new char lattice consisting of carbon and ash.

2. Coal lattice

The complex coal lattice is reduced to aromatic clusters linked by chemical bridges utilizing a simple lattice network [11]. This simple lattice network is described by lattice statistics. The importance of lattice statistics for modeling coal pyrolysis and the concurrent decomposition of labile bonds, as well as the forming of char bridges, were originally discovered by Niksa and Kerstein [89–92] using lattice statistics and by Solomon et al. [78] using Monte-Carlo simulations. Their work on coal pyrolysis has shown that many mechanistic features of the time-dependent conversion of the coal macromolecule into molecular fragments are based on lattice statistics. Percolation theory provides a mathematical expression for the statistics of bridge decomposition

during pyrolysis. The use of percolation theory is less time consuming compared to Monte-Carlo methods. However, many significant statistical properties of the lattice can be reproduced [50].

3. Percolation theory

This paragraph summarizes the discussion on percolation theory by Niksa and Kerstein [91,92] and Fletcher et al. [50]. Percolation theory analytically describes the size distribution of finite clusters of sites connected by intact bridges but separated from all remaining sites by broken bridges. Moreover, a critical bridge population is defined by the theory, depending only on the site coordination number above which infinite arrays will coexist with fragments of finite size. The adaptation of structural features of percolation theory to coals, as well as the product char-tar pairs obtained during pyrolysis, is a relatively simple matter. The infinite arrays of percolation theory represent macroscopic lattices of unreacted coal and/or char, while the finite fragments of percolation theory characterize relatively small tar molecules. The non-linear relationship between the distribution of finite fragments and the fraction of broken bridges is a significant feature of lattice statistics. This leads to interesting implications in coal pyrolysis. An ongoing discussion about the importance of lattice statistics and the utilization of percolation theory for coal pyrolysis is found in Fletcher et al. [50].

4. Bethe lattices

Bethe lattices are briefly summarized here based on the comprehensive discussion by Fletcher et al. [50]. In general, the statistics of real two- and three-dimensional arrays cannot be described analytically because sites and bridges are looped within the lattice. However, a class of pseudo-lattices, so-called Bethe lattices, can be solved analytically based on percolation theory. These Bethe lattices are similar to standard lattices with respect to the possible characterization by a coordination number and a bridge population parameter. However, in contrast to standard lattices, any two sites in a Bethe lattice are only connected by a single path of bridges and sites. The abstraction of a real honeycomb lattice using a trigonal Bethe lattice is shown in Fig. 6. The presence of loops in standard lattices results in the possible connection of two sites by more than one bridge and so prevents the description of lattice statistics in a closed form. Due to these features, more computationally extensive Monte-Carlo methods are normally required. Nevertheless, the mathematical constructs of percolation theory, as applied to this class of pseudo-lattices, have repeatedly proven a successfully means of representing the properties of real lattices under certain conditions. The Bethe lattices and real lattices have many properties that are similar for problems where only the smaller finite clusters and the infinite arrays are important. With increasing coordination numbers, the differences in the statistics between real and pseudo-lattices increase. However, when a coal lattice is approximated using Bethe lattices this issue is less significant. Carbon atoms in a coal matrix representing the sites in lattices can only form four bridges to other atoms (sites). Therefore, the coordination number for a lattice abstracting the coal matrix is four. This is
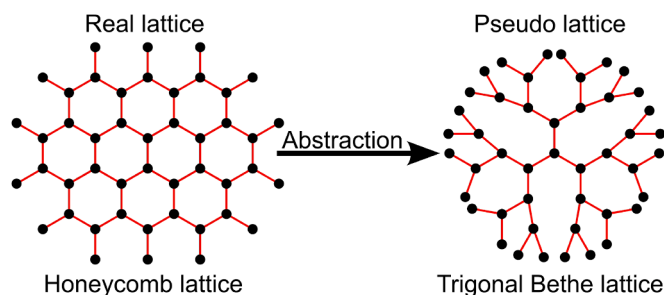

Fig. 6. Abstraction of real lattice using a pseudo-lattice (the black circles represent sites linked with each other by bridges marked as red lines). Adapted from [50].

still in the confidence region for using a pseudo-lattice instead of a standard lattice with the same coordination number.

5. Reaction mechanism

Here, the standard reaction mechanism of CPD is briefly explained; more details are given in Fletcher et al. [50]. The improved reaction mechanism of the advanced CPD version is explained in Jupudi et al. [85]. The standard mechanism, see Fig. 7, has four reaction steps describing the fragmentation of the coal matrix into two classes of fragments due to the decomposition of labile bridges and the formation of light non-condensable gases, tar precursors and char [50]:

1. Relatively slow formation of a reactive intermediate species ξ* by the breaking of a chemical bond in a labile bridge;
2. Release of light non-condensable gas species g_2 with simultaneous recombination of two corresponding sites in the lattice, forming a charred bridge c (first parallel reaction of intermediate species ξ*);
3. Formation of a side chain δ due to the stabilization of the reactive intermediate species ξ* (second parallel reaction);
4. Possible reactive conversion of a stabilized side chain δ into light non-condensable gas species g1 with a subsequent slower reaction.

The mathematical equations to describe the CPD reaction mechanism are published in several papers [11,44,50]. The formation and consumption rates for the individual species in the reaction mechanism are summed up in Eqs. (8) - (16). The relatively slow conversion of a labile bridge ξ into a reactive intermediate species ξ* is described by Eq. (8)

$$\frac{d\xi}{dt} = -k_b \xi \tag{8}$$

The change in the reactive intermediate species ξ* is the sum of the formation and consumption reactions for this species, as shown in Eq. (9)

$$\frac{d\xi^*}{dt} = k_b \xi - (k_\delta + k_c)\xi^* \tag{9}$$

Assuming that all the reactive intermediate species ξ* which are formed continue reacting immediately, the required equations for describing the formation of all pyrolysis products can be derived. This assumption describes a steady state between the production and consumption of the reactive intermediate species ξ*, shown in the following equation

$$\frac{d\xi^*}{dt} = 0 \tag{10}$$

It is thus possible to derive a formulation for the availability of the reactive intermediate species ξ*, as shown in Eq. (11)

$$\xi^* = \frac{k_b \xi}{(k_\delta + k_c)} \tag{11}$$

The production rate for charred bridges c is calculated using the expression for the reactive intermediate species ξ* from Eq. (12)

$$\frac{dc}{dt} = k_c \xi^* = \frac{k_c k_b \xi}{(k_\delta + k_c)} = \frac{k_b \xi}{(\rho + 1)} \tag{12}$$

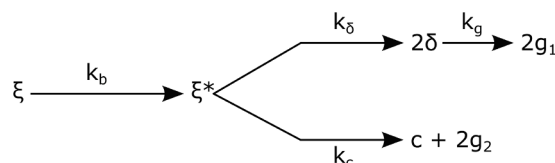Additionally, the ratio ρ between the reaction rate constants k_δ and k_c

Fig. 7. Reaction mechanism of the CPD model. Adapted from [50].

Table 1

Coal-dependent input parameters for coal composition and coal structure in CPD [50].

Parameter	Description	Determination
p_0	fraction of intact bridges	^{13}C-NMR spectroscopy
M_{Cl}	average molecular weight of aromatic cluster	^{13}C-NMR spectroscopy
M_δ	average molecular weight of side chains	^{13}C-NMR spectroscopy
$\sigma + 1$	coordination number of lattices	^{13}C-NMR spectroscopy
f_a'	^{13}C aromaticity	^{13}C-NMR spectroscopy
AC/Cl	aromatic carbon per cluster	^{13}C-NMR spectroscopy
c_0	Initial number of char bridges	empirical or fitting parameter
C	fraction of carbon	ultimate analysis

is introduced in Eq. (13)

$$\rho = \frac{k_\delta}{k_c} \tag{13}$$

The change in the side chains δ is the sum of the formation rate for side chains and the consumption rate with the formation of non-condensable gas species g_1 as shown in Eq. (14)

$$\frac{d\delta}{dt} = 2k_\delta\xi^* - k_g\delta = \left[\frac{2k_\delta k_b\xi}{(k_\delta + k_c)}\right] - k_g\delta = \left[\frac{2\rho k_b\xi}{(\rho + 1)}\right] - k_g\delta \tag{14}$$

Eq. (15) and Eq. (16) show the formation rates for the non-condensable gas species g_1 and g_2 formed during the conversion of side chain δ or the formation of charred bridges c out of the reactive intermediate species ξ^*

$$\frac{dg_1}{dt} = k_g\delta \tag{15}$$

$$\frac{dg_2}{dt} = 2\frac{dc}{dt} \tag{16}$$

All the reaction rate constants k_i ($i = b, \delta, g, c$) in Equations. (8) - (16) are described by the Arrhenius approach, shown in Eq. (3).

6. Input parameters of CPD

Two types of input parameters are necessary to use the CPD model:

1 coal-dependent structural and composition parameters [79];
2 coal-independent kinetic parameters [50].

To determine the coal-dependent structural parameters in CPD, solid-state ^{13}C-NMR spectroscopy measurements are necessary [41]. These input parameters are summed up in Table 1.

To avoid the experimental determination of coal-dependent structural parameters using ^{13}C-NMR spectroscopy for CPD, Genetti [93] and Genetti et al. [82] developed a set of correlations for calculation based on ultimate analysis and the ASTM volatile matter content.

Table 2 sums up the coal-independent parameters for the pyrolysis kinetic in CPD. The series form of the DAE model (rather than the parallel form) is used for bridge-breaking and light gas release.

A nitrogen release submodel was developed and implemented into the CPD framework in [94–96]. Nitrogen is characterized based on the chemical structure of coal as measured by ^{13}C NMR spectroscopy, which allow model predictions to be compared not only with nitrogen release data, but also with structural characteristics derived from available ^{13}C NMR measurements of char structure. The CPD nitrogen submodel accounts for the release of coal nitrogen in two different ways: (1) The weaker-bonded nitrogen is released as nitrogen-containing tar, which was modeled by modifying the CPD model to calculate this quantity at each calculation time step. (2) The fraction of stable nitrogen in coal, which progressively increases with coal rank, is released as HCN, described by a first order rate expression with a DAE model.

2.3.2. FLASHCHAIN®

FLASHCHAIN® has been developed by Niksa and Kerstein since the early 1980s, see chapter 5 in [42]. They have published the different development steps for the model in a series of papers [77,97,106, 98–105]. A summary of publications concerning the development of FLASHCHAIN® is also given in chapters 5, 7, 9 in [42]. Basically, FLASHCHAIN® combines three predecessor models:

1 the FLASHTWO model, also called the FLASH2 model [107];
2 the DISCHAIN model [89,90];
3 the DISARAY model [91,92].

The FLASHTWO model is used to describe the formation of char, tar, and light non-condensable gas species taking into account the pressure influence [77]. The DISCHAIN model is employed for the conversion of labile bonds using bridge scission and the formation of peripheral groups by applying kinetic mechanisms and chain statistics [77]. In FLASH-CHAIN®, the crosslinked three-dimensional char molecule is reduced to linear chain statistics and pseudo-components. An estimation of the qualitative influence of the macromolecular network is not performed [11]. Basically, the DISARAY model provides the same functions as the DISCHAIN model, the difference being that Bethe lattices are employed instead of linear chain statistics [11].

1. Reaction mechanism

The kinetic mechanism of FLASHCHAIN® describes the pyrolysis process in four steps [108]:

- Decomposition of the coal macromolecule into primary fragments with a broad particle size distribution;
- Reaching the phase equilibrium for tar in the metaplast and gas phase additionally to the removal of tar from the gas phase by convection, neglecting mass transfer resistance;
- Reactions in the condensed phase:
- Conversion of labile bridges into charred bridges and simultaneous prevention of further polymerization reactions;
- Formation of non-condensable gases causing convection and promoting the formation of intermediate tar products;
- Recombination reactions in the condensed phase and formation of non-volatile char species.

A graphical display of the FLASHCHAIN® reaction mechanism is

Table 2

Coal-independent kinetic parameters in CPD [50].

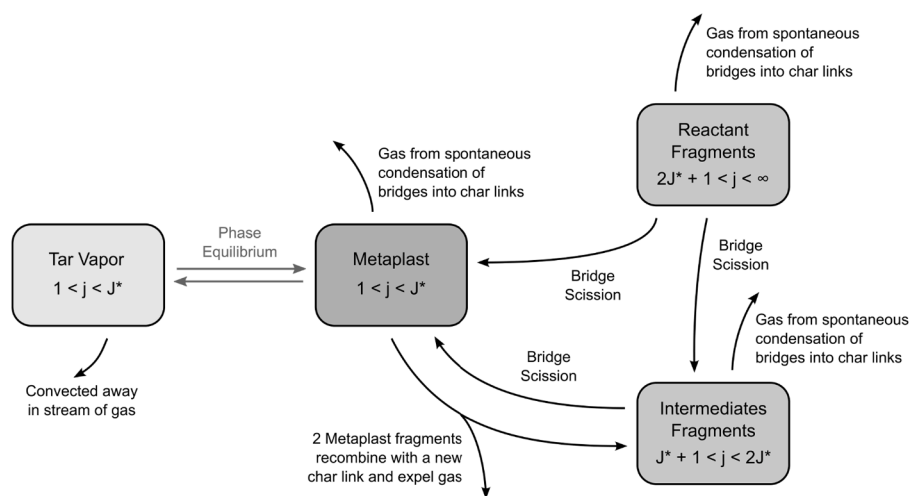| Parameter	Description	Value
E_b	activation energy for bridge scission	55.4 kcal/mol
A_b	pre-exponential factor for bridge scission	2.6×10^{15} s^{-1}
σ_b	standard deviation for E_b	1.8 kcal/mol
E_g	activation energy for light gas release	69 kcal/mol
A_g	pre-exponential factor for light gas release	3×10^{15} s^{-1}
σ_g	standard deviation for E_g	8.1 kcal/mol
ρ	ratio between reaction rate constants	0.9

Fig. 8. Reaction mechanism of the FLASHCHAIN® model. Adapted from [77].

Table 3
Input parameters for coal composition and structure in FLASHCHAIN® [77].

Parameter	Description	Determination	Remark
C	fraction of carbon	ultimate analysis	
H	fraction of hydrogen	ultimate analysis	
O	fraction of oxygen	ultimate analysis	
N	fraction of nitrogen	ultimate analysis	
S	fraction of sulfur	ultimate analysis	
f_a'	^{13}C aromaticity	^{13}C-NMR spectroscopy	x
AC/Cl	aromatic carbon per cluster	^{13}C-NMR spectroscopy	x
$^{H}f_a'$	^{1}H aromaticity	^{1}H-NMR spectroscopy	x
C_T	carbon atoms in monomer	f_a', AC/Cl	
C_A	carbon atoms in nucleus	f_a', $^{H}f_a'$, AC/Cl	
C_B	carbon atoms in labile bridges	f_a', $^{H}f_a'$, AC/Cl	
C_C	carbon atoms in charred bridges	f_a', $^{H}f_a'$, AC/Cl	
MW_A	molar mass of nucleus	f_a', $^{H}f_a'$, AC/Cl	
MW_B	molar mass of labile bridges	f_a', $^{H}f_a'$, AC/Cl	
MW_C	molar mass of charred bridges	constant fraction of MW_B	
MW_G	molar mass of non-condensable gases	regression (see [77])	x
p(0)	probability of intact bridges	pyridine extract yields	x
F_0^b	fraction of labile but intact bridges	C or fitting parameter	x

Table 4
Input parameters for the pyrolysis kinetics in FLASHCHAIN® [77].

Parameter	Description	Determination	Remark
v_B	selectivity for bridge scission	correlation	
A_B	pre-exponential factor for bridge scission	correlation	
E_B	activation energy for bridge scission	correlation	
σ	standard deviation of E_B	correlation	
A_R	pre-exponential factor for recombination	correlation	
E_R	activation energy for recombination	correlation	
A_G	pre-exponential factor for elimination of peripheral groups	fitting parameter	
E_G	activation energy for elimination of peripheral groups	fitting parameter	
v_C	stoichiometric coefficient	MW_G	x
v_E	stoichiometric coefficient	MW_G	x
P_c	pre-exponential factor for P^{sat}	Same for all coals	
A	parameter for P^{sat}	Same for all coals	
z	parameter for P^{sat}	Same for all coals	

given in Fig. 8.

2. Input parameters of FLASHCHAIN®

Two types of input parameters are necessary to operate the FLASH-CHAIN® model [77]:

- Structural and composition parameters for the coal and
- Kinetic parameters for coal pyrolysis.

Coal-dependent and coal-independent values exist for the kinetic parameters, while the coal structural parameters are all coal-dependent. The input parameters for coal composition and structure as well as pyrolysis kinetics are evaluated from only the proximate and ultimate analyses and internal databases of analytical data, such as ^{13}C NMR parameters and extract yields in pyridine. The parameters are summed up in Table 3 and Table 4, respectively.

All the coal structural parameters marked with an "x" in Table 3 can be determined using a submodel in FLASHCHAIN®, with the results of the coal's ultimate analysis as an input [98]. The results of the submodel are used to calculate additional structural parameters from Table 3.

The kinetic parameters marked with an "x" in Table 4 are coal-dependent. Using the submodels implemented in FLASHCHAIN® to determine the required input parameters, the model does not require measurements obtained by NMR spectroscopy [98] for every coal sample. Correlations for all the parameters in Table 4 have been reported [99]. In addition, FLASHCHAIN® is integrated into the commercial software package PC Coal Lab® distributed by Niksa Energy Associates LLC (NEA) [108], and is continuously updated as new devolatilization datasets are reported.

A submodel for the release of nitrogen was proposed and implemented in FLASHCHAIN® in [101]. Nitrogen content, being primarily present in coal in cyclic structures such as pyrrolic and pyridinic, was attributed to the aromatic clusters. Quaternary nitrogen is present in appreciable amounts only in low-rank coal, where it would be considered part of the labile bonds. Two mechanisms describe the release of nitrogen. The first mechanism accounts for formation and evaporation of tar containing nitrogen from the weaker bonded clusters. Tar release rate and yields are aligned to the release of other tars, which is correlated to the coal rank. The second mechanism accounts for the direct release of HCN from stable clusters at high temperature, in a process analogous to char graphitization that releases H_2. The FLASHCHAIN® also accounts for successive cracking of N-containing tars in the gas-phase, forming additional HCN.

More recently, the release of sulfur was proposed and implemented in FLASHCHAIN® in [103], where sulfur content was characterized in different forms: organic (S_{ORG}), pyritic (S_{PYR}) and sulphatic (S_{SO4}). In case such details of the sulfur distribution are not available, correlations are proposed to characterize sulfur into these three forms. Organic sulfur fraction is estimated as a function of the coal proximate analysis, which is distributed into three organic functionalities: S_{AL} (aliphatic), S_{AR} (aromatic) and S_{TH} (thiophenic), and their amounts are obtained as a function of the coal rank. Pyritic sulfur is estimated using the correlation of Strugala [109]. For sulphatic sulfur, they attribute a fixed value of 7% of the coal sulfur. They highlight that the release of sulfur can only be accurately interpreted if the distribution of the sulfur functional groups is correctly specified. The organic sulfur functionalities S_{AL} and S_{AR} were correlated to labile bridges and peripheral group, with release kinetics associated to the coal sample-specific parameters. The release of sulfur from decomposition of S_{TH} is described by a single distributed-energy reaction.

The FLASHCHAIN® approach was recently extended to tar decomposition during secondary pyrolysis [104] to describe tar decomposition into additional non-condensables, oils, and PAH at moderate temperatures, and the subsequent nucleation and condensation of oils and PAH into soot [104] at higher temperatures. Versions are also available for any biomass form [110], pet coke, black liquor, and petroleum

asphaltene.

2.3.3. Functional group-devolatilization, vaporization and crosslinking (FG-DVC) model

FG-DVC has been developed by Solomon et al. [78] since the early 1980s using the theory of functional groups. The theory of functional groups was developed by Gavalas et al. [111,112]. The FG-DVC model is an extensive pyrolysis model aiming at the prediction of many general trends during coal pyrolysis [78], such as:

- The formation rate of individual species is independent of the parent coal rank;
- Product yields are dependent on the coal rank and correlate with the parent coal's composition with regard to the functional groups;
- Similarity between the primary tar composition and the parent coal's composition for bituminous and rapidly heated low rank coals;
- Dependence of the tar yield on the amount of released H_2 and its chemical conversion;
- Correlation between the crosslinking and the formation of CO_2 and CH_4.

Similarly to FLASHCHAIN®, FG-DVC consists of two predecessor models:

1. The FG model, describing the decomposition of coal and char under the formation of gas species and other volatile components, and
2. The DVC model, describing the formation of tar species based on statistical methods.

Monte-Carlo methods are employed in the DVC model [78]. They are used for the mathematical description of coal lattices and their conversion during pyrolysis. The real lattice is abstracted by a two-parameter Bethe lattice [11]. Both predecessor models are extensively described by Solomon et al. [78] and the references therein.

Both predecessor models are characterized by a number of assumptions used to describe their sub-process of pyrolysis. The assumptions of the FG model are [78]:

- Formation of light gas species by decomposition of specific functional groups using first-order reaction rates based on the Arrhenius approach with distributed activation energies (Gaussian distribution);
- Thermal scission of bridge structures in the coal under formation of light gas species and simultaneous release of molecular fragments serving as an image of the functional groups and operating as tar precursors during transport to the particle surface;
- Execution of pyrolysis of functional groups in tar and char with the same reaction rates under specific operating conditions defined by high temperatures for the pyrolysis products as in an entrained-flow reactor.

For the DVC model, the following assumptions are of importance [78]:

- Input parameters are defined which are appropriate to the experimentally determined results for calibration;
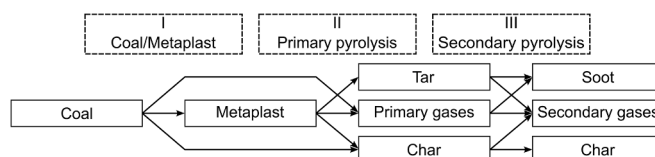

Fig. 9. Reaction mechanism of the FG-DVC model. Adapted from Yu et al. [67].

- Distribution of molar masses in the model is set to correspond to the real molar mass distribution of the coal determined by a pyrolysis experiment;
- Random scission of bridges during pyrolysis is based on an Arrhenius approach with Gaussian distribution under formation of two radicals reacting with labile and available hydrogen to form methyl and aromatic CH groups;
- Available hydrogen only appears in labile bridges and these are converted into stable bridges (double bond) through the consumption of available hydrogen;
- Tar is formed after the complete consumption of all available hydrogen;
- Formation rate for additional stable crosslinkings is determined by the formation rates of CO_2 and CH_4;

Crosslinkings are randomly distributed with a probability for attachment to an arbitrary monomer proportional to the molar mass of the monomer;

- Use of vapor pressure correlation proposed by Suuberg et al. [113] for the tar molecules;
- Empirical equation is used to describe the internal transport of tar by bubble transport or convective transport through pores in softening, plastic coals as well as in non-softening coals, respectively;
- Surface evaporation model proposed by Unger and Suuberg [114] is used to describe the external transport;
- Sole existence of molecules extracted with the help of pyridine with a molar mass lower than 3000 g/mole (adjustment of arbitrary limit according to the solvent and extraction conditions);
- Molar mass of the crosslinkings is calculated as the ratio between the total molar mass of the model molecules and the total number of crosslinkings.

1. Reaction mechanism

The different processes taking place during coal pyrolysis in the FG-DVC are summed up in three steps [78]:

   I Simultaneous formation of tar and gas species and concurrent release of labile bridges in the tar, conversion into peripheral groups or adding as stable bridge to aromatic clusters;
   II End of tar formation after complete conversion of labile bridges;
   III End of pyrolysis after complete conversion and release of all volatile functional groups from the formed char.

The reaction mechanism is represented graphically in Fig. 9.

2. Input parameters of the FG-DVC model

Compared to the other network models, FG-DVC requires the most input parameters, corresponding to its complexity. Similar to the other network models, it is possible to classify the input parameters into two groups:

1 Parameters describing the coal structure and composition;
2 Kinetic parameters describing the kinetic rates.

Fourteen different parameters are used to describe the coal structure, while the elementary mass fractions are used to determine the coal composition, as shown in Table 5.

Several experiments are required to determine the named structural and composition parameters in Table 5, e.g.:

- determination of yields for tar, CO_2 and CH_4 using pyrolysis experiments,
- extraction experiments with pyridine as solvent and
- field ionization mass spectroscopy (FIMS) or NMR spectroscopy.

Therefore, determining structural parameters for FG-DVC involves a considerable amount of work and can only be carried out in a specialized laboratory.

The kinetics of the reaction mechanism use twenty reactions. The reaction rate constants k_i are described with the Arrhenius approach, shown in Eq. (3), modified by the use of a distribution for the activation energy. The activation energy distribution is described by a Gaussian distribution [78]. Therefore, the twenty reactions examined in the mechanism require not only parameters for the pre-exponential factor but also the mean value and the standard deviation of the activation energy distribution. In a later publication, Solomon et al. [115] present an extensive summary of coal structure parameters and kinetic parameters for FG-DVC.

In the framework of the FG-DVC, sulfur release was introduced in [116]. The content of sulfur was divided into a number of the so-called precursor pools that evolve during pyrolysis with different kinetics. The evolution of each pool is modeled using a distributed activation energy approach to represent the diversity of the chemical structure of coals. The pool accounting for sulfur released as tar was introduced and the rate of release was modeled with the FG-DVC tar evolution algorithm. The organic fraction of sulfur in the coal is described as aliphatic sulfur

Table 5
Input parameters for coal structure and composition in the FG-DVC model [78].

Parameter	Description	Determination
W_B	mass fraction of labile bridges	tar yield of pyrolysis experiment
W_N	mass fraction of nuclei	parameter taken from FG model
W_P	mass fraction of peripheral groups	$1 - W_B - W_N$
H(al)	mass fraction of available hydrogen	$(2/28) W_B$
l	oligomer length	yield of extract, experimental
M_{ct}	molar mass of crosslinkings	literature or experimental
m_0	number of crosslinkings per monomer	M_{av}/M_{ct}
m_{CO_2}	number of potential CO_2 crosslinkings	parameter taken from FG model
m_{CH_4}	number of potential CH_4 crosslinkings	parameter taken from FG model
M_L	molar mass of labile bridges	constant value ($M_L = 28$ g/mole)
$M_{av}(\sigma)$	molar mass of monomers with a standard deviation σ	experimental, FIMS or NMR spectroscopy
M_{NL}	molar mass of stable bridges	constant value ($M_{NL} = 26$ g/mole)
M_{PS}	molar mass limit for pyridine extraction	adjustable value ($M_{PS} = 3000$ g/mole)
ΔP	inner pressure	fitting parameter
C	fraction of carbon	ultimate analysis
H	fraction of hydrogen	ultimate analysis
O	fraction of oxygen	ultimate analysis
N	fraction of nitrogen	ultimate analysis
S	fraction of sulfur	ultimate analysis

(loose), aromatic sulfur (tight), and char sulfur. While aliphatic and volatile aromatic sulfur are released during pyrolysis as H_2S, char sulfur remains in the char. Inorganic sulfur is considered only as pyritic sulfur (FeS_2), while sulphatic sulfur content is neglected. Half of the sulfur content in pyritic sulfur is released as H_2S, while the other half remains in the solid phase as FeS. The experiments used in the model development detected only traces of OCS and SO_2 released during pyrolysis, and these gases were, therefore, neglected.

Nitrogen release was also introduced to the FG-DVC in [116]. The content of nitrogen is also divided into precursor pools, which evolve with different kinetics during pyrolysis. They describe the direct release of nitrogen from coal as nitrogen-containing tar using their tar evolution algorithm. Nitrogen is also released directly from coal as HCN accounted for with first order kinetics and DAE model. The model describes only a very limited amount of NH_3 formed and released directly from coal pyrolysis. Higher amounts of NH_3 formation are modeled as the result of a successive reaction mechanism, which marks the novelty of the FG-DVC modeling approach for nitrogen release. The mechanism consists in the formation of NH_3 from heterogeneous reaction of HCN with the hydrogen present in coal. This mechanism explains why NH_3 formation is only observed at low heating rates, since residence times of HCN within the pore structure are longer in such conditions. Since this mechanism is strongly dependent on the residence time of HCN within the pores, it requires a proper description of the char, the presence of hydrogen in the char and the mass transfer of the gas species.

2.3.4. Summary of network pyrolysis models

In general, network pyrolysis models are characterized by a very complex description of the coal structure and the reaction mechanism. The real coal lattice is approximated by lattice statistics. In CPD and FG-DVC, Bethe lattices are used as pseudo-lattices, while in FLASHCHAIN® chain statistics and pseudo-components are employed [11]. Such approaches enable a more comprehensive examination of the coal structure consisting of:

- Aromatic clusters;
- Stable and labile bridges between the clusters;
- Functional groups in a peripheral position [11].

The more comprehensive examination of the coal structure has a direct influence on the reaction mechanism. The reactive conversion of specific structural groups is described by smaller subordinated mechanisms. As several reactants (structural groups) are taken into account in the reactions, the spectrum of included pyrolysis products is wider. Because of its higher complexity compared to empirical pyrolysis models, as well as offering accurate information on the pyrolysis rate, the network pyrolysis models are capable of providing detailed information about the yield and composition of the pyrolysis products. Additionally, the mechanistic approach used for the evolution of the coal structure during pyrolysis makes it possible to derive specific information about the developed char structure. However, the increased amount of detailed information about coal pyrolysis is accompanied by a considerably increased computational effort. Another drawback associated with the increased complexity of the reaction mechanisms and the description of the coal structure is the considerably higher effort required to adapt the kinetic and structural parameters to the feedstock. A variety of laboratory experiments are needed, especially to determine the structural parameters for the coal lattice. To ensure that network pyrolysis models can be used rapidly and in an automated manner, an extensive database needs to be created with kinetic and structural parameters for many feedstocks, such as coals or biomass. Due to these two disadvantages, the use of network pyrolysis models is limited for CFD applications. Several approaches to overcome these issues have been developed and they are presented in Section 5.
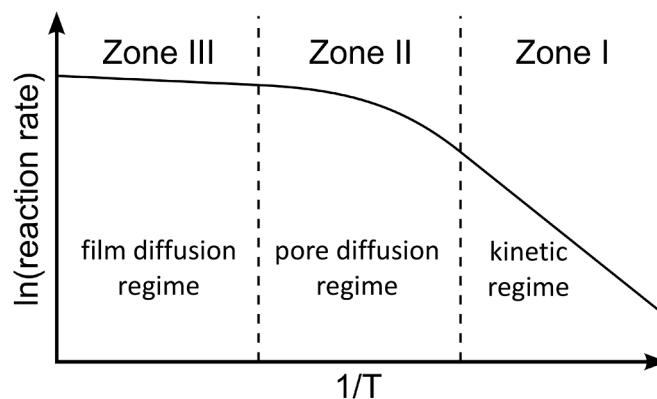
Fig. 10. Rate controlling regimes in Arrhenius diagram. Adapted from [45].

3. Char conversion

Char conversion mainly takes place after the main devolatilization phase, but can also occur simultaneously with the final pyrolysis phase, when residual volatile matter is still present. The char particle is the remaining solid structure after pyrolysis, composed of the parent coal's matrix, consisting of mainly carbon and mineral matter (the latter is also called "ash"). The correct description of the conversion processes taking place during char conversion is of particular relevance for the entire coal conversion process. This relevance is due to the fact that char conversion is usually much slower than pyrolysis and therefore defines the time required for coal conversion. When modeling char conversion processes, two aspects are particularly important:

- Adequate prediction of the carbon conversion level;
- Correct estimation of the gas composition formed by heterogeneous reactions.

The economical use of coal as a source of carbon for energy or material use is only possible if a carbon conversion level of $X_C > 99.5$ % can be achieved [117]. While the use of coal for electricity production by combustion is still the dominant conversion process, in recent years it has increasingly been used to produce synthesis gas by gasification. Therefore, acquiring the knowledge of how the gasification agents and operation conditions influence reaction kinetics is essential to produce the optimized synthesis gas for downstream utilization.

The following section presents the physical processes taking place during char conversion. The processes will be first described from a phenomenological point of view in Sections 3.1-3.4. Afterwards, the abstraction into model formulations will be outlined and advanced models are discussed in Section 3.5. Wherever applicable, a discussion on the specific model's capabilities to predict sulfur and nitrogen release is included.

3.1. Physical and chemical processes during char conversion

The process of char conversion is fundamentally different to pyrolysis. However, the pyrolysis conditions have a particular influence on char conversion processes. The char structure is formed during pyrolysis and therefore depends strongly on the conditions of the preceding conversion step [57,118]. In particular, during pyrolysis the porosity of the particles largely increases, leading to highly porous char structures [119–122]. Therefore, char particles are characterized by an intrinsic (inner) surface area and it is reasonable to assume that heterogeneous reactions occur over the entire surface. Under these assumptions, the whole char conversion process is governed by the combined effect of the transport of the reactants outside of the particle (film) and inside the particle's porous structure with the heterogeneous reactions occurring on the intrinsic surface. Additionally, the temperature histories during

devolatilization may influence the char molecular structure, by means of the so-called thermal annealing process (described in Section 3.2.4), influencing the kinetics of the heterogeneous reactions.

The numerous physical processes taking place during char conversion are strongly affected by the char particle's structure. They can be divided into three groups:

1. Heterogeneous surface reactions;
2. Intra-particle phenomena, especially pore diffusion;
3. Film diffusion.

Investigations carried out by Walker Jr. et al. [123] and Gray et al. [124] concerning the temperature dependency of film diffusion, pore diffusion and heterogeneous surface reactions have shown that, in certain temperature ranges, one process or a combination of two processes controls the overall rate. They postulated three reaction regimes. This model was later confirmed by other researchers, e.g. Smoot and Smith [125], and, in the char conversion literature, is today widely accepted as the classical "three-zone" theory for the interpretation of experimental data. A common illustration of the "three-zone" theory is given by the Arrhenius diagram in Fig. 10.

At low temperatures (Zone I, note the abscissa in Fig. 10 is $1/T$), the overall rate is limited by oxidation and/or gasification kinetics alone. Therefore, Zone I is also known as the *kinetically controlled regime*. Transport processes are significantly faster than reaction kinetics, resulting in a uniform concentration profile in which gas phase species concentrations are equal in the bulk phase and on the outer and inner particle surface.

In Zone II, at intermediate temperatures, the reaction kinetics are much faster than in Zone I. Pore diffusion effects become more important, limiting the overall rate. Thus, Zone II is also known as the *pore-diffusion-controlled regime*. With increasing temperature, the reaction kinetics become faster than the diffusion inside the porous structure of the particle, resulting in the formation of radial concentration gradients for the reactive species. Concentrations of gas phase species in the pores are lower than on the outer particle surface, while concentrations between the outer particle surface and the bulk phase remain similar. These conditions are of high practical relevance because combustion and gasification processes mostly take place in this regime [126–128].

Finally, at very high temperatures in Zone III, film diffusion becomes the rate-limiting step. Reaction kinetics are much faster than transport processes from the bulk phase to the outer particle surface, so Zone III is also known as the *film-diffusion-controlled regime*. Concentration gradients of reactive gas species are mostly observed in the boundary layer. Heterogeneous surface kinetics on the outer particle surface are so fast that they convert all reactants immediately. The concentrations of reactive species in the pores are nearly zero. Zone III, especially, is strongly influenced by particle-gas interactions since the flow conditions determine the boundary layer thickness and transport processes between the phases.

Further, homogeneous gas phase reactions in the boundary layer can have an impact on the particle conversion. Shaddix and colleagues [129–131] studied char conversion for different atmospheres. During the combustion of particles larger than 60 μm, mainly at high temperatures, gas-phase oxidation of CO to form CO_2 in the boundary layer must be taken into account for reliable predictions. CO released from the conversion of larger particles consumes O_2 in the boundary layer and reduces the partial pressure of O_2 on the particle surface. This gas-phase conversion is exothermic and increases the boundary layer temperature, subsequently transferring this heat to the particle. However, this also leads to an increase in the importance of CO_2 gasification reactions. Both these factors lead to a decrease in the particle temperature, firstly because the exothermic reaction of char with O_2 is hindered and secondly because the endothermic reaction of char with CO_2 is promoted. These effects depend, among other things, on the particle size.

The classical three-zone theory is an idealization; separation by sharp boundaries, as shown in Fig. 10, is not realistic. Two more or less distinct transition zones exist between the main zones. In these transition areas, overall rates are determined by a combination of the respective rate-limiting processes. However, it is impossible to determine the exact impact of the respective rate-limiting processes in the transition zones. As a result, the transition zones are commonly neglected, and boundaries are assumed to be sharp [123]. Moreover, not only the temperature, but also the particle size is a determining factor for the reaction regime.

The theory of three zones highlights the dominant process in specific situations. The process is dominated either by the chemistry or the transport phenomena. Modeling the char conversion requires the definition of the conversion rate, which usually falls into one of two categories:

1. Global, apparent or observed reaction rates;
2. Intrinsic reaction rates.

As the name implies, the apparent reaction rates (global, apparent) are those which can be observed and measured under any process conditions. The chemical reaction rate constants are influenced and determined by all three processes, and their effects are all lumped in under the conversion rate. They are highly empirical, basing the conversion rate on the particle's external surface area and on the oxidizer concentration at the external surface. Consequently, these models are only able to provide reliable predictions within small variations of the feedstock and operating conditions.

On the other hand, intrinsic models separate the chemistry, the internal and the external transport, using dedicated models for each of them. The char surface consists of an inner and outer part, the inner surface area being much higher than the outer one [132]. For this reason, intrinsic models account for the intrinsic surface area (inner surface) where the heterogeneous reactions take place, and can take into account the fact that the oxidizer within the particle has a non-uniform concentration profile.

Determining the intrinsic surface area theoretically is a very difficult task. In most cases, this value is obtained experimentally with analytical methods such as the Brunauer–Emmett–Teller (BET) approach. Further, the char conversion process itself causes changes in the characteristics of the intrinsic surface area. The decoupling of these physical aspects from the conversion rate allows intrinsic kinetic parameters to be defined for the heterogeneous reactions, referring to the chemical process only. Additional models are then required to describe the decoupled aspects:

- Film diffusion: external transport of the oxidizer from the bulk, through the boundary layer, onto the particle surface;
- Pore diffusion: internal transport of the oxidizer within the particle porous structure;
- Evolution of the intrinsic surface area along the conversion process.

Intrinsic reaction rates can only be measured directly when the conversion process is in the *kinetically controlled regime* (Zone I), when transport phenomena are not limiting. The observed kinetic rate in these cases can be described by intrinsic values for the kinetic parameters:

- Pre-exponential factor;
- Activation energy.

With rising temperatures, the difference between the observed and intrinsic reaction rates increases, indicating a transition from Zone I to Zone II. If extrapolated to higher temperatures, the intrinsic reaction rate exceeds the observed reaction rate due to the intra-particle depletion of the oxidizer. Thus, in Zone II, intrinsic kinetic rates can only be applied if the transport limitation is also accounted for. The transport limitation can be explicitly modeled or expressed as an effectiveness factor that counterbalances the overestimation of the reaction rate. The

effectiveness factor η can be defined as:

$$\eta = \frac{\text{Actuall overall reaction rate of all reactant species}}{\text{Maximum possible reaction rate of all reactant species}} \tag{17}$$

More details will be discussed in Section 3.3.

Similarly, the observed rates in Zone III are clearly lower than those estimated using intrinsic reaction rates at the particle temperature, since the overall rates are limited by external transport processes, which will be discussed in detail in Section 3.4.
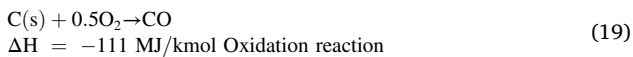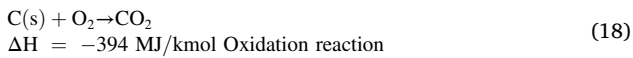
Before discussing the transport limitations, the reaction kinetics and the methods used to model this process are presented.
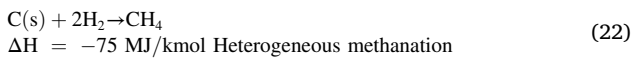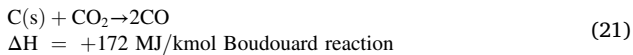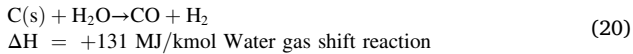
3.2. Heterogeneous surface reactions

Heterogeneous surface reactions take place on the inner and outer char particle surface. The char particle itself consists mostly of carbon and ash, with minor amounts of other elements. It is a common simplification to assume that only carbon remains as a reactive species in the char structure after pyrolysis. Nevertheless, some models also account for the content of other elements (especially H), also supporting the description of different char types of varying reactivity [57].

In char conversion processes, carbon atoms are consumed by various reactions. These consumption reactions can be globally divided into combustion and gasification reactions [126,133]:

Combustion:

$$C(s) + O_2 \rightarrow CO_2$$
$$\Delta H = -394 \text{ MJ/kmol Oxidation reaction} \tag{18}$$

$$C(s) + 0.5O_2 \rightarrow CO$$
$$\Delta H = -111 \text{ MJ/kmol Oxidation reaction} \tag{19}$$

Gasification:

$$C(s) + H_2O \rightarrow CO + H_2$$
$$\Delta H = +131 \text{ MJ/kmol Water gas shift reaction} \tag{20}$$

$$C(s) + CO_2 \rightarrow 2CO$$
$$\Delta H = +172 \text{ MJ/kmol Boudouard reaction} \tag{21}$$

$$C(s) + 2H_2 \rightarrow CH_4$$
$$\Delta H = -75 \text{ MJ/kmol Heterogeneous methanation} \tag{22}$$

C(s) represents solid carbon. Compared with the gasification reactions, oxidation reactions are several orders of magnitude faster. Methanation is several orders of magnitude slower than the other gasification reactions. Therefore, when modeling char conversion in gasification processes, heterogeneous methanation is often neglected if H_2 is competing as a reactant with H_2O or CO_2. Combustion and gasification can also be compared with regard to the reaction enthalpy. Combustion reactions are exothermic, whereas gasification reactions are endothermic except for heterogeneous methanation. The two oxidation reactions are commonly represented as a unique reaction:

$$C(s) + \frac{\psi + 1}{2}O_2 \rightarrow \psi CO_2 + (1 - \psi)CO \tag{23}$$

There is no general consensus as to whether CO_2 is produced primarily from the heterogeneous reactions or from the homogeneous reactions occurring in the particle boundary layer. However, it is accepted that both CO and CO_2 are formed as the main products of the heterogeneous reactions. Experimental evidences showed that CO_2 is produced mostly at low temperatures, while CO formation becomes predominant at high temperatures. For this reason, the ratio between the CO/CO_2 produced is usually modeled by empirical correlations based on the Arrhenius equation [134,135]:
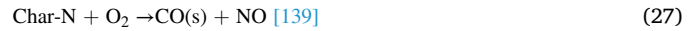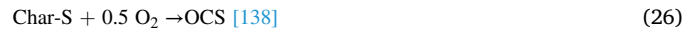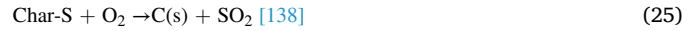
$$\frac{CO}{CO_2} = \frac{1 - \psi}{\psi} = A\exp\left(-\frac{E}{RT}\right) \tag{24}$$

Heterogeneous surface reactions can be described in several ways in a chemical mechanism. In general, they differ in their complexity (number of steps) and in the detail with which the individual steps of surface reactions are addressed.

The conversion of the elements that remain retained in the char, such as nitrogen and sulfur, are also released to the gas phase during oxidation and gasification process [136,137]. These reactions can also be divided into combustion and gasification reactions. Because of the complex structures in which these heteroatoms can be chemically linked to the char, different reaction paths take place.

A few examples of possible reacting mechanisms regarding the formation of SO_x and NO_x are exemplified:
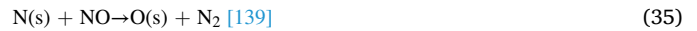
Combustion:

$$\text{Char-S} + O_2 \rightarrow C(s) + SO_2 \text{ [138]} \tag{25}$$

$$\text{Char-S} + 0.5\ O_2 \rightarrow OCS \text{ [138]} \tag{26}$$

$$\text{Char-N} + O_2 \rightarrow CO(s) + NO \text{ [139]} \tag{27}$$

$$\text{Char-HCN} + O_2 \rightarrow O(s) + CO + HCN \text{ [139]} \tag{28}$$

Gasification:

$$\text{Char-S} + CO_2 \rightarrow CO + OCS \text{ [138]} \tag{29}$$

$$\text{Char-N} + CO_2 \rightarrow C(s) + CO + NO \tag{30}$$

$$\text{Char-S} + H_2O \rightarrow CO + H_2S \text{ [138]} \tag{31}$$

$$\text{Char-N} + H_2O \rightarrow C(s) + NO + H_2 \tag{32}$$

$$\text{Char-N} + H^+ \rightarrow C(s) + NH \rightarrow \rightarrow NH_3 \text{ [140]} \tag{33}$$

NO_x Reduction:

$$C(s) + NO \rightarrow N(s) + CO \text{ [139]} \tag{34}$$

$$N(s) + NO \rightarrow O(s) + N_2 \text{ [139]} \tag{35}$$

$$N(s) + NO \rightarrow N_2O \text{ [141]} \tag{36}$$

$$C(s) + N_2O \rightarrow N_2 + CO(s) \text{ [141]} \tag{37}$$

Conversion of Char-S was investigated experimentally and numerically in [138,142,143], suggesting that sulfur is mostly released in combustion as SO_2 (Eq.(25)), with minor amounts of OCS (Eq.(26)). The release as OCS is promoted in gasification with CO_2 (Eq.(29)). In steam gasification the main released product is H_2S (Eq.(31)).

Conversion of Char-N is complex and several aspects influence the products of this process. Molina et al. [139,141] investigated experimentally and numerically the behavior of Char-N during char conversion and revealed the main reacting paths that lead to the release of nitrogen. Molina et al. [141] produced char from pyrolysis of coal in a fluidized bed reactor, and later investigated the conversion of char-N injecting the produced chars in the same reactor using oxidizing atmospheres. The results were further validated by Molina et al. [139], when HBr was used as a radical-scavenging agent in pulverized coal combustion in a turbulent flow multi-fuel combustor. Without HBr addition, they observed that high concentration of NO in the gas phase hinders Char-N conversion into NO, while low concentrations promotes this process. They suggest that Char-N, instead of being released directly as NO (Eq.(27)), must be released also as HCN (Eq.(28)), which then reacts in the gas-phase in a process strongly influenced by operating temperatures and reactants concentrations. At 1170 K, the HCN released would react with O_2 forming intermediate NCO, which is able react and destroy NO molecules, dropping overall NO concentrations. In the presence of

HBr, oxidation of HCN to NCO is quenched, resulting in increased NO concentrations at 1170 K. At 1370 and 1570 K, HCN rapidly converts into NO. In the presence of HBr, this oxidation is quenched, dropping NO concentrations. In the same work, they also describe NO reduction in the char surface: NO reacts with an active carbon site, releasing CO and forming an active nitrogen site (Eq.(34)). The later reacts with NO, forming and releasing N_2 (Eq.(35)). In a parallel mechanism, NO reacts with nitrogen active site releasing N_2O (Eq.(36)), which reacts with active carbon site and is reduced into N_2 (Eq.(37)).

Tian et al. [140] also describes the reduction of the nitrogen atoms linked to the char in the presence of H^+ radicals (typical in steam gasification), releasing unstable NH species (imidogen), which further reacts until formation of stable NH_3 (Eq. (33)). Recently, Guo et al. [144] further validated the heterogeneous reduction of NO_x on the char surface.

3.2.1. Global reaction mechanism

An empirical *n*-th order reaction equation is often used to describe the kinetics of the char heterogeneous reaction described by Eq. (38) [145–147]:

$$q = k_s(T)P_s^n \tag{38}$$

where q is the combustion rate, normalized by the external particle surface, and k_s is the rate constant, which is a function of the particle surface temperature T. P_s is the partial pressure of oxygen at the particle surface, and n is the global reaction order. The assumption is made in many works that the heterogeneous reactions occur only on the external surface of the particle; for this reason, reaction rates are expressed as per unit of external surface. This hypothesis can be acceptable for char oxidation in many practical conditions, where heterogeneous kinetics can be faster than diffusion (Zone III) at the high temperatures existing in pulverized coal boilers. In fact, pore diffusion effects are implicitly included in the external surface kinetic constant. This approach generally fails for conditions between Zones I and II, when diffusion inside the pores is comparable to the heterogeneous rates. For example, because gasification reactions are much slower than oxidation reactions, assuming that the external surface model applies is also not acceptable for practical calculations in the gasification process.

The *n*-th order equation can also be used for empirically modeling intrinsic heterogeneous reactions, which are given by:

$$R = k_p(T)C_s^n = k_c(T)C_s^n \tag{39}$$

where C_s is the reactant concentration on the particle surface and n is the reaction order. The reaction constants k_p and k_c are expressed by the Arrhenius equation:

$$k_p(T) = A_pT^\alpha \exp\left(-\frac{E}{RT}\right) = \frac{k_c(T)}{(RT)^n} \tag{40}$$

The rate constants k_c and k_p in Eq. (40) are proportional to the ratio between the external and intrinsic surface area of the particle. However, the fact must be taken into account that the two surfaces evolve differently during char conversion. In addition, only a fraction of the intrinsic surface area might contribute to the heterogeneous reactions, and that active part of the intrinsic surface area changes along with the operating conditions and particle properties.

The empirical *n*-th order equation is often used to describe the kinetics of char conversion in terms of global reactions [132]. The global reaction lumps together several elementary reaction steps, including

- Adsorption of gas phase reactants to active surface sites;
- Heterogeneous surface reactions;
- Desorption of products into the gas phase.

Although the limitations of *n*-th order models are well known, this approach is widely used for practical simulations. Accurate results can only be attained when the kinetic parameters in the model are previously calibrated to a similar fuel and comparable operating conditions.

3.2.2. Langmuir-Hinshelwood (LH) reaction mechanism

Fundamental studies of char conversion processes have shown that the heterogeneous reactions of carbon with gas phase reactants include additional phenomena [119]. In particular, they include:

- Adsorption of reactants at active sites on the surface with formation of an intermediate species;
- Heterogeneous surface reaction of intermediate species and formation of adsorbed product;
- Desorption of product from the surface and regeneration of the active sites.

The *n*-th order model can only describe the global behavior of the phenomena mentioned above, and generally it fails to reflect the adsorption/desorption nature of the reaction. In particular, Hurt and Calo [148] pointed out that the simple *n*-th order reaction approach is not able to account for the different apparent orders observed during char oxidation. Notably, reviewing the data in the literature, they observed that the order of the char oxidation reaction is typically dependent on the temperature. A more mechanistic description of the char reactions can be given by active site theory. Active sites can be identified as carbon edges or dislocations, oxygen and hydrogen functional groups and inorganic impurities.

The simplest mathematical model, which describes gas-solid reactions, was proposed by Langmuir [149], and later extended by Hinshelwood to include a dual site mechanism, for heterogeneous catalytic reactions. Next, formulations are discussed separately for oxidation and gasification.

3.2.2.1. Char oxidation.
The classic Langmuir-Hinshelwood model can be slightly adjusted for char oxidation, dividing adsorption into two steps, as reported by Laurendeau (1978) [119] and references therein:

$$\begin{aligned} C_f + O_2 &\rightarrow C(O) + O & k_1 \\ C_f + O &\rightarrow C(O) & k_2 \\ C(O) &\rightarrow CO & k_3 \end{aligned} \tag{41}$$

The first step describes the breaking of the molecular oxygen into two atoms and the adsorption of one of them by a free carbon site C_f. The second step describes the adsorption of the atomic oxygen produced in the previous step. Finally, the third step describes the desorption of CO into the gas phase. Typical values for the activation energies are in the range of 10–125 kJ/mol and 160–400 kJ/mol for the adsorption and desorption steps [150–153]. The global char conversion rate can be obtained from the mechanism in Eq. (41). First assuming that the only surface species formed is C(O) and that the surface coverage is constant (steady-state assumption):

$$0 = k_1P_{O_2}(1-\vartheta) + k_2P_O(1-\vartheta) - k_3\vartheta \tag{42}$$

ϑ being the fraction of occupied sites. Also, assuming that the concentration of atomic oxygen O is low, it can be rearranged as:

$$\vartheta = \frac{k_1P_{O_2}}{k_1P_{O_2} + k_3} \tag{43}$$

The reaction rate can be then derived from the rate of desorption of surface species C(O):

$$R = k_3\vartheta \tag{44}$$

Substituting ϑ by applying Eq. (43):

$$R = k_3\left(\frac{k_1P_{O_2}}{k_1P_{O_2} + k_3}\right) \tag{45}$$

Rearranging, dividing all terms by k_3 leads to:

$$R = \frac{k_1 k_3 P_{O_2}}{k_1 P_{O_2} + k_3} = \frac{k_1 P_{O_2}}{1 + \frac{k_1}{k_3} P_{O_2}} \tag{46}$$

At low temperatures, the mechanism is limited by the desorption step, resulting in a zero-order reaction. At high temperatures, by contrast, the limiting step is the adsorption, leading to a first-order reaction.

Hurt and Calo [148] showed that the mechanism in Eq. (41) cannot reproduce the experimental behavior of the char oxidation reactions. In fact, at low temperatures (< 900 K), experiments show a higher reaction order with respect to the oxygen concentration, between 0.6 and 1.0 [154]. In these temperature ranges, char conversion is generally studied employing Thermogravimetrical Analysis (TGA). At moderate temperatures (900 K $<$ T $<$ 1400 K), large uncertainties have been reported, especially depending on the assumptions related to the heat and transport models necessary to extract the intrinsic parameters. In fact, the reaction order measured is only apparent, and the actual order can be reconstructed by the Thiele expression $n_{app} = (n+1)/2$. Despite the lack of extensive datasets and the difficulties of evaluation, experimental studies suggest that char conversion is characterized by a low intrinsic order at moderate temperatures.

From this analysis, it is evident that the previous two-step reaction mechanism cannot properly describe the different reaction regimes observed during the oxidation of char. Additionally, the two-step oxidation mechanism predicts only the formation of CO. However, at low temperatures CO_2 is also produced.

A more detailed mechanism which is able to predict the experimental trends was proposed by Hurt and Calo [148], based on different experimental studies [146,151,161–169,152,154–160]:

$$\begin{array}{ll} C_f + O_2 \rightarrow 2C(O) & k_1 \\ C(O) + O_2 \rightarrow CO_2 + C(O) & k_2 \\ C(O) \rightarrow CO & k_3 \end{array} \tag{47}$$

The proposed reactions do not define the precise stoichiometry with respect to the free surface sites (C_f), and instead adopt the simplest form of the corresponding rate laws. In particular, both reactions 1 and 2 contain implicitly C_f on the left-hand side to correctly balance the carbon contents. Analogously following the procedure described in Eqs. (42)-(46), the overall reaction rate is therefore expressed as follows:

$$R = \frac{k_1 k_2 P_{O_2}^2 + k_1 k_3 P_{O_2}}{k_1 P_{O_2} + \frac{k_3}{2}} \tag{48}$$

According to the results obtained by Haynes and Newbury [153], the activation energies of the three reactions are $E_3 > E_2 > E_1$, which lead to different rate-determining steps depending on the temperature. At low temperatures, k_3 is small and the system is under O_2-complex reaction control. For moderate temperatures, the system is under desorption reaction control. For high temperatures, k_3 is large and the system is under adsorption reaction control. The global rate of reaction can be simplified when the reaction temperature is known [148]:

$$\begin{array}{ll} R = k_2 P_{O_2} & \text{Low Temperatures} \\ R = k_3 & \text{Moderate Temperatures} \\ R = 2k_1 P_{O_2} & \text{High Temperatures} \end{array} \tag{49}$$

Therefore, the resulting model dependency on the oxygen partial pressure predicts that the reaction order with respect to oxygen shifts from one (O_2-complex control, low temperature) to zero (desorption control, moderate temperature) and back to one again (adsorption control, high temperature). A detailed discussion including low-moderate and high-moderate temperatures is available in Hurt and Calo [148]. The three-step mechanism therefore exhibits good consistency with the experimental evidences for the whole range of temperatures in practical systems. Additionally, the primary CO/CO_2 ratio is given by:

$$\frac{[CO]}{[CO_2]} = \frac{k_3}{k_2 P_{O_2}} \tag{50}$$

which is consistent with the empirical approach previously discussed in Section 3.2.1. The more mechanistic description of the char conversion process enables the Langmuir-Hinshelwood-based reaction mechanisms to predict char conversion rates correctly over wide temperature and pressure ranges.

3.2.2.2. Char gasification. The Boudouard gasification reaction of char with CO_2 can be modeled by a two-step Langmuir-Hinshelwood (LH) mechanism [170–172]:

$$\begin{array}{ll} C_f + CO_2 \rightleftharpoons C(O) + CO & k_4, k_5 \\ C(O) \rightarrow CO & k_8 \end{array} \tag{51}$$

which leads to the following reaction rate [123,173]:

$$R_{c,CO_2} = \frac{k_8 k_4 P_{CO_2}}{k_8 + k_4 P_{CO_2} + k_5 P_{CO}} = \frac{k_4 P_{CO_2}}{1 + \frac{k_4}{k_8} P_{CO_2} + \frac{k_5}{k_8} P_{CO}} \tag{52}$$

This reaction rate shows that the presence of CO in the gas phase may lead to a reduction in the overall reactivity, due to the inhibitive effect of CO. In fact, the CO can react with the oxygen in an activated carbon site C(O) producing CO_2, reducing the overall reactivity.

A similar mechanism can be written for the water gasification reaction [123]:

$$\begin{array}{ll} C_f + H_2O \rightleftharpoons C(O) + H_2 & k_6, k_7 \\ C(O) \rightarrow CO & k_8 \end{array} \tag{53}$$

with the corresponding reaction rate [123,173]:

$$R_{c,H_2O} = \frac{k_8 k_6 P_{H_2O}}{k_8 + k_6 P_{H_2O} + k_7 P_{H_2}} = \frac{k_6 P_{H_2O}}{1 + \frac{k_6}{k_8} P_{H_2O} + \frac{k_7}{k_8} P_{H_2}} \tag{54}$$

Similarly, the presence of H_2 may limit the reactivity inhibiting the steam gasification rate.

In practical applications, the gasification atmosphere contains both the gasification agents CO_2 and H_2O and the products CO and H_2. This means that the gas phase reactants (e.g. CO_2 and H_2O) compete for the active sites on the char surface. Therefore, active sites on the surface can be blocked by the other reactants, so the reaction rate for the single reactant is reduced [114,125]. Additionally, LH mechanisms also allow inhibition by adsorbed reaction products on the surface to be taken into account [126,127].

The overall reaction rate including both H_2O and CO_2 gasification can be written as [173,174]:

$$R_c = \frac{k_4 P_{CO_2} + k_6 P_{H_2O}}{1 + \frac{k_4}{k_8} P_{CO_2} + \frac{k_5}{k_8} P_{CO} + \frac{k_6}{k_8} P_{H_2O} + \frac{k_7}{k_8} P_{H_2}} \tag{55}$$

The active sites should be the same for the CO_2 and H_2O reactions. However, some active sites may be present in pores which are smaller than the larger reactant (in this case, CO_2), meaning that they are active only for the smaller reactant (in this case, H_2O) [175]. In addition, CO_2 is adsorbed molecularly, while H_2O can be dissociatively chemisorbed to form OH species [176].

3.2.3. Comparison of reaction mechanisms

Several differences can be found when comparing global and LH

Table 6
Pore classification based on pore diameters [178].

Pore class	Pore diameter
Micropores	< 2 nm
Mesopores	2–50 nm
Macropores	> 50 nm

reaction mechanisms. In general, global mechanisms are simple and they have an empirical character. LH mechanisms are more complex since they describe char conversion processes in a mechanistic manner, taking into account more phenomena during conversion. Therefore, char conversion rates can be predicted correctly over a wider temperature and pressure range with a LH mechanism compared to a global mechanism. Concerning the behavior of the reaction rate with increasing level of reactant concentration, global mechanisms correspond to the behavior of a Freundlich adsorption isotherm. In contrast, the reaction rate behavior of LH mechanisms correlates with Langmuir adsorption isotherms. The adsorption behavior described by a Langmuir isotherm is distinguished by a maximum level of adsorbate on the adsorbent surface for high concentrations of adsorbed species in the surrounding fluid phase. This means that the capacity of the adsorbent is limited, which is similar to the limited number of active sites on the char surface. Therefore, LH reaction mechanisms have better preconditions concerning the adsorption behavior at high reactant concentrations for the description of kinetics for char conversion processes.

3.2.4. Thermal annealing

Niksa [42] describe the evolution of char composition in two major steps. The first is the char formation during coal devolatilization, when coal continues to release volatiles until the process is completed at about 1300 K, if the temperature is held for enough time. At this point, the element fractions of nitrogen and sulfur are comparable to the fractional char mass, while hydrogen and oxygen fractions in char are much lower than the fractional char mass. This is caused by the preferential release of volatiles containing high oxygen and hydrogen contents. The second step is the thermal annealing, which not only leads to higher ordering of the carbonaceous matrix, but also changes the composition of char by releasing additional HCN, H_2S, H_2, CO, and CH_4. These transformations increase carbon content in char and nearly eliminates all hydrogen and oxygen. Nitrogen retention depends on coal rank, and sulfur retention is significant even at 2300 K in inorganic FeS crystals (triolites) that are formed from pyrite decomposition. This residual sulfur is extremely difficult to eliminate in inert conditions.

The thermal annealing hinders the reactivity of char during oxidation and gasification because of the collapse of pores, which diminishes the surface area available for the heterogeneous reactions. Further, the elimination of the elements H, O, N, and S during annealing eliminates active sites that are available for the initiation process of char conversion. These two transformations explain the reduced reactivity observed for chars depending of their degree of graphitization. Natural graphite oxidation, for instance, takes place at much higher temperatures (onset 900 K) [177] and is a very slow process when compared to char oxidation.

Niksa [42] explains that, for mathematical modeling purposes, heteroatoms can be included in the char composition and have them

released at the overall rate of char conversion, omitting the annealing stage from process simulations. This remains an acceptable simplification unless the process includes extended reacting time under reducing conditions at elevated temperatures.

3.3. Intra-particle phenomena

Char conversion processes are strongly influenced by intra-particle phenomena. Typical intra-particle phenomena include pore diffusion and the evolution of the pore structure, as well as the evolution of the char particle in general during conversion. The porous structure is very complex and initially results in the release of volatile matter and moisture from the parent coal's lattice during drying and pyrolysis. It consists of different pore types which can be classified by their diameter, see Table 6.

When the heterogeneous reactions rates are calculated, both the global and LH reaction mechanisms require the concentrations of gas phase reactants in the vicinity of the outer and inner char particle surface. While the concentration of gas phase reactants on the outer particle surface is determined by film diffusion processes, pore diffusion processes determine the concentration inside the particle pores. Since most of the active sites are inside the pores on the inner surface, pore diffusion has a significant influence on the total conversion rate of char. The pore structure can be characterized by various parameters including:

- Pore length;
- Pore diameter;
- Tortuosity;
- Porosity and the fraction of macro-, meso- and micropores [127, 132].

Gas phase species transport inside the pores can be classified into two categories:

1. Molecular diffusion, mainly observed in macro- and mesopores;
2. Knudsen diffusion, mainly observed in micropores.

Effective pore diffusion is determined either by one mechanism or by a mixture of both. Which mechanism dominates depends on the pore diameter or, more specifically, the Knudsen number Kn. For *Kn << 1* classical continuum assumptions are justified (molecular diffusion), while for *Kn >> 1* the laws of kinetic theory of gases for strongly diluted/rarefied media (Knudsen diffusion) need to be applied. For both limits of the Knudsen number, respective diffusion coefficients can be formulated [132]. These diffusion coefficients have to be adjusted to the real pore geometry, since both coefficients are defined based on the simplifying assumption that the pore is a long, straight channel.

Next to the influence of pore diffusion on char conversion rates, the

Table 7
Char classification system according to [179,182].

Char groups	Group I	Group II	Group III
Two-dimensional schematic representation			
Porosity (%)	> 70	variable, 40–70	< 40
Average wall thickness (μm)	< 5	> 5	> 5
Shape	Spherical-subspherical	Subspherical	Angular
Typical swelling ratio	> 1.3	< 1.0	< 0.9
Typical residual mass ratio	0.1–0.5	0.1–0.5	1.0

evolution of the pore and char structure has to be borne in mind. Depending on the reaction regime, the chemical reaction, and therefore the consumption of carbon in the char particle, mainly takes place on the outer char surface or inside the char particle pores on the inner surface. If the char conversion process takes place in Zone III, the chemical reactions consume carbon on the outer surface. The active sites in the pores are not involved. Therefore, very little evolution of the pore structure is observed. The char particle is consumed from the outside to the core. In the process, the particle diameter decreases continuously while the particle density and porosity remain almost constant. This conversion behavior is also called shrinking-core behavior.

The opposite behavior can be observed if the char conversion takes place in Zone I, the kinetic-controlled regime. There, the chemical reactions occur on all active sites on the outer and inner particle surface. Since the inner surface in the porous structure is much higher, a major portion of the carbon is consumed in the pores. Significant pore evolution can be observed, which leads to a change in the inner surface. Since most of the char consumption takes place on the inner (intrinsic) surface, the pore evolution causing this change needs to be taken into account. The effect of pore evolution on reaction kinetics has an opposing character:

- Increase in particle porosity through an increase in pore volume accompanied by an enhancement of the pore diffusion;
- Decrease in intrinsic particle surface area due to merging of pores, accompanied by a loss of active sites.

The conversion process in Zone I results in the excavation of the char particle. Since most of the carbon is consumed in the pores, the particle's porosity increases while the density decreases. The diameter of the particle remains almost constant.

As mentioned above, the initial char structure strongly depends on the conditions of the preceding conversion steps: drying and pyrolysis. Benfell et al. [179] developed a classification system for the initial condition of char based on the work of Bailey et al. [180] and Lightman and Street [181]. Char is classified by structural parameters such as porosity or average wall thickness. The classification system is summarized in Table 7.

As shown in Table 7, char in Group I is characterized by a high void volume, resulting in a high particle porosity. The walls of the char particle are thin and form a hull around the void. The swelling ratio and the residual mass ratio show that the particle increases in volume and loses significant amounts of mass during pyrolysis. This leads to a considerably decreased density of the initial char particle compared to the parent coal particle. In general, the particles are of spherical shape. The opposite behavior is exhibited by Group III char. The particles are characterized by a low porosity and void volume in the pore channels and a high wall thickness. The char particles tend to shrink and release only a small amount of mass during pyrolysis. Therefore, the density of Group III char is high in comparison with the other groups. The char particle is mainly angular. Group II char is a combination of the other groups. Areas with a high void volume and very dense parts can be found in the same particle. Therefore, the particle properties fall between the values of the other groups. The examination of different char particle groups is important to take into account the influence of the different particle geometries on the reaction kinetics.

3.3.1. Modeling pore diffusion

According to Hong [132], two general groups of approaches can be identified when pore diffusion pore processes are modeled:

1. Use of the analytical Thiele modulus approach [183];
2. Use of numerical solutions in radial direction through the porous char structure [184].

The first models describing pore diffusion processes were developed by Thiele [183]. He studied the transport process in particle pores using catalyst pellets. Since catalyst pellets and char particles are both porous structures whose surface is covered with active sites, the findings by Thiele [183] have been abstracted to describe the influence of intra-particle diffusion on heterogeneous reaction kinetics of solid fuels. The connection between reaction kinetics and the Thiele modulus was achieved by introducing an effectiveness factor η. The effectiveness factor allows the observed reaction rates r_{obs} to be calculated using the intrinsic reaction rates r_{in}, which are only valid when the char conversion process is taking place in the kinetically controlled regime.

$$\eta = \frac{r_{obs}(C_s)}{r_{in}(C_s)} \tag{56}$$

A detailed discussion, including the derivation of Eq. (56) based on the contemplation of the percentages of the char conversion taking place on the outer and inner particle surface, can be found in Hong [132]. As noted above, it is not the entire intrinsic particle surface area which contributes to the conversion in Zone II and Zone III due to transport limitations. Thus, the effectiveness factor can be interpreted as the fraction of the inner particle surface where heterogeneous surface reactions take place.

An approximate estimation of the effectiveness factor using the Thiele modulus φ is given by the Thiele modulus approach [183,185]. The relation depends on the geometry of the particle as shown in the following equations:

In Cartesian coordinates:

$$\eta = \frac{\tanh(\phi)}{\phi} \tag{57}$$

In spherical coordinates:

$$\eta = \frac{1}{\phi}\left[\frac{1}{\tanh(3\phi)} - \frac{1}{3\phi}\right] \tag{58}$$

In a more general formulation, the Thiele modulus can be calculated using the formulation given by Bischoff [185]:

$$\phi = L\frac{vr_{in}(C_s)}{\sqrt[2]{2}}\left[\int_0^{C_s} D_{eff}(C)vr_{in}(C)dC\right]^{-\frac{1}{2}} \tag{59}$$

where L is the characteristic length, v is the stoichiometric coefficient and D_{eff} is the effective pore diffusion coefficient. For spherical char particles, the ratio of the sphere volume to the outer sphere surface is used as the characteristic length [186]. The stoichiometric coefficient is determined by the heterogeneous surface reaction with the gas phase reactants. It describes the amount of consumed gas-phase reactant per consumed amount of carbon on a molar basis. Several models are available to define the effective pore diffusion coefficient, e.g. the Parallel Path Pore Model (see below).

Examining the effects of pore diffusion on heterogeneous reactions kinetics using the analytical Thiele modulus is a feasible method which does require a limited amount of information about the porous structure of the particle. In general, structural parameters defining the pore's geometry require specific experiments. These can usually only be performed ex situ. Thus, particle extraction for various conversion levels during the combustion/gasification would be required, which is often not feasible. Nevertheless, the Thiele modulus approach allows only an approximate estimation of the effectiveness factor. It is important to note that the relations defined by Eq. (57) and Eq. (58) are the only exact solution for reactions with a global reaction order of unity.

Hong [132] and Hong et al. [161] developed a correction factor for the relations between the Thiele modulus and the effectiveness factor, decreasing the error for reaction kinetics with a reaction order deviant from one.

3.3.2. Evolution of intrinsic surface

The structural evolution of porous particles undergoing gasification or combustion is important for predicting burnout behavior [187–190]. Porous solids such as coal and biomass chars are known to have complex pore structures [191,192]. As already mentioned, the heterogeneous reactions take place on the intrinsic surface of the char, which evolves during the conversion process. The rate of char conversion is strictly connected to the availability and the characteristics of this surface. The complexity of the evolution of these surfaces requires an adequate description for improved prediction of the process. Many models of surface structure evolution have been developed, with the grain and the pore models being widely employed, partially due to their relative simplicity and success in reproducing experimental data obtained under kinetically controlled conditions.

3.3.2.1. Grain and pore model.

Before the more dedicated models describing the pore structure were proposed, the effects described above were incorporated into empirical reaction rate constants, neglecting several important changes in the solid structure. As an alternative, grain and pore models were proposed. In these models, physical properties of the materials are accounted for, such as the pore sizes and total porosity, and evolve along the conversion process. From these assumptions, the changes in the intrinsic surface area can be estimated, serving as an input to calculate the reaction rate. In this way, the structural parameters can be decoupled from the overall rate of reaction.

The essential difference in these approaches is the aspect on which they focus. Chars can be described as volumes divided into a solid matter and a void fraction. The grain models focus on the consumption of the solid matter fraction, described by grains that are consumed and reduce in volume. The pore models focus on the increase in void fraction, which is characterized as a distribution of pores that grow along the conversion, increasing the void volume.

Such models can introduce several simplifications, e.g. assuming that the grains/pores are the same shape and size. However, chars are not homogeneous in terms of the pore dimensions, distribution and shape, and this has led to many other attempts to improve pore models. The pore models can be classified into a few categories [193]. The list below briefly describes the main categories, with examples of their use:

- Average pore size model [159,194–196]. All pores are assumed to have the same length and diameter and not to intersect.
- Grain model [197–199]. The char is described by many non-porous sub-particles (grains), each one reacting as a shrinking sphere. The grains may have different distribution of sizes.
- Random pore model [191,192,200–207]. One of the most widespread models with several variations proposed. Pores of random sizes and orientation describe the porous structure. They may be adjusted for intersections.
- Dendritical pore distribution model [208,209]. The pores are sized according to the distribution and the smaller pores are branches from the larger pores (pore tree approach). The model assumes that volatiles generated in the interior of particles create fine pores which combine closer to the surface to form larger pores.
- Spherical vesicle pore model [210]. A number of spherical bubbles (vesicles) of equivalent or different sizes are linked by smaller tubes (micropores), which account for the majority of the particle surface area.
- Discrete pore model [211,212]. Similar approach to the grain model. The char is divided into numerous small blocks. A certain fraction is randomly defined as void to account for the total porosity;
- Stochastic pore network model [213–216]. Similar to the average pore size model and the random pore model, but it allows random variation in the diameter of pores between the pore intersections.
- Semi-empirical models [217–224].

3.3.2.2. Random pore model (RPM).

As mentioned earlier, during char conversion the porous structures due to carbon consumption and, therefore, the intrinsic surface of the char particle changes correspondingly. This influences the fraction of carbon consumed in the pores. Since combustion kinetics are several orders of magnitude faster than gasification kinetics, the consumption predominantly takes place on the outer surface and in the openings of the porous char particle structure, the macropores. On most of the pore surface, including meso- and micropores, no heterogeneous surface reactions take place. Therefore, the char particle is consumed from the outside to the inside and no considerable change in the intrinsic surface is observed.

On the contrary, the slower reaction kinetics of the gasification reactions utilize the entire inner particle surface for heterogeneous surface reactions. The higher use of available surface for chemical reactions leads the main conversion site to shift from the outer particle surface, moving inside the pore structure. Since the main carbon consumption site is within the pore structure, the char conversion leads to the excavation of the particle inducing two opposed effects important for the char reactivity:

1. increase in the particle porosity caused by an increase in the pore volume, accompanied by the enhancement of the pore diffusion and
2. decrease in the inner particle surface caused by the coalition of pores, accompanied by a loss of reactive sites.

The loss of active sites due to a decrease in the inner particle surface is important for predicting char gasification kinetics correctly. The well-known Random-Pore Model (RPM) proposed by Bhatia and Perlmutter [225,226] can be used to describe the evolution of the intrinsic surface during char conversion. As input parameters, this model requires the actual carbon conversion and an empirical structural parameter, the so-called ψ-parameter, depending on the parent coal. The examination of the actual carbon conversion incorporates the current conversion progress. With the input parameters, the RPM calculates a factor which can be interpreted as the ratio between the current and the initial inner particle surface.

3.3.3. Parallel path pore model (PPPM)

As mentioned in the introduction part of Section 3.3, two different diffusion mechanisms, namely molecular and Knudsen diffusion, are responsible for transporting gas phase species from the outer particle surface into the particle pores.

Each mechanism dominates the overall diffusion rate for a certain range of pore sizes. However, when the diffusion coefficients are defined according to the respective formulation, diffusion is assumed to take place in long, straight channels [132]. This assumption is not consistent with the real pore geometry. Therefore, an adaptation of the standard diffusion coefficient is necessary to account for the porous structure of char particles. The modified diffusion coefficients are often called effective diffusion coefficients D_{eff}.

One possibility to adapt standard diffusion coefficients to the real pore geometry is the Parallel Path Pore Model (PPPM) proposed by Wheeler [196] and Carberry [227]. The model takes pore structure parameters such as porosity ε into account. However, the model makes several assumptions to limit the complexity involved in determining the effective pore diffusivity. The influence of Knudsen diffusion and the effects of microporosity on the overall diffusion are neglected since calculating Knudsen diffusion coefficients requires detailed knowledge of several pore structural parameters such as the tortuosity and pore diameter. These parameters are only accessible by experiments with the char. Therefore, only the molecular diffusion is examined, and modified by two parameters, the particle porosity ε and an empirical parameter f/τ. The empirical parameter represents the ratio between the percentage of porous volume in macropores f and the tortuosity τ. It is used for adaptation and to lump the influences of all neglected effects into one parameter.

$$D_{eff,ij} = \varepsilon \frac{D_{ij}f}{\tau} \qquad (60)$$

The advantage of this type of approach is that it reduces the complex porous structure to one factor with no need to determine any other porous structure parameter. The benefit of this sort of approach is discussed by Sun and Hurt [127]. Their main argument is that effective pore diffusion coefficients can be predicted with a reasonable value for the lumped, empirical parameter over a wide range of fuels and operating conditions, without any modifications to the coal rank or temperature.

3.3.4. Char particle evolution

During char consumption by combustion and/or gasification, particles evolve because of the consumption of carbon from the char matrix. While the approaches used to describe the evolution of the pore structure are described in Section 3.3, the change in overall particle properties, especially density and diameter, is described here. This is directly related to the way carbon is consumed in the different regimes, see Fig. 10.

3.3.4.1. Mode-of-burning model. An empirical model, the so-called Mode-of-Burning model [228], can be used to determine the carbon consumption profile during char conversion processes, and therefore how the char particle properties alter. The empirical parameter α is introduced to determine the conversion process. This parameter varies between zero and one, determining two limiting cases:

1. $\alpha = 0 \rightarrow \rho_p = $ const. $\rightarrow$ shrinking core behavior of the char particle;
2. $\alpha = 1 \rightarrow d_p = $ const. $\rightarrow$ development of excavated char particle.

The empirical parameter α is used to set the carbon density and carbon mass into relation. The relation is shown in the following equation

$$\frac{\rho_c}{\rho_{c,0}} = \left(\frac{m_c}{m_{c,0}}\right)^{\alpha} \qquad (61)$$

with ρ_c and $\rho_{c,0}$ as the current and initial carbon density, and m_c and $m_{c,0}$ as the current and initial carbon mass. Knowing the change in carbon density and the apparent ash density ρ_a (assumed to be constant), the current apparent char particle density ρ_p can be calculated using

$$\frac{1}{\rho_p} = \frac{X_a}{\rho_a} + \left(\frac{1 - X_a}{\rho_c}\right) \qquad (62)$$

with X_a as the current ash mass fraction of the char particle. Afterwards, the current, apparent char particle density is used to calculate the current particle diameter d_p using

$$\frac{d_p}{d_{p,0}} = \left[\left(\frac{m_p}{m_{p,0}}\right)\left(\frac{\rho_{p,0}}{\rho_p}\right)\right]^{\frac{1}{3}} \qquad (63)$$

with $d_{p,0}$ as the initial char particle diameter, m_p and $m_{p,0}$ as the current and initial char particle mass and $\rho_{p,0}$ as the initial char particle density.

When using the Mode-of-Burning model, the challenge is to find a good value for α which is consistent with the simulated conversion process. Mitchell et al. [229] studied ten US coals concerning the value for the empirical parameter α. Their results for simulation and experimental data showed that the value for α differs only slightly for the investigated coals, although the rank of the investigated coals covers lignite to bituminous coals. The best-fit value for the investigated US coals is $\alpha = 0.2$. However, Mitchell et al. [229] only investigated char consumption by combustion. For consumption by gasification, Liu and Niksa recommend a value near unity (α = 0.95).

It should be noted that the Mode-of-Burning model has a major drawback. The parameter α is usually assumed to be constant for the
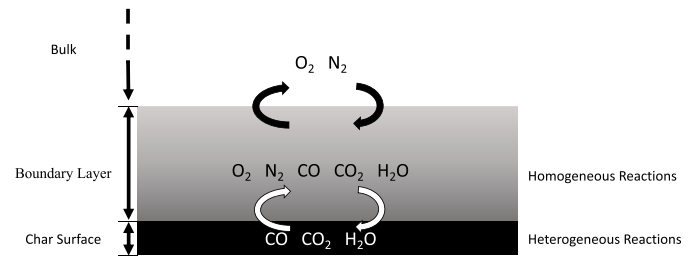

Fig. 11. Schematic representation of the external transport phenomena during char conversion.

entire process. It cannot be adapted to varying consumption processes whose reaction kinetics differ considerably from each other. For example, in an industrial entrained-flow gasifier, the char particles react in oxidizing atmospheres (combustion) near the burner while they react in reducing atmospheres (gasification) in the post-flame zone.

3.3.4.2. Model by Haugen and Mitchell. Haugen et al. [230] proposed a detailed approach in order to overcome the drawbacks of the Mode-of-Burning model. Instead of assuming that α is constant for the whole conversion, this parameter varies with conversion and in effect, describes how the radius and apparent density of a char particle change with conversion. In this case, the assumptions made are high thermal conductivities (no intra-particle temperature gradient) and Thiele's approach to concentration gradients and uniform ash distribution.

Further, they assume that conversion occurs in two different stages:

- First stage of char conversion, in which particle radius (and thus volume) are constant;
- Second stage, in which particle size and density change.

The length of the first stage is defined by τ, which is the time required for the mass of the outermost layer to be completely consumed. In CFD simulations, this value can be obtained explicitly during the calculations. When the combustion conditions are in Zone I, the value of τ is equal to the total particle conversion time, and the radius remains constant. In combustion Zone III, τ is negligible compared to the total conversion time, as the conversion takes place from the outside due to limitation in the oxidizer. In Zone II, τ is a fraction of the particle conversion time, and the changes in particle size and apparent density are governed by the effectiveness factor η. Thus, during the course of conversion, the variable mode of conversion of a porous particle is given by:

For $t \leqslant \tau$

$$\frac{dr_p}{dt} = 0 \qquad (64)$$

$$\frac{d\rho_p}{dt} = \frac{dm_p}{dt}\frac{1}{V_p} \qquad (65)$$

and for $t > \tau$

$$\frac{dr_p}{dt} = \frac{dm_p}{dt}\frac{1 - \eta}{4\pi r_p^2 \rho_p} \qquad (66)$$

$$\frac{d\rho_p}{dt} = \frac{dmp}{dt}\frac{\eta}{Vp} \qquad (67)$$

where r_p is the radius of the char particle. Therefore, the model provides the time when the particle radius starts to decrease and, after this time, the rates at which the radius and apparent density decrease.

This model was applied by Haugen et al. [231], with particles assumed to be spherical and uniform in composition and morphology, using a kinetic mechanism for the char oxidation reactions based on the Haynes model [232], allowing the simulation of char oxidation with a

detailed heterogeneous reaction mechanism, tracking species concentrations at the particle's outer surface, and taking into account the fact that the apparent density and diameter of the particle vary depending on the mass loss (typical of combustion Zone II)

3.4. External transport processes

Char conversion can only happen in the presence of gaseous oxidizer agents O_2, CO_2 or H_2O in the carbonaceous matrix. Therefore, the oxidizer must be present in the vicinity of the reacting char surface. Film diffusion accounts for the transport of gas phase species from the bulk phase to the outer particle surface. The particle surface and bulk phase are separated from each other by a boundary layer whose thickness depends on particle-gas interactions and flow conditions. Gas phase species are transported through the boundary layer, which can be turbulent or laminar, by means of molecular diffusion and convection. For char conversion based on heterogeneous surface reactions, the influence of the Stefan flow on the mass transfer has to be taken into account [229]. Schematically shown in Fig. 11, the resulting process can be described by three parallel events:

1. Transport of reactants and products from/to the bulk into and across the boundary layer;
2. Diffusion into the char porous structure;
3. Consumption by heterogeneous and gas-phase reactions.

Another aspect which needs to be taken into account is the formation of an ash layer on the outer surface of the char particle, typical in Zone III combustion, where the reaction kinetics are faster than the internal pore diffusion. This results in a particle with carbon-rich core protected by an isolating ash layer, as discussed in Section 3.4.2 below.

3.4.1. Modeling transport processes

In order to account for the transport processes in the boundary layer, a suitable description of film diffusion is required. Three models are widely employed, all of which are briefly summarized below:

1. Single-Film model
2. Two-Film model
3. Continuous-Film model.

3.4.1.1. Single-film model. The Single-Film model, also called the One-Film model, is the simplest approach to describe the mass transfer of reactive species from the bulk phase into and across the boundary layer until the particle surface. Many assumptions are invoked [233]:

- The burning process is quasi-steady.
- The spherical carbon particle burns in a quiescent, infinite ambient medium (bulk phase).
- There are no interactions with other particles and no convection effects.
- At the particle surface, carbon reacts with the oxygen, producing CO or CO_2. In general, global reaction formulations or simple LH mechanisms are used to describe the consumption of carbon by heterogeneous surface reactions.
- The gas phase consists of the reactants, the reaction products and inert gas species. The reactants diffuse inward; on the outer particle surface, they react with the carbon, forming the respective products, which then diffuse outward. The inert gas forms a stagnant layer, causing a Stefan flow. Secondary homogeneous reactions of products do not affect the heterogeneous surface reactions, assuming they are taking place far away from the reacting surface in the bulk phase.

- The gas phase thermal conductivity (λ), specific heat capacity (c_p) and the product of the density and mass diffusivity (ρD) are all constant. In addition, the Lewis number (Le) is assumed to be unity:

$$Le = \frac{\lambda}{(\rho c_p D)} = 1 \tag{68}$$

- Intra-particle diffusion is neglected.
- The particle has no temperature gradient and radiates as a gray body to the surroundings without the participation of the intervening medium.

Taking into account x_0 as the char surface and x_∞ as the conditions at the outer region, the single-film model results in:

- CO/CO_2 concentration is maximum at x_0 and is equal to the bulk value at $x\infty$;
- Temperature is maximum at x_0 and is equal to the bulk temperature at $x\infty$;
- O_2 is equal to the bulk value at $x\infty$ and reaches a minimum at x_0;

By coupling this transport model with a kinetic model, the concentration of oxygen in the particle surface can be calculated, resulting in the solution of energy and mass flows in the process. This model, however, has many simplifying assumptions. An improved description is proposed in the Two-Film and Continuous-Film models.

3.4.1.2. Double-film and continuous film model. In the Double-Film model, also called the Two-Film model, the main product of char oxidation is carbon monoxide (CO), which is released and further reacts with oxygen to form CO_2 in the boundary layer [233]. Thus, two reaction mechanisms are accounted for:

- Heterogeneous reaction between oxidizer and carbon on the surface of the char;
- Homogeneous reactions in the boundary layer.

Homogeneous reactions are assumed to be infinitely fast, forming an infinitely thin flame sheet, forming two separated and not overlapping layers:

- Pre-flame zone, between the char surface and the flame sheet.
- Post-flame zone, between the flame sheet and the end of the boundary layer.

More complex temperature and concentration profiles along the boundary layer are observed compared to the single-film model. All gases in the boundary layer are considered to be unreactive, except in the flame sheet, where the peak temperature is attained [234]. All the remaining assumptions of the One-Film model remain unchanged.
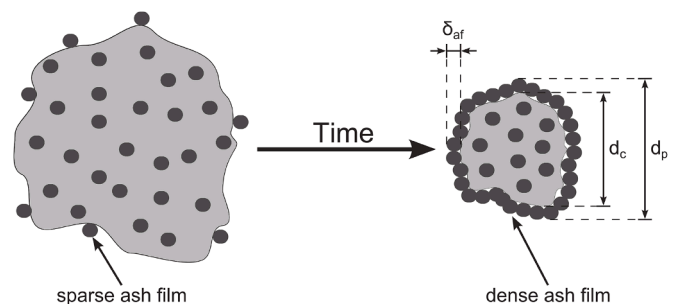

Fig. 12. Composition of char particle during char conversion process. Adapted from [117].

The Continuous-Film model assumes that the flame is distributed within the boundary layer, instead of occurring in a single sheet. No inert zone is taken into consideration, and the boundary layer must be discretized, see e.g. [235]. This approach results in a more complicated, but more realistic profile of the species concentrations and temperature along the boundary layer.

3.4.1.3. Comparison of different models. The Single-, Double- and Continuous-Film models are characterized by increasing levels of description of the physical and chemical processes occurring in the boundary layer during char conversion. However, an improved description also increases the required computational resources for simulations. Trying to find a good compromise, Hecht et al. [130] performed CFD simulations of the same case, applying the three different models. The Two-Film model exhibited larger deviations than the Single-Film model. Both are compared to the Continuous-Film model, which is considered to be the reference. In this specific case, Single-Film model deviations were always below 16 % when the particle size was between 60–135 μm and the bulk oxygen concentration was no higher than 60 %. These results were obtained after improving the Single-Film model by taking into account a calibrated mechanism for char consumption including reactions with O_2, CO_2 and H_2O.

Matalon [236] analyzed the dependence of the particle burning rate in terms of the surface and gas phase Damköhler number and found that there is a minimum value for the gas phase Damköhler number below which the gas phase is necessarily frozen (that is, characteristic diffusion time across the boundary layer is much shorter than characteristic homogeneous reaction time, yielding no reaction in the boundary layer). Since the Damköhler number is proportional to the square of the particle diameter, this implies that there is a diameter below which the single-film model is applicable.

Results of theoretical investigations [237,238] have indicated that the single-film model with CO formation at the particle surface is an acceptable model for particle sizes from 50 μm up to about 100 μm.

3.4.2. Influence of ash on transport processes

In general, the influence of ash on the coal conversion becomes important during char conversion. Additionally, the level of influence depends on the char conversion process. In experiments, a strong decrease in the reaction rates is observed in the late stages of char consumption [117]. The decrease in the conversion rate results in an increase in the char particle residence time in the reactor required to achieve the desired carbon conversion level of $X_C = 99$ % for industrial applications [127].

During char conversion, carbon is consumed by heterogeneous surface reactions and transported into the gas phase, while inert ash grains remain in the char particle or agglomerate on the outer particle surface, forming an ash layer. In this process, the particle is divided into two parts, as shown in Fig. 12:

1 a reactive carbon-rich core where the reactions on the inner and outer surface take place and
2 an ash layer forming around the core whose density and thickness increase continuously with increasing carbon conversion.

The division of the char particle has several effects on transport processes:

- "dilution" effect due to the reduction of the carbon mass and carbon surface available per unit particle volume, resulting in a reduction in the mass transport rate, and
- formation of an additional resistance for the mass and heat transfer from the gas phase, surrounding the particle, to the carbon-rich core through the ash layer.

These ash effects have to be taken into consideration using a char conversion model. The "dilution" effect can be integrated using the size of the carbon-rich core in the heat and mass transfer equations, as well as in the heterogeneous reaction kinetics. During char conversion, the diameter of the carbon-rich core decreases continuously while the char particle diameter, defined as the sum of the carbon-rich core diameter and thickness of the ash film, approaches a constant value asymptotically.

The second effect is taken into account in the ash inhibition model by incorporating the ash film as additional resistance in the heat and mass transfer equations. This resistance increases as the difference increases between the diameter of the carbon-rich core and the particle diameter.

As mentioned earlier, the influence of ash inhibition effects depends on the char conversion process. During combustion, the shrinking core behavior is dominant, resulting in a considerable loss of char particle diameter due to carbon consumption on the outer surface of the carbon-rich core, while at the same time the particle density remains constant. In this process, ash grains are released from the char matrix, agglomerating around the particle and forming an ash layer. By contrast, during gasification, the main consumption of carbon takes place in the porous char particle structure, resulting in the excavation of the particle. The number of ash grains reaching the outer surface is strongly limited. Therefore, ash inhibition influences char combustion much more strongly than char gasification due to the characteristics of the conversion progress for combustion and gasification.

3.5. An overview of advanced char conversion models

The discussion above highlights the complexity of char conversion and the multitude of physical and chemical processes involved in combustion and gasification applications. Consequently, a significant number of advanced char conversion models have been developed and are in fact still being developed.

In the following, a selection of different advanced char conversion models are presented briefly, mostly referring to the specific literature for further information. The specific submodels integrated into each model are finally summarized at the end in a table.

As computational power grows and makes it possible, future developments will definitely invest in quantum chemistry investigations. Nowadays, most of the investigations in this direction are based on graphene-like structures (i.e. an extended two-dimensional carbon network). Frankcombe et al. [239] performed ab initio calculations on basal plane oxidation of graphene layers for the release of carbon monoxide. Another example refers to the analysis of different active groups to study low-temperature spontaneous combustion [240]. Some investigations consider the graphene as a small PAH [241,242], while periodic graphene structures were considered to account for the influence of the solid structure at the reaction sites [243]. Although quantum chemistry-based kinetic models are not currently available for practical applications, it reveals a promising potential for future developments.

3.5.1. Carbon Burnout Kinetics/Extended (CBK/E) & Carbon Burnout Kinetics/Gasification (CBK/G)

CBK/E and CBK/G are the latest two versions of the Carbon Burnout Kinetics (CBK) model series. CBK/Extended (CBK/E) is one of the most recently developed models for coal combustion [133]. CBK/Gasification (CBK/G) is the successor model of CBK/E, adding gasification kinetics to the heterogeneous surface reactions [126]. Both models are widely used to interpret research data and model industrial applications [117]. The development of the models series and the submodels implemented are described in the following papers [117,126,127,133,148,229,244] as well as in the PhD theses by Hong [132], Benfell [245] and Shurtz [246]. Extension of CBK model to account for the conversion of char-S was done simply by releasing SO_2 together with the char burnout rate. Similarly, char-N is converted using a splitting function fNO, which determines the conversion ratio of char-N between NO and N_2.

A particular feature of the CBK/E and CBK/G is the correlation between the coal rank and char reactivity during heterogeneous conversion, so that predictions can be made knowing only the proximate and ultimate analyses of the parent coal. Niksa et al. [133] applied a rank dependency parameter to the frequency factor of the desorption of surface oxides during oxidation with O_2, but indicated that low rank coals can also have the reactivity of their chars strongly influenced by catalytic effects of minerals. Liu and Niksa [126] investigated and extended the same concept to gasification by CO_2 and H_2O, where rank dependency parameters were applied to the frequency factors of rates of production of surface oxides. Rank dependency for rate parameters of oxide desorption during gasification with H_2O was introduced for both frequency factors and activation energies. The authors stated that high-volatile bituminous coals or higher ranks exhibit gasification reactivity that diminishes with the fuel rank. For lower rank coals, the catalytic effects of minerals become more significant than the generic rank dependency correlations. These statements indicate that for lower rank coals having high content of catalytic minerals, additional experimental data could be necessary for reliable predictions. In these two works, the authors extended the CBK/E and CBK/G models to account for high pressure char conversion.

3.5.2. Char Conversion Kinetics (CCK) and n-th order Char Conversion Kinetics (CCKN)

CCK and CCK^N are two offsprings of the latest two versions of the CBK model series. They were proposed in the Ph.D. thesis by Shurtz [246]. CCK stands for Char Conversion Kinetics. Differently to the CBK model series, correlations for kinetic parameters are used which are based on coal structural parameters instead of the coal rank. These correlations are detailed in [246] and [247]. CCK uses a semi-global Langmuir-Hinshelwood kinetic mechanism while CCK^N uses power law expressions (n^{th}-order kinetic mechanism) for the surface reactions.

The sensitivity of the submodels in CCK was evaluated in [248], identifying that the annealing, the oxidation reaction order, the swelling model, and the mode of burning parameter are the most influential in the model performance, followed by extension of the CCK to oxy-fuel conditions in the Ph.D. thesis by Holland [249] and in [250], in which several submodels in the code were further modified to more realistic physics (e.g. particle diameter) . The annealing submodel was improved [251] accounting for the model sensitivity to char graphitization level.

3.5.3. Model for char particle conversion – Tremel & Spliethoff

Tremel et al. [252–257] at Munich Technical University (TUM), Germany, conducted a series of works on developing a model for char particle conversion. A comprehensive description of the experimental setup and the obtained results, as well as the model development based on these experiments, can be found in [213-218].

3.5.4. Model for char particle conversion – CSIRO

The Commonwealth Scientific and Industrial Research Organisation (CSIRO) model was developed at CSIRO Energy Technology, Kenmore, Qld, Australia [258]. The three dissertations prepared by Beath [193], Benfell [245] and Hodge [259] describe specific parts of the model development.

3.5.5. Model for char particle conversion – Mitchell

The last advanced char conversion model presented here was developed at Stanford University in the Mitchell group. The model is presented in several papers [147,260] and it accounts for char conversion in all three regimes (I, II and III), where the particle conversion changes between conversion (mode of burning) at constant volume (regime I), to constant density (regime III), with a transitions zone (regime II) where both volume and density changes along conversion. Additionally, the Ph.D. theses by Campbell [261] and Ma [262] give more details. Their results are further published in Ma and Mitchell [263] and Campbell and Mitchell [264], where attention was paid into extending the model to char conversion at high pressures. Haugen et al. [230] updated the model to predict the shift between the modes of burning as a function of the particle's mass conversion, not only the operating conditions. Haugen et al. [231] further extended the model by introducing adsorption-desorption kinetics for the heterogeneous reactions with CO_2 and detailed kinetics for the homogeneous gas-phase reactions. Tilghman et al. extended the model to conversion of chars from biomass in gasification and combustion environments in [265] and proposes reactant-specific effectiveness factor−Thiele modulus relations, together with introduction of CO and H_2 inhibition reactions in [266].

3.5.6. Atomistic model of char oxidation – Penn State University

An atomistic model for the simulation of char oxidation was developed and presented in the Ph.D. thesis by Louw [267], at Pennsylvania State University, USA. The model was supported by a deep compositional and structural analysis of coals, published in several papers [268–270]. The model allows coal conversion to be simulated using molecular dynamics techniques such as ReaxFF, employing their novel Perl script called Vol3D together with a pre-existing script, Fringe3D, to populate a 3D volume by stacking aromatic carbon clusters. Mineral matter and pores can be incorporated into the structure. This modeling approach accounts for the effect of competing structural factors that influence char reactivity. They also employed their molecular dynamics techniques to investigate the conversion of sulfur from coke in combustion [271,272]. The studies unraveled some complex mechanisms that lead to conversion of tightly bonded sulfur into the formation of C_2S, OCS, CNS in oxygen-poor atmospheres, which in the presence of hydrogen lead to formation of H_2S. In oxygen-rich conditions, tightly bonded nitrogen rapidly oxidized into CON and NO, while sulfur oxidized into OCS and successively converted into CO_2S, CO_3S and CO_4S, which probably leads to decomposition into more stable species such as CO_2 and SO_2. Despite the fact that such advanced models cannot be easily employed into CFD simulations of particle and reactor scales, they are very useful to understand the intermediate steps of the phenomena and not only the yields and rate of formation of target species.

3.5.7. Summary

The submodels used by the various models for simulating chemical and physical phenomena taking place during char conversion are summed up in Table 8.

Table 8

Summary of submodels implemented in advanced char conversion models, NthOR stands for n^{th} order kinetic mechanism (power law expression).

|	Hetero. surf. reaction	Film diffusion	Thermal annealing	Ash inhibition	Pore surf. evolution	Pore diffusion	Oxidation and gasification	CO/H_2 Inhibition gasification
CBK/E & CBK/G	LH mechanism	SFM	✓	✓	RPM	Thiele, PPPM	✓	✓
CCK & CCK^N	LH mech./ NthOR	SFM	✓	✓	RPM	Thiele, PPPM	✓	✓ ×
Tremel & Spliethoff	NthOR	SFM	✓	×	RPM	Thiele	Only gasification	×
CSIRO	NthOR	SFM	×	×	RPM	Thiele	✓	✓
Mitchell	LH mechanism	SFM	(✓)	×	RPM	Thiele	✓	✓
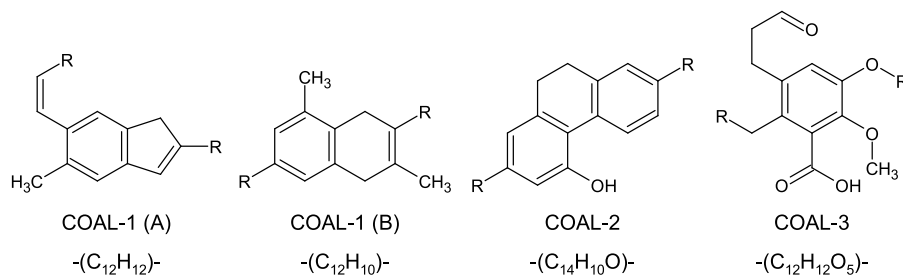
Fig. 13. Schematic chemical structure of the reference coals in the CRECK-S-C model [274].
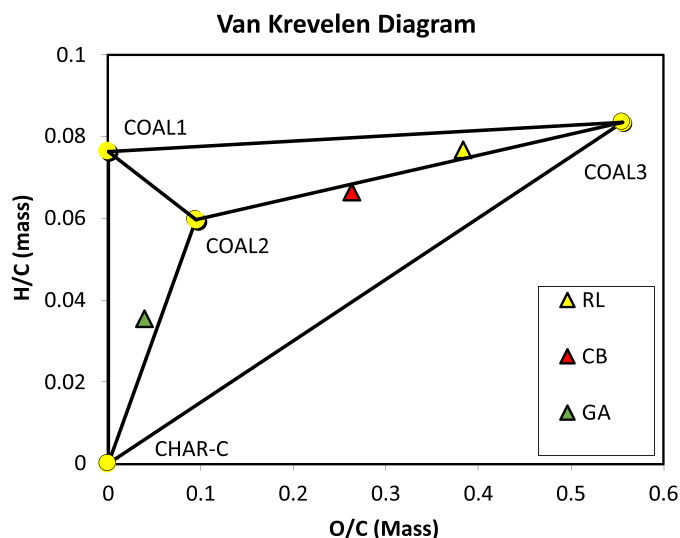

Fig. 14. Van Krevelen diagram containing the reference structures of the CRECK-S-C model. Triangular symbols refer to coal samples: Rhenish lignite (RL) [285], Colombian bituminous (CB) [286], German anthracite (GA) [287]. Round symbols refer to the reference coals.

4. Seamless model of coal conversion and pollutant formation – CRECK-S-C model

Another model that describes the thermochemical conversion of coal was developed in the CRECK modeling research group at Politecnico di Milano, Italy. They attribute a systematic nomenclature for their models: CRECK-p-yymm-t, in which p stands for the phase (solid, liquid or gas), yymm refers to the release date, and t stands for the fuel type (e.g. C for coal, P for plastics, B for biomass). The general theory behind the development of pyrolysis kinetic models for solid fuels was firstly published in [273]. The consolidated approach for coal pyrolysis was first discussed in [274], which brings the name CRECK-S-1002-C. Further developments were also extensively reported in a Ph.D. thesis [49]. The formation and release of sulfur and nitrogen species from coal was first proposed as standalone models in [275] and [276], respectively. The sulfur and nitrogen models were reformulated to integrate seamlessly with the main model in [277]. The CRECK-S-C models approach differs from the models discussed in the previous Sections in several aspects. In terms of its complexity and level of detail, the CRECK-S-C conversion model resides halfway between the very complex description adopted by the network models and the roughly simplified one-step, two-step, and DAE models. It was developed to offer a global description of coal conversion, despite the differences in the fuel structure, rank and composition, relying on the definition of reference coals and a coal characterization method, which is discussed in Section 4.1. Consisting in a multi-step kinetic model, it encompasses coal devolatilization, the formation and release of chemi-adsorbed species (metaplastic species), the formation of char and its annealing process, all of which are

discussed in Section 4.2. The kinetic model for heterogeneous char conversion by oxidation and gasification was first made available in [278], and will be discussed in Section 4.3. Thus, in contrast to the models discussed before, pyrolysis and char conversion are described in a seamless approach. Further, the model can be directly coupled with gas-phase kinetic mechanisms and uses the same CHEMKIN-like format. Finally, the release of pollutants or precursors (sulfur and nitrogen) will be discussed below, in Section 4.4. It is important to note that the approach is not limited to coal as a solid fuel but has also been adapted to the thermochemical conversion of plastics [279], lignocellulosic biomass [57,280–283] and algae biomass [284].

4.1. Reference coals and characterization method

While the network models discussed above require detailed data on the coal structure and molecular composition, the CRECK-S-C model brings together all this structural information and channels into four reference monomeric structures (i.e. commonly found clusters) that are bonded repeatedly in the polymeric macrostructure of coal:

1. COAL-1 – ($C_{12}H_{11}$) – Represents hydrogen-rich anthracites. It is a 50 % molar mixture of COAL-1(A) and COAL-1(B), and contains no oxygen;
2. COAL-2 – ($C_{14}H_{10}O$) – Represents bituminous coals, which have a similar composition and structure to many mid-rank coals;
3. COAL-3 – ($C_{12}H_{12}O_5$) – Represents lignites, which have a similar structure and composition to low-rank coals. It has a high content of both oxygen and hydrogen;
4. CHAR-C, pure carbon, representing larger aromatic clusters in graphitized structures.

Not only a molecular composition, but also a molecular structure is assigned for each of these reference components, as shown in Fig. 13, which represents the boundary characteristics of coals.

From the structures, it can be observed that COAL-1 (A) and (B) have branches containing methyl ($R-CH_3$) and larger ($R-CH_2-CH_2-R$) groups, resulting in an increased hydrogen content compared to unbranched

Table 9
Example of characterization of different coals in the CRECK-S-C model.

Elem. composition (dry wt.%)	Rhenish Lignite (RL) [285]	Colombian Bituminous (CB) [286]	German Anthracite (GA) [287]
C	65.83	71.85	85.23
H	5.05	4.77	3.03
O	25.25	18.87	3.31
N	0.68	1.76	1.23
S	0.29	0.54	1.80
Ash	2.9	2.2	5.40
Characterization (dry and ash-free wt.%)			
COAL-1	7.66	-	14.79
COAL-2	19.65	51.97	43.83
COAL-3	72.69	45.65	-
CHAR-C	-	2.38	41.38

Table 10

Kinetic mechanism of COAL-1 pyrolysis and char annealing [274].

	Reactants	Products	Reaction description
COAL-1 pyrolysis			
R1	COAL-1 →	5 CHAR-H + 0.1 CHAR-C + 0.2 H_2 + 0.9 CH_4 + G{C_{2-5}}	Low temperature pyrolysis
R2	COAL-1 →	G{TAR-1}	
R3	COAL-1 →	5 CHAR-H + 0.25 CHAR-C + 0.5 H_2 + 0.75 CH_4 + C_{2-5}	High temperature pyrolysis
R4	COAL-1 →	TAR-1	
R5	G{TAR-1} →	TAR-1	Release of metaplasts
R6	G{C_{2-5}} →	C_{2-5}	
R7	G{TAR-1} + CHAR-H →	5.3 CHAR-H + 3 CHAR-C + 2.55 H_2 + 0.4 CH_4	Crosslinking
R8	G{TAR-1} + CHAR-C →	4.3 CHAR-H + 4 CHAR-C + 2.55 H_2 + 0.4 CH_4	
Char annealing			
R9	CHAR-H →	2 CHAR-C + 0.5 H_2	Annealing
R10	CHAR-C →	CHAR-G	

aromatic clusters. COAL-3 has several oxygenated groups such as ether (R-O-R), methoxy (R-O-CH$_3$), carbonyl (R-C=O), and carboxyl (R-C(=O)-OH), which are typically found in lignites. The presence of these groups provides the compositional characteristics of these species and reflects the reactivity and the products released during the thermochemical conversion of coals.

These reference coals can be represented in a Van Krevelen diagram, providing a graphical description of their composition, as reported in Fig. 14. The reference species COAL-1, COAL-3 and CHAR-C are then employed to define a triangular area, which is called the characterization range. Every coal sample whose composition falls within this area can be characterized by a linear combination of the three limiting reference coals, taking into account the atomic mass balances. As bituminous coals are commonly used to generate energy, reference COAL-2 is included in the characterization, dividing this area into three sub-triangles. Thus, any coal to be studied is characterized by the linear combination of the reference coals defining the sub-triangle in which the fuel composition is located.

This characterization method requires elemental (or ultimate) analysis in terms of the carbon, hydrogen and oxygen contents, as the criteria for characterizing any fuel is to take into account the atomic mass balances. This approach strongly simplifies the amount of required experimental data on the fuel. The proximate analysis complements the fuel characterization by providing the moisture and ash contents. In Fig. 14,

Table 12

Species used by Sommariva et al. [274] in the de-lumping procedure.

Lumped tar	Composition	De-lumping species	Composition
TAR-1	$C_{10}H_8$	Naphthalene	$C_{10}H_8$
TAR-2	$C_{14}H_{10}O_1$	Phenanthrol	$C_{14}H_{10}O_1$
TAR-3	$C_{11}H_{10}O_2$	p-coumaryl alcohol	$C_9H_{10}O_2$
		Sinapyl aldehyde	$C_{11}H_{12}O_4$
		Phenanthrol	$C_{14}H_{10}O_1$
BTX	$C_{13}H_{14}$	Benzene	C_6H_6
		Toluene	C_7H_8
		Xylene	C_8H_{10}
Ox-C	$C_1H_3O_1$	Methanol	$C_1H_4O_1$
		Formaldehyde	$C_1H_2O_1$

three coal samples are also reported as an example: Rhenish lignite (RL), Colombian bituminous (CB), and German anthracite (GA). As they fall within the feasible characterization area, they can be represented as a linear combination of the reference coals.

The characterization procedure can be simply represented through the linear system of equations (69)–(71):

$$\alpha \cdot \omega_C^{RC1} + \beta \cdot \omega_C^{RC2} + \gamma \cdot \omega_C^{RC3} = \omega_C^{Coal\ Sample} \tag{69}$$

$$\alpha \cdot \omega_H^{RC1} + \beta \cdot \omega_H^{RC2} + \gamma \cdot \omega_H^{RC3} = \omega_H^{Coal\ Sample} \tag{70}$$

Table 11

Species produced from pyrolysis of reference coals of the CRECK-S-C model [274].

Category	Name	Description	Molecular formula
Metaplastic (chemi-adsorbed) species	G{COAL-2}	Intermediate solid from COAL-2 pyrolysis	$C_{12}H_{12}O_5$
	G{TAR-1}	Trapped lumped TAR-1	$C_{12}H_{11}$
	G{TAR-2}	Trapped lumped TAR-2	$C_{14}H_{10}O_1$
	G{TAR-3}	Trapped lumped TAR-3	$C_{11}H_{10}O_2$
	G{CO_2}	Trapped CO_2	C_1O_2
	G{COH_2}	Trapped CO plus H_2	$C_1H_2O_1$
	G{H_2O}	Trapped H_2O	H_2O_1
	G{BTX}	Trapped Benzene-Toluene-Xylene (6:3:1 molar)	$C_{13}H_{14}$
	G{CH_4}	Trapped CH_4	C_1H_4
	G{C_{2-5}}	Trapped C_2-C_5 hydrocarbons	C_1H_2
Char species	CHAR-H	High hydrogen content char	C_2H_1
	CHAR-C	Low hydrogen content char	C_1
	CHAR-G	Graphitized char	C_1
Gas species	H_2	Hydrogen gas	H_2
	CH_4	Methane	C_1H_4
	C_{2-5}	C_2-C_5 hydrocarbons	C_1H_2
	CO	Carbon monoxide	C_1O_1
	CO_2	Carbon dioxide	C_1O_2
Tar species	TAR-1	Lumped tar from COAL-1	$C_{12}H_{11}$
	TAR-2	Lumped tar from COAL-2	$C_{14}H_{10}O_1$
	TAR-3	Lumped tar from COAL-3	$C_{11}H_{10}O_2$
	BTX	Lumped aromatic species Benzene-Toluene-Xylene (6:3:1 molar)	$C_{13}H_{14}$
	H_2O	Water vapor	H_2O
	O_x-C	Methanol-Formaldehyde (1:1 molar)	$C_1H_3O_1$

$$\alpha \cdot \omega_O^{RC1} + \beta \cdot \omega_O^{RC2} + \gamma \cdot \omega_O^{RC3} = \omega_O^{Coal\ Sample} \qquad (71)$$

where α, β, and γ are the unknowns corresponding to the mass fraction of the reference coals that characterize the sample, ω_i^j is the mass fraction of the corresponding atom i in the solid j, RC 1–3 are the reference coals and the specific choice depends on the sub-triangle.

In order to better explain the characterization method, Table 9 shows the composition of these three coal samples, which have significant differences in their elemental compositions, and the resulting distribution of reference coals that are able to characterize them.

The resulting values in Table 9 show that different distributions of reference coals are necessary to characterize these samples. Also, different sub-triangles encompass the different samples, resulting in the absence of CHAR-C, COAL-1 and COAL-3 in the characterization of RL, CB and GA, respectively. It is interesting to note that since Rhenish lignite is in the upper triangle, CHAR-C is set to zero.

This characterization method allows a wide range of coal compositions to be represented in a single coal conversion model. However, it does not take into consideration the maceral composition of coals, which can significantly affect the combustion behavior of the fuel. The characterization can be extended to account for sulfur and nitrogen in coal, which is described independently of the hydrocarbon fraction, see Section 4.4.

4.2. Pyrolysis of hydrocarbon compounds and char formation

Each of the reference coals described in Section 4.1 follows its independent pyrolysis path, and the overall coal behavior is obtained by the linear combination of the behavior of the individual reference coals. The pyrolysis of each reference species forms a corresponding distribution of solid and volatile products that take into consideration the initial atomic mass balance. To facilitate discussion on the coal pyrolysis reactions, the kinetic mechanism of COAL-1 pyrolysis, including char annealing reactions, is reported in Table 10. The entire mechanism, and especially the reactions for the other reference structures, can be found in [274].

The model proposes two parallel reacting pathways for pyrolysis. The first is dominant at low temperatures (R1 and R2) and the second at high temperatures (R3 and R4). Two reacting paths compete in the low temperature mechanism: one is the decomposition reaction (R1), describing the formation of char and chemi-adsorbed species (trapped metaplastic species) with low molecular weight, and the other is the depolymerization reaction, describing the formation of trapped tar (R2). Similar competing reactions are present in the high temperature mechanism, accounting for decomposition (R3) and depolymerization (R4), describing the direct release of volatiles to the gas phase. Trapped species are also released to the gas phase when their evaporation energy barriers are surpassed (R5 and R6). The presence of trapped species promotes crosslinking, reticulation and repolymerization reactions,

which lead to secondary char formation (R7 and R8), explaining the reduced volatile yields found in low-temperature processes, compared to high-temperature processes. Reactions R9 and R10 are thermal annealing reactions, part of the pyrolysis mechanism, and will be discussed later.

Different versions of the model have been proposed in various publications, with some variations in the species, stoichiometries and kinetic parameters. Nevertheless, the same categorization can be applied for the species formed from pyrolysis of the reference coals in every version of the mechanism. Table 11 lists all the species produced from coal pyrolysis in the complete kinetic mechanism, as reported in Sommariva et al. [274].

While intermediate solids, metaplastic and char species are in the solid phase, tars and gases are volatiles. By considering these two separate phases, the coal mass loss can be accounted for. All the species named "G{}" undergo further release reactions until char and volatile species are formed. Three different lumped tar species are used to describe typical tars released from each reference coal, namely TAR-1, TAR-2 and TAR-3, referring to heavy-molecular-weight volatile species. The tar species O_x-C is a lumped representation of low-molecular-weight oxygenated compounds such as methanol and formaldehyde. Tar species BTX is a lumped representation of light aromatic species, such as benzene, toluene and xylene.

The characterization of the tars via the de-lumping procedure is necessary for coupling gas-phase kinetic mechanisms. The de-lumping enables the description of secondary gas-phase reactions that are very significant at high temperatures, increasing tar cracking reactions. Sommariva et al. [274] characterized the lumped tars using real chemical species, as reported in Table 12.

The devolatilization process leads to the formation of residual char. In the CRECK-S-C model [274,276,278], char is made up of so-called metaplastic species and char species (see Table 11), which allow different char compositions to be described. The model predicts not only the overall yield of char, but also the elemental composition. These aspects were extensively validated by comparison with low- and high-heating-rate experiments [274]. As pyrolysis progresses, intermediate solids and metaplastic species complete their devolatilization, leading to a residual solid composed of char species only. The release of metaplastic species (see Table 11) G{CH$_4$}, G{C$_{2-5}$}, G{CO}, G{CO$_2$}, G{H$_2$O}, and G{COH$_2$} at high temperatures describes the progressive drop in hydrogen and oxygen content, and the increase in the char carbon content.

As reported in Table 11, three char species are present: CHAR-H, CHAR-C and CHAR-G. Their presence is useful to describe the evolution of char characteristics such as the composition and the reactivity due to the annealing process (R9 and R10 in Table 10). Char species CHAR-H is formed in higher amounts during early coal pyrolysis. As the pyrolysis progresses to higher temperatures, young CHAR-H progressively transforms into amorphous CHAR-C species (R9), with a decreasing hydrogen content, accounting for the first step of char annealing. The second step of annealing (R10), also called graphitization, transforms amorphous CHAR-C into graphitized CHAR-G, accounting for the progressive reordering of the structure and the increase in cluster size.

The reaction rate constants are calculated using the kinetic parameters in Arrhenius format, as reported in Equation (72)

$$k(T_P) = A\ T_P^\beta \exp\left(-\frac{E_A}{R_G T_P} \right) \qquad (72)$$

in which A is the frequency factor, T_p is the particle temperature, β is the exponential coefficient of temperature (modified Arrhenius format), E_A is the energy barrier (activation energy) and R_G is the constant of gases. The general rate of reactions is described in Equations (73) and (74), for mono- and bimolecular reactions, respectively
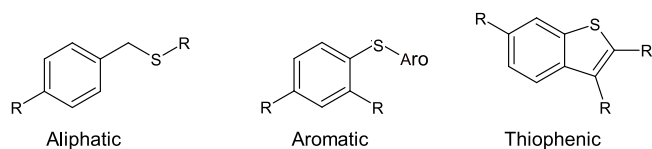
Table 13
Kinetic mechanism of char species conversion in the CRECK-S-C model [278].

	Reactants	Products
Reactions with O$_2$		
R1	CHAR-H + 0.75 O$_2$ →	0.5 H$_2$O + CO + CHAR-C
R2	CHAR-C + O$_2$ →	CO$_2$
R3	CHAR-C + 0.5 O$_2$ →	CO
R4	CHAR-G + O$_2$ →	CO$_2$
R5	CHAR-G + 0.5 O$_2$ →	CO
Reactions with H$_2$O		
R6	CHAR-H + 0.5 H$_2$O →	H$_2$ + 0.5 CO + 2 CHAR-C
R7	CHAR-C + H$_2$O →	H$_2$ + CO
R8	CHAR-G + H$_2$O →	H$_2$ + CO
Reactions with CO$_2$		
R9	CHAR-H + 0.5 CO$_2$ →	0.5 H$_2$O + 0.5 CO + 2 CHAR-C
R10	CHAR-C + CO$_2$ →	2 CO
R11	CHAR-G + CO$_2$ →	2 CO

Fig. 15. Typical organic sulfur structures in coal.

$$r = k[A] \tag{73}$$

$$r = k[A][B] \tag{74}$$

The mass balance of the coal particle is calculated as the sum of the mass of the solid species in the mixture, which is obtained as a function of their net formation/decomposition rates, see Equation (75)

$$\frac{dm_i^S}{dt} = V_S \rho_S R_i \tag{75}$$

where m_i^S is the mass of the i-th solid species in the particle, V_S is the solid particle's volume, ρ_S is the particle density, and R_i is the net formation rate of the i-th solid species resulting from the multi-step kinetic mechanism.

Because the reactants in the pyrolysis mechanism are all solid species, the concentrations are calculated using the relative density of the species with respect to the solid density (partial density). The CRECK-S-C model of coal pyrolysis was also presented in a reduced one-step version, in order to ease the implementation into CFD simulations [276].

4.3. Char conversion

Char species formed during pyrolysis of the reference coals react with oxidizing gases in heterogeneous reactions. Depending on the pyrolysis conditions, coal produces chars with different reactivities. As laid out in Table 13, the progressive decrease in char reactivity during oxidation and gasification is explained by attributing different apparent kinetic parameters to the heterogeneous reactions of CHAR-H, CHAR-C and CHAR-G [278]. With a total of 11 reactions, the heterogeneous kinetic mechanism describes the conversion of the three char species formed during pyrolysis, accounting for oxidation and gasification.

CHAR-G is a representation of the aged graphitic structure of char and thus exhibits low reactivity. CHAR-C is the young char with amorphous carbon organization, while CHAR-H is also a young char, but containing a relatively large amount of hydrogen and thus with more active sites and higher reactivity. The relative reactivity of the three char species CHAR-H, CHAR-C and CHAR-G is assumed to be ~40:20:1 at 1173 K [278], in order to fit the macroscopic observations about char formation and its subsequent conversion in the different operating conditions.

In the first set of reactions (R1–R5), char species react with O_2, releasing oxidized species and consuming the char. The more reactive CHAR-H undergoes partial oxidation, forming CHAR-C, H_2O and CO (R1). The chemical rationalization is related to the high content of hydrogen in CHAR-H species, which is considered to first be extracted by O_2, forming H_2O. After extraction, the remaining fraction of carbon is attributed to form directly CO and CHAR-C. The latter continues along its own oxidation reaction path without increasing the number of species and, consequently, the number of reactions in the model. Then, CHAR-C (R2 and R3) and CHAR-G (R4 and R5) react, forming either CO or CO_2. In order to consider the selectivity for the formation of CO and CO_2, two competing oxidation reactions are taken into consideration for both CHAR-C and CHAR-G. The kinetic parameters of the char conversion reactions were calibrated to agree with the kinetic parameters reported in the literature [133,148,288] as well as in terms of the CO/CO_2 ratio [134,264,289,290] .

Another set of reactions describe char gasification reactions with H_2O (R6–R8) and CO_2 (R9–R11). Similar to the reaction with O_2, CHAR-H is partially oxidized, forming CHAR-C. CHAR-C reacts with H_2O releasing H_2 and CO, and with CO_2 releasing CO. In the same way, CHAR-G reacts with H_2O and CO_2, but the rate of reactions are slower when compared to the reactions with CHAR-C. The relative reactivity of the three char species is similar to the reactions with O_2. Gasification reactions with H_2O are about 10^3 times slower than the corresponding oxidation reactions, while gasification reactions with CO_2 are 4–5 times slower than those with H_2O, at 1200 K.

In the CRECK-S-C model, the heterogeneous reactions are simply described on a volumetric basis, consolidating the surface features in the pre-exponential factors of the kinetic parameters. Thus, for chars with significantly different reacting surface areas, the pre-exponential factors must be adjusted. The heterogeneous reactions are defined as first-order with respect to the solid species. In relation to the gases, the reactions are defined as first-order, except for the partial oxidation reactions with O_2 (R1, R3 and R5), for which the reaction order was calibrated empirically, resulting in 0.78 for O_2.

The same formulation used for the pyrolysis reactions is used for the char conversion reactions. Because there are gas and solid species as reactants in the heterogeneous mechanism, their concentrations are calculated according to the phase they belong to. For gas species, the concentration is calculated using an equation of state, while for solid species the concentration is calculated as the partial density of the species in the particle.

4.4. Sulfur and nitrogen release from coal

The formation and release of SO_x, NO_x, and their precursors are directly related to the forms in which sulfur and nitrogen are present in the coal structure. These species are among the most important pollutants formed in coal combustion. In order to address these important aspects of coal conversion, the model was extended to include the

Table 14
Species produced from sulfur pyrolysis in the CRECK-S-C model [275].

| Category	Species	Description
Intermediate solids	FeS	Intermediate inorganic species formed from S_{PYR} pyrolysis
Metaplastic species	G{H_2S}	Trapped H_2S
	G{S_{GAS}}	Trapped S_{GAS}
	G{SO_3}	Trapped SO_3
	G{S_{TAR}}	Trapped S_{TAR}
Char species	S_{CHAR}	Sulfur chemically bonded to char
	$S_{CHAR-ING}$	Inorganic sulfur bonded to char
	Fe	Iron atom in the residual ashes
Gas species	H_2S	Hydrogen sulfide
	S_{GAS}	Lumped mercaptans
	SO_3	Sulfur trioxide / sulfuric anhydride
Tar species	S_{TAR}	Lumped tar containing sulfur
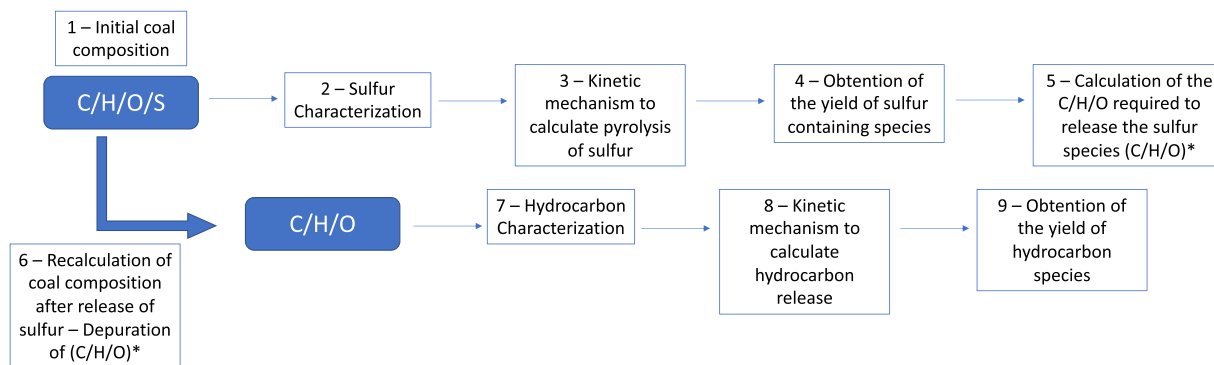
Fig. 16. Workflow for using the sulfur pyrolysis model combined with the main coal pyrolysis model.

release of sulfur and nitrogen during the process of coal pyrolysis in [275] and [276], respectively. These models share many similarities to the pyrolysis kinetic model of the hydrocarbon fraction of coal [274], but because of the particularities of these heteroatoms, some important differences were taken into consideration.

These two models describe the multiple forms in which these heteroatoms are present in coal, using a limited number of reference structures. The release of sulfur and nitrogen is described using several different chemical species, including light gases and condensable tars. The models also account for the retention of sulfur and nitrogen in the char, but kinetic models for the heterogeneous conversion of such species during char burnout were not developed concurrently.

Because of some differences in the formulation of these models, seamless integration with the hydrocarbon model was not possible. Using these models in combination required additional efforts, which hindered their widespread implementation in CFD simulations. Only recently the formulation of these models was unified in [277] to achieve the seamless integration of all the C/H/O/N/S fractions of coal in a single combustion model. The inclusion of SO_x and NO_x formation from char-retained sulfur and nitrogen during char conversion was presented in [291] and [292], respectively. A more detailed description of the sulfur and nitrogen models will be presented in Sections 4.4.1 and 4.4.2, respectively.

4.4.1. Kinetic model of sulfur release during coal pyrolysis

Similarly to the hydrocarbon pyrolysis model, the sulfur model proposes a characterization of the fuel in terms of reference species, accounting for both organic and inorganic sulfur compounds.

The inorganic sulfur is accounted for as two reference species:

- S_{PYR} – Pyritic sulfur – complex mineral structure containing iron sulfide together with other inorganic compounds. Most commonly containing sulfur in the oxidation state S^{-2}.
- S_S – Sulfate sulfur – salts and other complex inorganic compounds in which sulfur is present as SO_3^{-2} and SO_4^{-2}.
- The organic sulfur is accounted for in three chemical functionalities, attributed to three different reference species:
- S_{AL} – aliphatic sulfur – sulfur bonded to aliphatic carbons.
- S_{ARO} – aromatic sulfur – sulfur bonded to aromatic carbons.

Table 15
Species produced from nitrogen pyrolysis in the CRECK-S-C model [275].

Category	Species	Description
Metaplastic species	G{NH₃}	Trapped NH_3
	G{HCN}	Trapped HCN
	G{N$_{TAR}$}	Trapped N_{TAR}
Char species	CHAR-N	Nitrogen chemically bonded to char
Gas species	NH₃	Ammonia
	HCN	Hydrogen cyanide
Tar species	N$_{TAR}$	Lumped tar containing nitrogen

- S_{THIO} – thiophenic sulfur – sulfur present in heterocyclic compounds, bonded to two adjacent carbons in the ring.

The general chemical structure of these organic sulfur functionalities is illustrated in Fig. 15, each image showing sulfur bonded in different ways to carbon atoms.

The sulfur in each of these reference species has different reacting paths during pyrolysis, releasing gases (H_2S, SO_3, S_{GAS}) and tars (S_{TAR}) and forming char structures in different proportions. Table 14 shows the list of species present in this model, containing a brief description and the corresponding phase they belong to. The species S_{GAS} represents lumped mercaptans, and S_{TAR} represents lumped tar containing sulfur.

The mechanism is made up of a total of 17 species (5 reference species and 12 product species), involved in 15 reactions [49,275]. The model describes the pyrolysis of the organic components assuming that there are two competing reacting mechanisms (low and high temperatures). The low temperature mechanism describes the decomposition of the reference species forming intermediate metaplastic species (chemi-adsorbed species) that are further released to the gas phase at higher temperatures. While in the metaplast phase, the trapped tars can react with the char species S_{CHAR} in crosslinking and reticulation reactions, releasing light gases and retaining additional sulfur in the char. At high temperatures or high heating rates, the organic sulfur reference species directly decompose into sulfur gas (S_{GAS}) and tar (S_{TAR}) components, without the intermediate formation of the metaplastic phase.

The decomposition of inorganic components is described in a two-step release for pyritic sulfur (S_{PYR}) and a one-step release for sulfate sulfur (S_S). In the first step, S_{PYR} releases hydrogen sulfide (H_2S), forming an intermediate solid (FeS) and permanent inorganic sulfur in char ($S_{CHAR-ING}$). In the second step, the decomposition of FeS releases additional hydrogen sulfide, leaving iron in the remaining ashes. Sulfate sulfur decomposition forms sulfuric anhydride (SO_3) and permanent inorganic sulfur in char ($S_{CHAR-ING}$).

When a detailed compositional analysis of sulfur in the coal is available, the data can easily be correlated to these reference species to characterize the sulfur content. For when such data is not available, Maffei et al. [275] proposed correlations for the attribution of the reference species. The total sulfur content is first split into organic and inorganic assuming standard values: 54% is attributed to the inorganic fraction, 49% being pyritic sulfur and 5% sulfate sulfur. The characterization of the organic fraction, on the other hand, changes as a function of the carbon content (i.e. coal rank), following Equations (76)-(78):

$$S_{AL} = [0.276 - 0.69 \times (\omega_C - 0.6)] \times S_{TOT} \qquad (76)$$

$$S_{ARO} = [0.184 - 0.345 \times (\omega_C - 0.6)] \times S_{TOT} \qquad (77)$$

$$S_{THIO} = [1.035 \times (\omega_C - 0.6)] \times S_{TOT} \qquad (78)$$

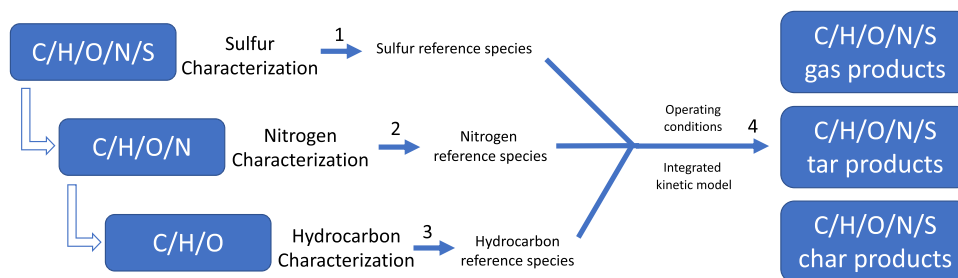In this first publication [275], sulfur release from coal pyrolysis was

Fig. 17. Schematic representation of the C/H/O/N/S characterization procedure and obtention of product distribution from coal conversion processes in the integrated CRECK-S-C model.

presented as a standalone model which was not completely compatible with the main coal pyrolysis model. Fig. 16 shows the steps required to correctly obtain the sulfur and hydrocarbon pyrolysis products from coal.

Because the stoichiometry of the sulfur model accounted only for the atoms of sulfur, calculating the corresponding composition of the products required a sequence of steps: characterization of the sulfur fraction of coal; calculation of yield and composition of sulfur pyrolysis products; recalculation of coal composition taking into account the corresponding composition of volatiles released (C/H/O)*; characterization of the recalculated hydrocarbon fraction of coal; calculation of yield and composition of hydrocarbon pyrolysis products.

A fully integrated model was presented in [277], where the necessary contents of carbon, hydrogen and oxygen are attributed to the sulfur reference species, and the corresponding formation of products containing these atoms is directly included in the sulfur kinetic mechanism. This proposed formulation dismisses any need to treat sulfur content separately from the remaining content of coal.

Using the integrated model and additional experimental data [293], Debiagi et al. [138,291] extended the model to include the heterogeneous conversion of sulfur in char. These latest efforts enabled the sulfur content to be fully integrated into the seamless framework of the CRECK-S-C model.

4.4.2. Kinetic model of nitrogen release during coal pyrolysis

The model describing the release of nitrogen during the pyrolysis of coal was proposed by Maffei et al. [276]. Similarly to the hydrocarbon pyrolysis model, fuel-nitrogen is characterized by reference species. Nitrogen is commonly found in coal as pyrrolic, pyridinic and quaternary chemical functionalities accounting for 50–80%, 20–40% and 0–20% of total nitrogen, respectively [294]. However, unlike sulfur, nitrogen content is not closely related to the coal rank, showing non-linear trends [49]. Maffei et al. [276] mention that more precise correlation can be obtained with respect to the coal maceral composition. This information is, however, not usually available and therefore currently not taken into consideration. Inorganic nitrogen can also be identified in ions such as nitrite, nitrates and ammonium, but only in small amounts.

Because of the complex distribution of nitrogen and uncertainties reported in the literature, Maffei et al. [276] propose a model that is supported by the analogue behavior between the released fraction of nitrogen and total fraction of released volatile matter, as reported by Chen and Niksa [84] and Perry and Fletcher [96]. On this basis and to maintain a consistency in the model, they adopted the same criterion for the nitrogen matrix already used to characterize the effect of the solid phase composition on the formation of hydrocarbon species [49,274]. Thus, four solid nitrogen reference species are taken: COAL-1-N, COAL-2-N, COAL-3-N and CHAR-N, closely tied to the reference coals COAL-1, COAL-2, COAL-3 and CHAR. Depending on the elemental composition (C/H/O) of the coal, the nitrogen content of each coal is characterized using the same distribution of the reference coals of the hydrocarbon fraction characterization (see Fig. 14).

The nitrogen in each of these reference species has different reacting paths during pyrolysis, releasing gases (NH_3 and HCN) and tars (N_{TAR}) and forming char structures in different proportions. Table 15 shows the list of species in this model, with a brief description and their corresponding category. The species N_{TAR} is lumped and represents a variety of species containing nitrogen, such as the typically found pyridine and pyrrole and their substituted compounds. Future extensions could also consider the direct release of N_2, which was observed during pyrolysis of low-rank coals and lignite [295–297].

The mechanism consists of a total of 11 species (4 reference species and 7 products), involved in 17 reactions [49,276]. The release of nitrogen components is assumed to occur along with coal pyrolysis. Thus, in accordance with the main model of coal pyrolysis, it was assumed that two different mechanisms, low and high temperature, compete during the release of the nitrogen components. Again, the low temperature mechanism accounts for the formation of metaplastic species, which are then released to the gas phase at higher temperatures. The metaplastic tar species G{N_{TAR}} reacts with CHAR-N through crosslinking and reticulation reactions, releasing additional NH_3 and HCN, decreasing the overall release of N_{TAR}, increasing the retention of nitrogen in the char. This process is hindered at high temperatures by the direct release of volatiles to the gas phase.

Similarly to the sulfur model, the first nitrogen model proposed was able to predict the distribution of nitrogen in the products based on the characteristics of coal and the operating conditions. Moreover, in the first formulation [276], nitrogen release from coal pyrolysis was presented as a standalone model, which was not completely compatible with the main coal pyrolysis model. The steps necessary to use the nitrogen model with the main coal model are analogous to those reported in Fig. 16 for sulfur.

A fully integrated model was presented in [277], where the necessary contents of carbon, hydrogen and oxygen were attributed to the nitrogen reference species, and the corresponding formation of products containing these atoms were directly included in the nitrogen kinetic mechanism, there was no need to treat nitrogen content separately from the remaining content of coal. Using the integrated model and the structure of the heterogeneous reactions reported in Table 13, the nitrogen model was extended to account for the heterogeneous conversion of nitrogen in char, and implemented in a carrier-phase DNS simulation of coal combustion in [292]. These latest efforts enabled the nitrogen content to be fully integrated into the seamless framework of the CRECK-S-C model.

4.5. Summary

The CRECK-S-C model provides a general, seamless kinetic framework for the coal conversion process. It provides a level of detail and accuracy that can be considered intermediate compared to the highly detailed network models (CPD, FG-DVC, FLASHCHAIN®) and the simple SFOMs (Single First-Order Reaction Models), C2SMs (Competing Two-Step Models) and DAEMs (Distributed Activation Energy Models) for pyrolysis, the same argument also applies for the detailed char

models. It offers an end-to-end approach, integrating the fuel handling and characterization, pyrolysis, char formation and annealing [274], the formation and release of SO_x [275] and NO_x [276] and their precursors, and char burn-out [278] in a seamless model. In particular, there is no conceptual gap between the pyrolysis and the char model. The model requires the elemental composition from ultimate analysis as input data. Coal is assumed to be a combination of a number of reference coals which can be used to describe the conversion of many typical coals. The model is only able to describe coals that fall within the characterization range.

The sulfur and nitrogen devolatilization processes, first made available as standalone submodels [275,276], were reformulated in [277] to allow their seamless integration into the main coal model. The integrated model was implemented and further validated for oxy-fuel conditions [298] and for the behavior of sulfur [138,291] and nitrogen [292] during coal conversion. A schematic summary of the necessary steps for using the integrated C/H/O/N/S model is represented in Fig. 17: (1) all sulfur content is characterized into the corresponding sulfur reference species, (2) then all nitrogen content is characterized and, to finish the characterization, (3) the hydrocarbon fraction is characterized. Having the complete characterization of the coal, (4) the integrated kinetic model is used to predict the distribution of products. This will enable a a comprehensive treatment of most thermo-chemical conversion steps in a single model that can be directly coupled to CFD.

It is important to note that char conversion is assumed to take place as a volumetric process, rather than a surface process. It is well known that the surface characteristics strongly influence the reactivity of the chars. However, the surface aspects are simplified, assuming average values, and lumped in the kinetic parameters. Moreover, pore diffusion is not explicitly treated. Therefore, for chars that have a significantly different porous structure and for different atmospheres (such as oxy-fuel combustion), the kinetic parameters must be adjusted to provide proper results.

5. Coupling detailed models for solid fuel kinetics to 3D-CFD applications

Despite the availability of advanced phenomenological and semi-empirical models for the thermo-chemical conversion of coal, as described in the previous sections, most CFD simulations reported even in the recent literature still use simplified approaches for modeling the solid phase kinetics. This can be attributed to the computational cost associated with the use of advanced models and to the challenges in prescribing accurate kinetics data for the feedstock employed. Considering that CFD simulations of pulverized coal combustion and gasification require substantially more computational resources compared to pure gas phase systems, a balance must be found between computational cost and prediction quality. Especially recently, substantial efforts have been reported in the literature to incorporate advanced solid fuel kinetic models into CFD simulations; these are reviewed in this section with a special focus on so-called indirect approaches, see below.

Similarly, it is interesting to note that a number of studies have been published recently dealing with improved numerical approaches for the description of gas phase processes in coal combustion/gasification, specifically turbulence modeling and turbulence-chemistry interaction, respectively. These are reviewed in Section 6.

Advanced approaches such as network pyrolysis models (Section 2), char conversion models (Section 3) or the CRECK approach (Section 4) provide information about the conversion rate of coal and yield of char, the composition of products and the evolution of the coal/char matrix. Different strategies have been developed for the coupling to CFD and they can be divided into two main categories:

1 Direct coupling by invoking the phenomenological model on a particle-by-particle basis for each time step of the CFD calculation and
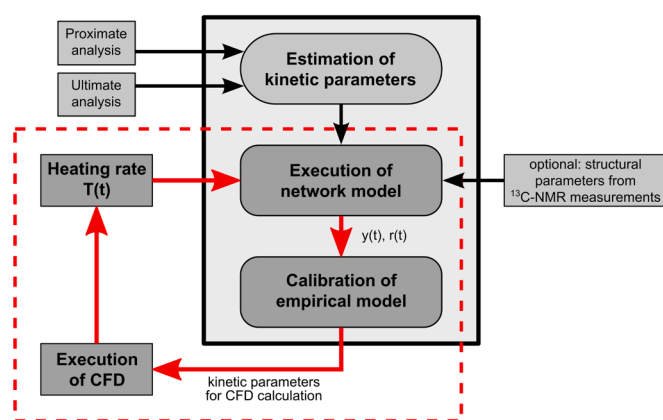

Fig. 18. Workflow of the Pyrolysis kinetic preprocessor (PKP). Adapted from Vascellari et al. [41].

2 Indirect coupling by successively invoking the solid fuel kinetic model and the CFD calculation (or information thereof) in an iterative routine.

Both approaches can predict the thermo-chemical conversion but have specific advantages and disadvantages. Direct coupling is favorable as it requires no a priori estimates (e.g. for the particle temperature history): this information is directly available for each particle during the simulation and the kinetic model can be directly applied. Depending on the model's complexity, this can lead to a substantial increase in computational resources. To the authors' best knowledge, only the following models have been used in direct coupling so far:

- CPD, e.g. see [11,18,307,308,299–306],
- FG-DVC, e.g. see [301],
- CRECK-S-C approach, e.g. see [309].

The source code of CPD is freely available, which in principle permits integration into CFD solvers, and was also implemented in the commercial code ANSYS Fluent. FG-DVC was implemented in the CFD solver PCGC [310]. The CRECK-S-C approach has no such restrictions since it uses a standard CHEMKIN format for the reaction mechanism. Other models are closed-source and can only be run within specific standalone programs or do not offer an open interface for CFD coupling.

By contrast, the indirect approach relies on a simplified representation of the detailed kinetic models. The parameters of the simplified approaches, e.g. single or multi-step models, are determined using the detailed models. Thus, these simplified models using global rates can be considered as a regression function with a certain number of kinetic parameters that must be adjusted. This usually requires the definition of relevant conditions, i.e. the particle heating rate, the temperature history, the atmosphere and so on. In the context of this paper, these conditions are usually extracted from corresponding CFD calculations.

It should be noted that these parameters can also be determined from experiments, which can be considered the traditional approach. However, this restricts the use to conditions that are close to the experimental conditions. These might not be close to what is relevant to the targeted application. More discussion can be found in the literature, e.g. in [42, 311] and references therein.

Widely used indirect approaches for pyrolysis and char conversion are discussed in Sections 5.1- 5.3 and selected references reporting their use are given. In addition, the commercial software PC Coal Lab® [108] provides automatic parameter determination for SFOM, C2SM and DAEM based on FLASHCHAIN® for pyrolysis. Further, a similar approach is provided for char conversion using CBK/E and CBK/G, which is also discussed below in Sections 5.4-5.5.

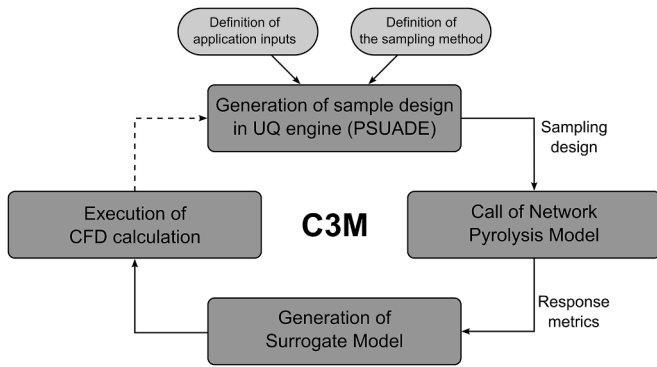Finally, machine learning has become a very promising alternative

Fig. 19. Workflow of advanced chemistry surrogate model in C3M toolbox.

for data-driven modeling in various scientific disciplines. Initial studies have been published for modeling solid fuel kinetics; for these applications the data is usually generated by running the detailed kinetic model, but in the future, it might be interesting to make use of the enormous amount of available experimental data. This is discussed in Section 5.6.

It is particularly important that the models correctly predict the ultimate volatile yields. Especially for high heating rates, only very few time steps are actually available in CFD to resolve devolatilization dynamics. Volatile yields are crucial because they partition the parent coal into fuels that burn in the order of milliseconds vs. char which burns in the order of seconds.

5.1. Pyrolysis Kinetic Preprocessor (PKP)

The Pyrolysis Kinetic Preprocessor (PKP) [41] was initially developed at Technical University Bergakademie Freiberg. Work continued at the Technical University Darmstadt and the University of Stuttgart. PKP is used to calibrate simple empirical pyrolysis models such as SFOM, C2SM or DAE models using results either from experiments or from advanced phenomenological models such as CPD, FG-DVC or FLASH-CHAIN®. The code is implemented in object-oriented Python language. The PKP method has been successfully used in several studies for calibrating the SFOM using the advanced phenomenological models CPD, FG-DVC and FLASHCHAIN® [312–315], and for calibrating the C2SM using the CPD, FG-DVC and FLASHCHAIN® models [128,316] to achieve favorable agreement with the experimentally observed volatile yield.

Taking into account one or more temperature histories for a coal particle $T_{p,i,j} = f_i(t_j)$, for each heating rate i and a discrete number of time steps t_j the single network pyrolysis models can calculate the yield of volatiles $Y_{i,j}^{net}$ and a pyrolysis rate using the following equation

$$r_{i,j}^{net} = \frac{dY_{i,j}^{net}}{dt} \tag{79}$$

The results of proximate and ultimate analyses of the feed coal are generally used to adapt the kinetic parameters of the phenomenological models. In a similar way to Eq. (79), the yield of volatiles and the pyrolysis rate can be determined for each heating rate i with an empirical model considering a general set of model parameters x_k. Taking into consideration N_{hr} particle temperature history and a discrete number of time steps $N_{t,i}$ for each heating rate i, the objective function OF is calculated as shown in the following equation

$$OF(x_k) = \frac{1}{N_{hr}} \sum_{i=1}^{N_{hr}} \left\{ \frac{\sum_{j=1}^{N_{i,j}} \left[Y_{i,j}^{net} - Y_{i,j}^{emp}(x_k) \right]^2}{N_{t,i} \left[\max_j \left(Y_{i,j}^{net} \right) - \min_j \left(Y_{i,j}^{net} \right) \right]^2} \right\} \tag{80}$$

The objective function can possess several local minima taking into account multiple particle heating rates. Therefore, the objective function is minimized with the use of a genetic algorithm [317]. This type of algorithm is capable of finding global minima. By contrast, local optimization tools such as gradient-based methods are less suitable to solve the problem on hand.

When this calibration method has been used previously, only single heating rates have been used for adaptation. However, the results of several studies [133,318] show that the operating conditions during pyrolysis have a strong influence on the calibration procedure. Therefore, PKP has been implemented with a calibration method using the data of many particle heating rates to account for local or particle-size-based differences in the reactor. Since the adaption of an empirical model in PKP requires knowledge about the conditions in the reactor, in general an iterative approach is chosen. Based on this procedure a representative particle heating rate from the CFD calculation is chosen. Finally, reliable pyrolysis parameters are derived.

The workflow of the PKP code is illustrated in Fig. 18.

The four sub-steps of the mechanism are:

1 Determination of the kinetic parameters of the network pyrolysis models based on the results of proximate and ultimate analyses, using the individual methods developed for single models;
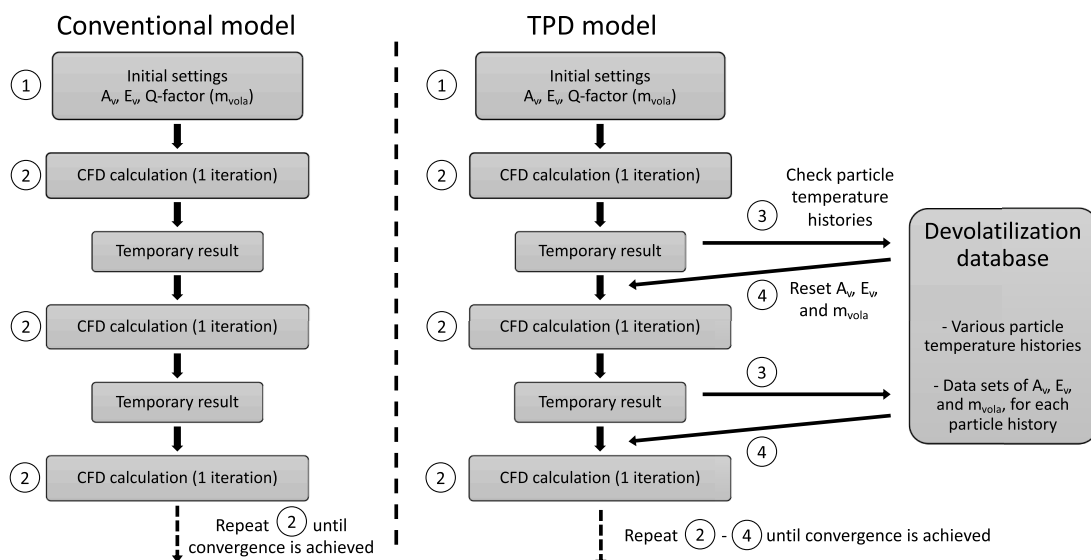

Fig. 20. Procedures for CFD simulation using conventional devolatilization models, i.e. the SFOM model (left), and the TDP model (right). Adapted from [321].

2 Estimation of yields and pyrolysis rates by the network models using the heating rates and, optionally for CPD only, results of the coal structure measurements by 13C-NMR spectroscopy;

3 Calibration of the empirical models, minimizing the objective function, defined in Eq. (80);

4 Execution of the CFD simulation using the kinetic parameters from the calibration procedure [41].

Finally, to achieve accurate heating rates for the CFD simulation, steps 2–4 are carried out iteratively until a converged solution is reached. It is particularly important to consider different particle sizes representative for the particle size distribution (PSD), since the final ultimate yield will strongly depend on this.

5.2. Carbonaceous Chemistry for Computational Modeling (C3M)

The Carbonaceous Chemistry for Computational Modeling, C3M, model was developed by the United States Department of Energy National Energy Technology Laboratory (NETL) [319]. C3M software interfaces with the kinetic packages PC Coal Lab® (Niksa Energy Associate), CPD (University of Utah) and FG-DVC (Advanced Fuel Research) and CFD softwares MFiX (NETL), ANSYS FLUENT (ANSYS) and Barracuda (CPFD). The C3M software provides the pyrolysis reaction rate, composition and yield for volatile gases and tar for use in CFD simulations. The MFiX Validation module in C3M allows users to perform virtual TGA experiments to evaluate the effect which operating conditions – such as the pressure, temperature and heating rates and fuel type – can have on pyrolysis reaction rates and yield, before CFD simulations are performed. The Uncertainty Quantification (UQ) module in C3M generates advanced chemistry surrogate models for pyrolysis rates and yields for use in CFD simulations [319,320]. A surrogate model constructed from data measured at different operating temperatures and heating rates, which accounts for local changes in the temperature and heating rate, can be more accurate than a single response model developed for a fixed heating rate and temperature. Therefore, C3M provides both direct and indirect coupling with the aforementioned kinetic software package.

The workflow for constructing surrogate models for pyrolysis in C3M is documented by Van Essendelft et al. [319] and is shown in Fig. 19. The first step required by the UQ module in C3M is to define the operating envelope of the reactor. Nominal operating values have to be defined, along with their operating range for input parameters such as the pressure, temperature, heating rate, particle size, among others. The input parameters can either be uniform, characterized by minimum and maximum values (epistemic), or expressed by a normal distribution, characterized by a mean and standard deviation (aleatoric). In the second step, the UQ software toolkit PSUADE, from the Lawrence Livermore National Laboratory, is used to generate a sampling space where each sample is a unique operating condition that the reactor encounters. In the third step, the chosen phenomenological pyrolysis model is launched by C3M for each of the sampling points. The fourth step involves constructing a response surface for the quantities of interest (QoIs), based on user-specified inputs. The QoIs can be the species yield and reaction rates as functions of input parameters such as temperature or heating rates. Finally, in the last step the application-oriented surrogate model is coupled to the CFD calculation. Since the dependencies of the pyrolysis rate and product yields on the heating rate and particle temperature are collected and stored in the easily and quickly accessible surrogate model, the CFD solver is capable of invoking the model for each particle individually time step by time step. As seen in Fig. 19, there may be a need to repeat Steps 1 through 5 if the original design of the experiment did not cover all possible operating conditions seen in the reactor. The surrogate model routine in C3M allows the toolbox to indirectly couple network pyrolysis models to CFD applications without needing to execute numerous iterations to achieve the desired accuracy.

5.3. Tabulated Devolatilization Process (TDP)

The TDP model was developed by Hashimoto et al. [321] at the Central Research Institute of the Electric Power Industry (CRIEPI) in Japan. TDP stands for Tabulated Devolatilization Process. It is used for coupling network pyrolysis models to CFD calculations to increase the level of detail and the accuracy of devolatilization description. In a similar way to the C3M model [319], Hashimoto et al. [321] pursue the same idea of combining the advantages of directly and indirectly coupling network pyrolysis models to CFD calculations. The routine they developed for the TDP model tries to avoid multiple iterations of the successive execution of the devolatilization database generation with TDP model and CFD calculations.

The development of TDP is presented in detail by Hashimoto et al. [321]. The TDP model for coupling phenomenological devolatilization models to CFD is schematically shown in Fig. 20 and is described in the following.

Initially, prior to the CFD calculation, data has to be collected for generating the devolatilization database. This includes typical devolatilization parameters such as the activation energy, pre-exponential factor and mass fraction of volatile matter in particle, for several particle temperature histories (particle temperature and heating rate). Both experimental and numerical data, e.g. obtained with network pyrolysis models such as CPD, FG-DVC and FLASHCHAIN®, can be used as inputs. The TDP model generates the devolatilization database in the form of a table connecting the various temperature histories and respective devolatilization parameters with each other.

The second step is to couple the generated table, including the devolatilization database, to the CFD calculation. In addition, an initial setting of devolatilization parameters is chosen for the first iteration of the CFD solver (i.e. steps (2-4) in Fig. 20.

The third step is the CFD simulation itself. After each iteration of the CFD solver, the TDP model analyzes the results for the particle temperature and heating rate from the last iteration and checks for the best fitting particle temperature history in the tabulated devolatilization database. The respective devolatilization parameters are applied in the next step of the CFD solver. Thus, the devolatilization parameters are updated for each particle by the TDP model. This is continued until convergence is achieved.

The TDP model allows phenomenological devolatilization models to be coupled to a CFD application using a modified indirect approach. The model's implementation tries to avoid using more than one iteration of the successive execution of the TDP model and CFD calculation. Similarly to C3M [319], the accuracy of predicted results after one run of the routine depends strongly on the generation of a representative devolatilization database.

Additionally, the validity of the proposed model is examined by the numerical simulation of an industrial-scale low-NO_x burner. In this simulation, the results of experiments are compared with CFD calculations employing the TDP model, the SFOM model proposed by Badzioch and Hawksley, and the C2SM model proposed by Kobayashi et al.. Further evaluation of the TDP model was conducted by Hashimoto et al. [318] on a laboratory-scale pulverized coal jet flame, and the simulation results were again compared to the experimental data and the results obtained from the conventional devolatilization models SFOM and

Table 16

Comparison between CBK/G and SNOI model.

Submodel	CBK/G	SNOI model
Heterogeneous surface reactions	LH mechanism	NthOR
Thermal annealing	✓	×
Pore evolution	RPM	RPM
Film diffusion	SFM	SFM
Ash inhibition	✓	×
Pore diffusion	PPPM	PPPM

C2SM. Through cross-comparisons, Hashimoto et al. [318,321] found that the TDP model can give better results compared to the other conventional models in predicting the particle velocities. They also reported that, compared to the turbulence model, the gas-phase combustion model and the radiation model, the devolatilization model has an important influence on particle velocity prediction. Recently, Takahashi et al. [322] applied the TDP model to predict soot formation characteristics in a pulverized coal jet flame using LES. In all the above simulations with TDP, the database for devolatilization was generated using the FLASHCHAIN® model.

5.4. Single n-th order reaction (SNOR) model for char conversion

Advanced char conversion models are capable of predicting char consumption by oxidation and gasification. The following section presents two approaches used to integrate such advanced char conversion kinetics into CFD, namely SNOR and SNOI [108,128].

SNOR stands for "single n-th order reaction". It builds directly on CBK/E [133] and CBK/G [126]. SNOR is incorporated into the commercial software package PC Coal Lab® distributed by Niksa Energy Associates LLC (NEA) [108]. Due to the complexity of the advanced CBK versions and the lack of a direct interface, they are not suitable for direct CFD applications. Instead, SNOR uses empirical global kinetics for the more mechanistic LH mechanisms, which are fitted using the results of CBK/E or CBK/G model. The derived global kinetics are valid for the defined operation conditions, e.g. temperature, pressure, etc., and the parent coal.

SNOR considers O_2 for oxidation reactions and CO_2, H_2O and H_2 for gasification reactions as reactants. For O_2 and H_2, the reaction rates are defined as

$$R_i = \vartheta R_i^\circ = \vartheta A_i \exp\left(-\frac{E_i}{R_G T}\right) P_{i,s}^{n_i} \tag{81}$$

with ϑ as an empirical fitting parameter, R_i° as the surface-based reaction rate without the influences of char aging or char structure changes, R_i as the reaction rate based on the outer particle surface, A_i, E_i and n_i as the pre-exponential factor, activation energy and reaction order of the *n-th* order global kinetic approach and $P_{i,s}$ as the reactant partial pressure at the char particle surface. For the reaction rates of CO_2 and H_2O, inhibition by the product species CO and H_2 is taken into account using additional terms

$$R_{CO_2} = \vartheta R_{CO_2}^\circ = \vartheta \frac{A_{CO_2}\exp\left(-\frac{E_{CO_2}}{R_G T}\right) P_{CO_2,s}^{n_{CO_2}}}{1 + K_{CO} P_{CO,s}} \tag{82}$$

and

$$R_{H_2O} = \vartheta R_{H_2O}^\circ = \vartheta \frac{A_{H_2O}\exp\left(-\frac{E_{H_2O}}{R_G T}\right) P_{H_2O,s}^{n_{H_2O}}}{1 + K_{H_2} P_{H_2,s}} \tag{83}$$

Fig. 22. Total volatile yield predicted by network models for Utah bituminous coal considering different heating rates. Reprinted with permission from [41]. Copyright 2013 Elsevier Ltd.

with K_{CO} and K_{H_2} as pre-exponential factors of the inhibition term. The empirical fitting parameter ϑ describes the influence of the main inhibition mechanisms which decelerate the char conversion rate as the carbon conversion level X_C increases. The inhibition mechanisms taken into consideration are the aging of char (thermal annealing and ash inhibition) and the changes to the char structure, e.g. density and porosity. The empirical parameter ϑ is defined using a fifth-order polynomial expression depending on the carbon conversion level X_C

$$\vartheta(X_C) = \alpha_0 + \alpha_1 X_C + \alpha_2 X_C^2 + \alpha_3 X_C^3 + \alpha_4 X_C^4 + \alpha_5 X_C^5 \tag{84}$$

with α_j *(j = 0 − 5)* as regression coefficients.

5.5. Single n-th order intrinsic (SNOI) model for char conversion

In addition to the SNOR versions of CBK/E and CBK/G, a second approach was developed to couple phenomenological models to CFD applications. A reduced version of the CBK models is applied: the so-called single n-th order intrinsic (SNOI) model [128]. SNOI uses only certain submodels of CBK/G, summarized in Table 16.
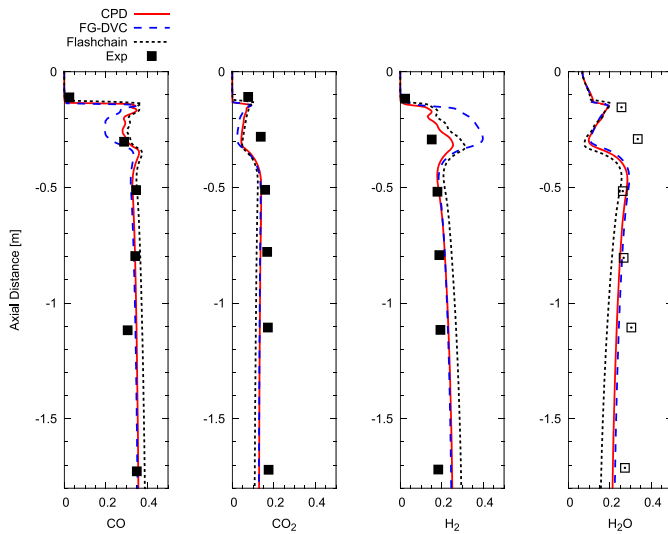

Fig. 21. Left: Calculated volatile mass fraction from CPD and an optimized two-step model for four heating rates. Right: Calculated ultimate volatile yield vs. heating rate using CPD and the two-step model. Reprinted with permission from [48]. Copyright 2016 Elsevier B.V.
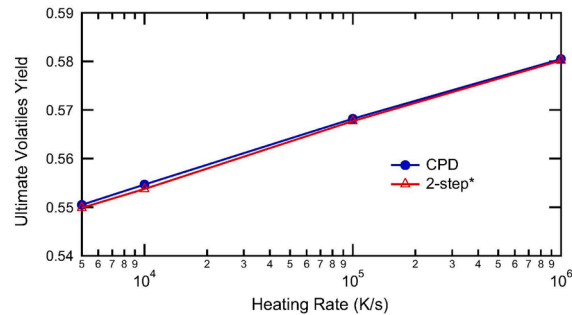
Fig. 23. Utah bituminous coal: CO, CO_2, H_2 and H_2O molar fraction along the axis. Results of C2SM calibrated with CPD, FG-DVC and FLASHCHAIN compared to experiments [327]. Experimental values for H_2O are reported with hollow symbols because they are not directly measured. Reprinted with permission from [41]. Copyright 2013 Elsevier Ltd.

SNOI uses a global kinetic approach instead of the more mechanistic LH reaction mechanism. The calibration of the kinetic constants demands less effort compared to a LH reaction mechanism.

Another simplification is that H_2 is neglected as a reactant since the gasification kinetics of H_2 are several orders of magnitude smaller than the oxidation kinetics or even gasification kinetics of CO_2 and H_2O. Therefore, the number of equations in the global kinetic mechanisms is reduced to three reactions. The formulation of the reaction rates is identical to the equations used in the SNOR versions.

Neglecting ash inhibition and thermal annealing by removing the respective submodels considerably reduces the computational effort. Because SNOI was mainly developed to model char gasification, the negligence of ash inhibition can be justified as explained in Section 3. Thermal annealing occurs when particles are exposed to high temperature levels. With respect to CFD simulations of gasifiers, the coal/char particles are much closer to the burner flame during pyrolysis than during char conversion. This results in an exposure to high temperature
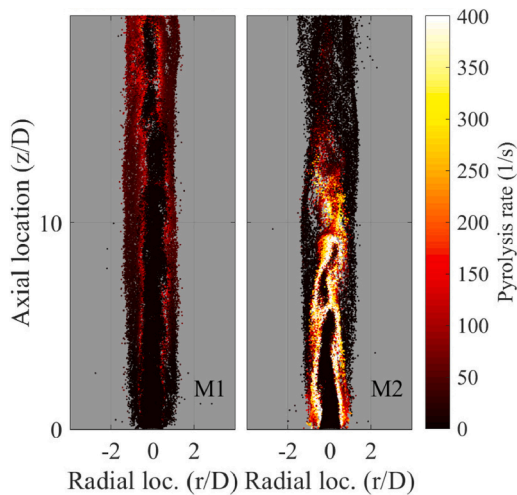
Fig. 24. Instantaneous stochastic fuel particle pyrolysis rate. Results are for Cases M1 and M2 as indicated. The images are clipped at z/D = 20 to focus on the upstream region dominated by pyrolysis. Reprinted with permission from [330]. Copyright 2019 Elsevier Inc.

levels for a short time only, which defines the reduction in particle reactivity.

5.6. Machine learning approaches for solid fuel kinetics

Similarly to the aforementioned PKP model for devolatilization and the SNOR and SNOI models for char reactions, machine learning is an another option and a strongly emerging scientific field aimed at fitting detailed solid fuel kinetics to a reduced-order model based on a database generated from the network models such as FG-DVC, CPD or FLASH-CHAIN® for devolatilization and CBK/E and CBK/G model for char surface reactions. Some initial applications of machine learning approaches for solid fuel kinetics are reviewed next.

In machine learning approaches, the relevant information, such as the heating rate or the ultimate and proximate analyses are the inputs for the specific machine learning algorithms (i.e., unsupervised and supervised machine learning methods), while the outputs can be the rates of kinetic parameters. Abbas et al. [323] were the first to use a machine learning method employing neutral networks (NNs) to predict the kinetics of devolatilization. The input parameter was the temperature for charactering the heating condition, while the output was the weight loss, which is related to the kinetics of devolatilization. The NN approach was implemented in the CFD simulations, and comparable results were obtained with those obtained using the detailed devolatilization method FLASHCHAIN®. Xing et al. [324] further extended the work of Abbas et al. [323] by considering the different heating rates and coal types (determined by the ultimate and proximate analyses) as input parameters for the machine learning employing Artificial Neural Networks (ANNs). The output is the kinetics parameters for the devolatilization method of C2SM, which can be directly used in the CFD simulation. Compared to the CPD model, the ANN model shows a competitive prediction capability for the total volatile release and release rates. The results showed that the heating rate has the most significant effect on the pre-exponential factor, while the coal type directly influences the activation energy and the total volatile yield. Recently, Debiagi et al. [325] developed a reduced order model for devolatilization and char conversion processes based on the supervised machine learning method employing HDMR (high-dimensional model representations by Rabitz et al. [326]). The database for the machine learning is generated based on single coal particle combustion for various operating conditions extracted from the LES results of a pulverized coal combustion chamber, taking all the pyrolysis and char conversion processes into account. A detailed solid fuel kinetic model (CRECK-S-C model) (Section 4) was employed to generate the database for training and testing. The input parameters include the temperature, heating rate, O_2 mass fraction and residence time, while the outputs include the mass loss, gas/tar pyrolysis rates and char oxidation rate. The results showed that the HDMR-based supervised machine learning approach is suitable for generating reliable, computationally efficient models to describe the solid fuel kinetics.

Overall, the recent results have shown that the approaches based on machine learning are promising for implementing detailed solid fuel kinetics in CFD simulations of the pulverized coal combustion and gasification applications.

5.7. Selected comparisons of solid fuel kinetics and their application in CFD

In the following, selected examples from the literature are presented where different models for the solid fuel kinetics are compared with a particular focus on their use in a CFD simulation.

Richards and Fletcher [48] investigated six different empirical pyrolysis models and compared the results to CPD. Specifically, they looked at the extent to which the models were able to reproduce the following two trends: increasing devolatilization temperature with increasing heating rate, and increasing ultimate volatiles yield with

increasing temperature. They showed that a modified two-step model with 18 adjustable parameters (referred to as RF in the paper) provides a good approximation for a wide range of temperatures and heating rates. This is illustrated in Fig. 21. They also showed that single-step models (SFOM) cannot adequately match CPD results for the range of conditions considered.

A direct comparison of CPD, FG-DVC and FLASHCHAIN for four different coals was conducted in Vascellari et al. [41] under entrained-flow gasification conditions. Realistic heating rates were obtained from a CFD simulation and used to predict the volatile yields. An example result for Utah bituminous coal is shown in Fig. 22. While the general trend is similar for the models, the final yield can differ significantly. All three network models were then used to adjust the parameters of C2SM for all four coals individually. CFD simulations were carried out and compared to experiments, see Fig. 23, which shows results for the Utah bituminous coal. The relevance of the pyrolysis model can be seen directly, and differences in the predictions of the rate and yield also lead to differences in the local distributions of CO, CO_2, H_2 and H_2O.

Interestingly, good agreement was obtained between the experimental data and the CFD simulations for three of the four coals. Significant deviations were only found for North Dakota lignite. This discrepancy is partly due to the fact that the kinetic data for the network models had to be extrapolated for the specific O:C and H:C ratio of this coal. This emphasizes the importance of kinetic data for solid kinetics for CFD simulation.

Specifically with respect to entrained flow gasification, a recent article by Mularski et al. [328] reviewed the importance of different models in CFD. In agreement with the above results, they concluded that the proper modeling of devolatilization is critical for an accurate estimation of flame stabilization, structure, and lift-off. The modeling must take into account the fact that the devolatilization kinetics and yield strongly depend on the heating rate. While the advanced standalone network pyrolysis models provide accurate results for a wide range of operating conditions, the kinetic parameters of the empirical models must be properly calibrated to obtain consistent results. With respect to char conversion, detailed models are required, as presented in Section 3, one distinctive feature of gasification is that it occurs essentially in Regime II (pore-diffusion controlled). For char conversion, the authors also concluded that the direct application of the detailed models in CFD is very challenging. As with pyrolysis, appropriate calibration procedures can be used for the simpler models.

Further work, especially using the fully coupled models in multidimensional CFD simulations, has shown the benefits of using the detailed models to fit the parameters of empirical pyrolysis models. Shamooni et al. [329] fitted C2SM with the CRECK-S-C model and obtained good results. Rieth et al. [18] confirmed that the direct use of a network model in CFD (here CPD) can be advantageous, but they also concluded that suitably adjusted empirical models can also provide good results.

Zhao et al. [330] used CPD-fitted single and two step models in an LES of a pulverized coal jet flame. Using the single step model, pyrolysis occurs too rapidly, which directly influences the flame structure. This is illustrated in Fig. 24, where the single-step approach (left, M1) and the two-step approach (right, M2) are compared.

6. Gas phase modeling of pulverized coal combustion and gasification in CFD

While the previous Section discussed the integration of advanced models for solid phase kinetics in CFD, this Section is concerned with the treatment of the gas phase. This includes two elements: (1) the modeling of the turbulent flow and mixing and (2) the coupling of turbulence and gas phase chemistry, which is usually referred to as turbulence-chemistry interaction (TCI). TCI is discussed both in terms of combustion and pollutant formation.

It is important to note that many studies using either advanced approaches for the flow field (Sections 6.1 and 6.2) or for TCIs (Sections 6.3 and 6.4) do not necessarily use advanced models for the solid phase. In fact, coupling and employing advanced models for both the gas and solid phase really constitutes the next step in the CFD modeling of pulverized coal combustion or of solid fuel combustion in general. The relevance of high-fidelity simulations of PCC was also highlighted in a recent article by Cai et al. [331], which emphasized the value of LES and DNS despite the high computational cost.

6.1. Modeling of the turbulent gas phase

CFD simulations of turbulent combustion and gasification processes can be performed at three different hierarchy levels: Direct Numerical Simulations (DNS), Large Eddy Simulations (LES), and Reynolds-Averaged Navier–Stokes (RANS), respectively. These levels differ in the treatment and resolution of the turbulent fluid motion and mixing. In DNS, all the instantaneous heat and mass balance equations are fully resolved. In this way, all the turbulence scales are accounted for and the effects on the reacting flows are captured. However, this approach is computationally very costly, which currently restricts its application to simplified geometries with reduced Reynolds numbers. The continuous evolution of computational power and software is progressively raising the possibilities of applying such simulations to more realistic settings. In LES, the turbulence is separated into two scales, which are defined by the filter size. The turbulent motion taking place on scales larger than the cut-off length of the filter size is explicitly calculated, while the smaller scale is described using a sub-grid scale (SGS) for sub-filter models. When the cut-off length in a LES tends to zero, the simulation approaches a DNS. Besides the simplifications, this approach allows complex features to be captured, such as unsteadiness, ignition spots, quenching and combustion instabilities. RANS simulations, on the third level, describe the turbulent motion by averaging the instantaneous balance equations. Turbulence models must account for all turbulent motions, further drastically reducing the required CPU power compared to LES.

6.2. RANS, LES and DNS of pulverized coal combustion and gasification

RANS has been the most widely used approach in the CFD of pulverized coal combustion for many decades, with an enormous breadth of works reported in the archival literature. Many studies using the advanced models for solid fuel kinetics discussed in the previous sections are in fact RANS-based [12,41,45,318,321,332–334]. In the following, we concentrate on newer studies with LES and DNS.

6.2.1. Large Eddy Simulation - LES

Compared to RANS, LES offers many advantages as it resolves large-scale unsteady motions, which are important for flame propagation and stabilization. Because of this, more and more investigations are now reported using LES for pulverized coal combustion. There are also a few DNS studies on simplified configurations. DNSs are usually not intended to simulate entire burners or even furnaces; rather, they provide highly resolved reference data especially for TCI, as discussed in Sections 6.3 and 6.4.

Kurose and Makino [335] conducted the first LES to model pulverized coal combustion, investigating interactions between dispersion, evaporation, and coal combustion. SGS turbulence and combustion were described with the Smagorinsky model and the conserved scalar approach, respectively. Watanabe et al. [336] conducted a LES of a swirl-stabilized pulverized coal combustion furnace with a complex burner. The simulation results obtained with LES were compared to the available experimental data and the RANS simulation results. The comparisons showed that compared to the RANS results, the LES results are closer to the experimental data, especially in the recirculation zone. The review paper by Kurose et al. [337] discussed the progress of pulverized coal combustion CFD in terms of RANS and LES, concluding that

LES is far superior to RANS simulations and is expected to become a useful tool for developing and designing new combustion chambers in the near future. Yamamoto et al. [338] conducted a LES of a pulverized coal flame ignited by a preheated gas flow. The simulation results were compared to the experimental data and the RANS simulations at different inlet stoichiometric ratios. They found that the lift-off heights predicted using LES show better agreement with the experimental data when compared to the RANS results. To improve the prediction capability of the single reaction rate devolatilization model, Yamamoto et al. [338] introduced a factor modifying the frequency factor, which is a function of the fraction devolatilized. Franchetti et al. [339] conducted a LES of a laboratory-scale pulverized coal flame using the Eddy-Break-Up (EBU) model [340] and the simplified coal combustion submodels. The simulation results, including the particle velocities, particle temperature and species concentrations, were compared to the experimental data. They found that the particle velocities and particle temperature can be well predicted by the coal combustion submodels they employed. However, large discrepancies can be observed for the species concentrations, which was attributed to the EBU model employed, as infinitely fast chemistry is assumed. Wen et al. [341] conducted a LES for the same burner as in [339] using the EBU model and the simplified coal combustion submodels. To consider the SGS effects of turbulence velocity and the scalar fluctuation of the gas flow on the coal particles, the so-called velocity-scalar joint filtered density function (VSJFDF) model [342] was employed. The simulation results were compared to the experimental data and the results reported in [339]. Comparisons showed that the VSJFDF model can predict not only the influence of the SGS turbulence and scalar fluctuation on the particles, but also the effect of the subsequent coupling interactions between the large-scale flow field, SGS turbulence and the particles on the flame configuration. Further, it was found that the species concentrations still cannot be correctly predicted using the EBU model, and finite-rate chemistry models were recommended. Stein et al. [343] compared the LES results from three different research groups, including Freiberg University (FG), Imperial College (IC) and Stuttgart University (ST), for the same laboratory-scale burner. The coal combustion submodels and parameters used by different groups were unified for comparison, and the groups differed in terms of the code base and the treatment of the coal particles (Eulerian in IC, and Lagrangian in FG and ST). The comparisons showed that the velocity statistics can be well predicted by all simulations, while the particle temperature and species concentrations exhibited large discrepancies due to the EBU model employed. The common finding of the aforementioned works is that the infinitely fast chemistry model cannot produce good predictions of the species concentrations, and finite-rate chemistry models are required. In recent years, various advanced TCI models that were initially developed for gas and spray combustion have been extended to study pulverized coal combustion in the frameworks of RANS and LES, see Sections 6.3 and 6.4. For gasification, Abani and Ghoniem [344] conducted both RANS and LES for the Brigham Young University gasifier. The Lagrangian-Eulerian method was used to describe the particle trajectory in the flow field, the devolatilization rate was described with the single kinetic rate model, while the char surface reaction rate was characterized with the model proposed by Zhang et al. [345], in which the char surface reaction was described with the moving flame front suitable for CFD simulations. The main finding of this work is that the LES performs much better than the RANS in terms of the penetration of the volatile gaseous jet and the radial distribution of species. Kumar and Ghoniem [307] conducted both RANS and LES for entrained flow gasification in a sudden expansion geometry using multi-physcis models. The devolatilization rate was described with the CPD model embedded in the Fluent software, and the char surface reaction rate was characterized with the model proposed by Smith et al. [346].

6.2.2. Direct Numerical Simulation - DNS

Full DNS is the paradigm for resolving all turbulence scales (from integral to Kolmogorov) and all near- and intra-particle processes, something that is still impossible for pulverized coal combustion at present. Specifically for particle combustion, DNS of the carrier phase (CP-DNS; the particles are not fully resolved on the grid and are usually modeled as point particles) is a promising method since the computational cost is affordable, and the obtained DNS dataset can be used to analyze the pulverized coal combustion characteristics and to develop new coal combustion submodels. Luo et al. [347] conducted the first CP-DNS of pulverized coal combustion in a hot vitiated co-flow. It was found that in the upstream region, the reaction zone is scattered and an individual particle combustion mode is formed, while in the downstream region, the reaction zone is more continuous and the group combustion mode is observed. Hara et al. [19] conducted a CP-DNS for a laboratory-scale pulverized coal jet flame employing a global volatile matter reaction scheme. Comparisons with the experimental data showed that the particle velocities and the particle preferential motions agree with the experimental data. Muto et al. [348] studied the effect of particle swelling on pulverized coal combustion based on the DNS dataset generated by Hara et al. [19]. They found that the swelling due to devolatilization and char surface reactions does not have a significant effect on the distribution of the coal particle temperature. In the above two DNS datasets, the global chemical reaction mechanisms were used to save computational cost. Recently, Rieth et al. [349] conducted a DNS of a turbulent pulverized coal flame stabilized in a turbulent mixing layer with a detailed chemical reaction mechanism containing 52 species and 452 elementary reactions [350,351]. The DNS results showed that heat is initially released in lean conditions, both premixed and non-premixed combustion modes exist in the combustion field, and transient states such as local extinction and re-ignition prevail in the pulverized coal flame studied. Based on the DNS dataset, Rieth et al. [352] evaluated the performance of the steady flamelet/progress variable (FPV) approach [353] through both *a priori* and *a posteriori* analyses. The *a priori* analysis showed that the flamelet library and trajectory variables employed are suitable for modeling complex pulverized coal flames, while the *a posteriori* analysis produced similar results, although with a larger deviation compared to the *a priori* analysis. Wen et al. [354,355] further conducted comprehensive analyses of the DNS generated by Rieth et al. [349] using flamelet tabulation methods, focusing on multi-mode combustion, transient effects, strong heat losses and reoccurring issues in flamelet modeling for pulverized coal combustion. The suitability of the premixed-flame-based flamelet model and non-premixed-flame-based flamelet model was evaluated in [354] by means of *a priori* analysis, and the relevance of the transient states in the pulverized coal flame was studied using *budget analysis*. The results showed that both flamelet models make good predictions in the respective combustion zones, while the non-premixed-flame-based flamelet model performs better overall than the premixed-flame-based flamelet model. The unsteady states can be represented to some extent by the steady flamelet models since the unsteady terms of the trajectory variables are available in the flow field. Extended flamelet models that can consider strong heat losses and multi-combustion modes were developed in [355]. The results showed that the extensions can account for high heat losses in the pulverized coal flame studied, and the performance of the multi-mode flamelet model strongly depends on the definition of the combustion mode index. Wan et al. [32] conducted DNS to investigate the alkali metal emissions in early-stage pulverized coal combustion. The suitability of the premixed-flame-based flamelet model for predicting pulverized coal combustion was also evaluated. Recently, Shamooni et al. [292] conducted a CP-DNS of early-stage pulverized coal combustion with fuel-bound nitrogen, focusing on the detailed NO_x formation. The computational setup is a turbulent mixing layer, the same as that in [349]. Both volatile-N and char-N were considered in the DNS, with the NH_3, HCN and C_5H_5N representing the light and lumped nitrogenated tar in volatile matter. The results showed that NO is formed as soon as the small groups of particles are entrained into the lower hot burnt gases, then the volatile ignition begins. The results also showed

that the contribution of NO_2 to total NO_x is limited, and NO is mainly formed from the fuel-NO, with a limited thermal Zeldovich mechanism and the prompt mechanism. In fact, the Zeldovich mechanism does not contribute to the formation of NO but to its consumption in the fuel-bound nitrogen pulverized coal flames.

Tufano et al. [314,315] conducted DNS for single coal particles and particle arrays in laminar and turbulent flows considering heating-up, devolatilization, ignition and volatile combustion. The DNS fully resolves the particle boundary layers, the flame structure and the smallest flow scales. The first part [315] investigated how the inter-particle distance (L_x) influenced the flame interaction. The analysis showed that depending on the inter-particle distance, different combustion regimes can be observed, ranging from isolated burning for large L_x to group combustion for small L_x. The second part [314] investigated the effects of the particle Reynolds number and turbulence, showing that increased turbulence intensity delays the ignition of single particles. Further, they found that the steady flamelet model works well in reproducing the DNS data for lower turbulence intensities, while for high Reynolds numbers, significant discrepancies exist due to the multi-dimensional effects (e.g., curvature etc.). Due to the different extents of interaction of the different coal particle flames, the turbulence slightly promotes the mass release for the particle set furthest upstream, but considerably delays the mass release for the downstream particles.

6.3. Turbulence-chemistry interaction (TCI) for coal combustion and gasification

As mentioned above, the second challenge is to model turbulence-chemistry interaction, something that has been a topic of active research for turbulent gas phase combustion for many decades, as evidenced e.g. by the TNF International Workshop on Measurement and Computational Turbulent Flames [356]. Many advanced models have been developed and applied. In the last decade, an increasing number of studies have worked on transferring these findings to solid fuel combustion, which is discussed in this section.

In previous studies [322,339,341,343,357–359], simple gas combustion models based on the assumption of infinitely fast chemistry, such as the EBU model [340], the eddy dissipation concept (EDC) model [360], the partially stirred reactor (PaSR) model [361], or the scale similarity filtered reaction rate model (SSFRRM) [362], were generally used for turbulent pulverized coal combustion. It is only in recent years that advanced gas combustion models such as the transport probability density function (PDF) model [363], the flamelet model [364], and the conditional moment closure (CMC) model [365] – all initially developed for gas combustion – have been extended to simulate turbulent pulverized coal combustion. In the following, progress on the development of gas combustion models for pulverized coal combustion is reviewed.

6.3.1. Eddy Break-Up model (EBU)

The EBU model was initially proposed by Magnussen [340] in the context of RANS. Zhou et al. [366] and Hu et al. [367] proposed a straightforward extension for LES by introducing the filtered strain rate as a means of computing the flow timescale. The EBU model assumes that the chemical timescale is infinitely small, and the chemical reaction rate purely depends on the mixing rate. In previous works on the simulation of pulverized coal combustion, the common finding is that the EBU model over-predicts the consumption rate of reactants, and generally over-predicts the products' concentration.

6.3.2. Transport Probability Density Function model (PDF)

To overcome the limitations of the EBU model, some gas combustion models based on finite-rate chemistry have been developed for modeling pulverized coal combustion. Stöllinger et al. [21] first extended the transported PDF model for pulverized coal combustion in the context of RANS. To treat the devolatilization and char surface reaction separately, two mixture fractions were introduced to describe the mixing process.

The gas phase and particle phase are treated with two separate PDF transport equations by means of stochastic Lagrangian methods. For the solid phase, they adopted the Distributed Activation Energy Model (DAEM) [115] to characterize the devolatilization rate, and the intrinsic model proposed by Smith [145] to characterize the char surface reaction rate. In the DAEM model, the different species compositions in volatile matter follow the first-order decomposition reactions with the same pre-exponential factor and activation energy, distributed according to a Gaussian distribution. The transported PDF model which was developed coupled the simplified solid phase models and was applied in simulations of a semi-industrial-scale furnace. The simulation results were compared to the available experimental data. Overall agreement was achieved between the measurements and simulation results for both the gas phase and the coal particles. The results also showed that the performance of the proposed transported PDF model is sensitive to the models for the coupling source terms in the governing equation. One possible limitation of the method developed by Stöllinger et al. [21] is that the assumption of local equilibrium chemistry it made might not be sufficient for predicting slow reacting species such as CO. To overcome this limitation, Zhao and Haworth [12] reformulated the transported PDF model by adopting a consistent hybrid Lagrangian particle/Eulerian mesh algorithm to solve the PDF transport equation based on finite-rate chemistry. In their work, they tested both the single-rate devolatilization model and the devolatilization model with two competing rates, using the original parameters proposed by Kobayashi et al. [65] . The conventional diffusion-kinetic-controlled surface reaction model proposed by Baum and Street [368] was adopted with the assumption that char is directly converted to the final product, CO_2. The newly developed model was evaluated by simulating two independent laboratory-scale pulverized coal jet flames. For both flames studied, the baseline model offered good predictions of the measured mean and RMS particle axial velocity, while the predicted particle temperature and species concentrations still showed large discrepancies, which were attributed to the uncertainties in experimental data. Recently, Zhao et al. [330] developed a two-phase multiple mapping conditioning/large eddy simulation (MMC-LES) model for turbulent pulverized coal combustion. The MMC-LES model includes an Eulerian LES for the flow field, a stochastic Lagrangian particle scheme for the turbulent composition and an inertial Lagrangian scheme for the fuel particles. As in the work by Zhao and Haworth [12], both single and two-order reaction rates for devolatilization were evaluated, with the volatile matter assumed to be either a combination of light gases or pure methane. The char surface reaction was neglected for the specific pulverized coal flame studied. The performance of the MMC-LES model was applied to a laboratory-scale turbulent pulverized coal flame studied by Zhao and Haworth [12]. The predictions were found to be in good overall agreement with the experimental data and comparable to previously reported LES results for the same target flame with CP-DNS results [19].

6.3.3. Flamelet models

Like the transported PDF model, the flamelet model [364] is another promising TCI approach. Several groups have contributed in the last decade in that respect. One particular advantage of the flamelet approach is that it can consider detailed gas phase chemistry with a reasonable computational cost. Flores and Fletcher [369] were the first to introduce a flamelet-based model for describing turbulence-chemistry interactions in turbulent pulverized coal flames. This flamelet-based model was developed based on two mixture fractions, which were used to describe the mixing of volatile matter and char off-gases with the oxidizer separately. The model based on two mixture fractions was found to perform better than the single-mixture-fraction method in predicting the NO concentration. Vascellari et al. [370] introduced the unsteady flamelet concept to model the ignition delay time of a single coal particle in a laminar configuration, and the flamelet predictions were compared to the available experimental data. Further, Vascellari et al. [371] reformulated the unsteady flamelet model based on a new

analytical expression of the scalar dissipation rate in the context of the flamelet/progress variable (FPV) approach [353]. The suitability of the unsteady FPV approach was evaluated by comparing it against the detailed chemistry solutions and the experimental data using both *a priori* and *a posteriori* analyses. The comparisons showed that the FPV method is able to correctly reproduce the flame structure before and during the ignition process. Messig et al. [313] evaluated the suitability of the premixed-flame-based flamelet model and the non-premixed flamelet model for a counterflow pulverized coal flame, which was experimentally studied by Xia et al. [372]. Further, the importance of interphase heat transfer in the flamelet model was identified, and the necessity was recognized of introducing the total enthalpy in the flamelet model. The results showed that the non-premixed-flame-based flamelet model performs better overall than the premixed-flame-based flamelet model, especially for fuel-rich conditions. In refs. [313,370, 371], only the devolatilization process was considered, and accordingly, the flamelet model was formulated based on a single mixture fraction. Recently, Vascellari et al. [373] extended the flamelet model to include the context of two mixture fractions in order to consider both the devolatilization and char surface reactions. The performance of the multi-stream flamelet model was evaluated in a pulverized-coal stagnation flame by comparing it with the detailed chemistry solutions and the experimental data. The comparisons showed that the proposed multi-stream FPV model can accurately predict the main features of coal combustion, with only minor issues related to the manifold used to build the look-up table.

Watanabe and Yamamoto [374] independently extended the flamelet concept to model turbulent pulverized coal combustion in the context of DNS, where both the devolatilization and char surface reactions were considered with two mixture fractions as in [369]. The flamelet model was developed based on the FPV approach [353], and the performance of the extended FPV approach was evaluated by comparing it against the detailed chemistry solutions in terms of the instantaneous distributions of CO_2 and OH mass fractions, and particle temperature. Watanabe et al. [375] further extended their FPV model to the context of LES to predict ignition and extinction phenomena in a laboratory-scale coal jet flame and a large-scale test furnace. To consider moisture evaporation, the extended FPV model was based on three mixture fractions, used to describe mixing among the coal moisture, volatile matter and char off-gases, respectively. It was found that for the laboratory-scale coal jet flame, the profile of the ratio of coal burnt on the central axis of the jet flame predicted by the flamelet model agrees with the measurement, while for the large-scale test furnace, the unstable flame state occurring at a lower coal feeding rate can be reproduced by the extended FPV model.

A series of DNS and LES works on flamelet modeling have been published by Wen et al. [13,354,355,376–382]. At first, Wen et al. [383] reformulated the flamelet model developed by Watanabe and Yamamoto [374] in terms of the definition of the trajectory variables and the flamelet table generation, based on the detailed analysis of pulverized coal combustion characteristics in a laminar counterflow flow [13]. The reformulated flamelet model was also extended in the context of LES to simulate the laboratory-scale pulverized coal jet flame [377] and the semi-industrial-scale furnace [376]. For the sake of describing the complex configurations in the industrial burners, the flamelet model initially developed for a two-fuel-stream configuration was further extended to include the context of multi-stream, while the extended multi-stream flamelet model was evaluated in the laboratory-scale piloted pulverized coal jet flame [380] and the semi-industrial-scale furnace [376]. In the pulverized coal combustion system, both premixed and non-premixed combustion modes can be observed [19,349]. To adapt to the multi-combustion modes in the pulverized coal flame, Wen et al. [355,378] coupled the premixed-flame-based flamelet model with the non-premixed-flame-based flamelet model by making use of the combustion mode index. In the premixed flame reaction zone, the thermo-chemical quantities are extracted from the premixed flamelet library, while in the non-premixed flame reaction zone, the non-premixed flamelet library is accessed. Recently, the flamelet model has been extended to describe the pollutant formation in a pulverized coal flame [381,382]. In [381], the performance of the flamelet model extended to predict NO_x was evaluated in laminar counterflow flames for different coal types, while in [382], the extended flamelet model for predicting SO_x was also evaluated in laminar counterflow flames. The details of these two works will be described in Section 6.4 . Recently, Wen et al. [384] further extended the multi-stream flamelet model to cover pulverized coal combustion in an oxy-fuel atmosphere. Both NO_x and SO_x emissions were considered in the extended flamelet model, which was applied to a laboratory-scale swirl-stabilized pulverized coal burner [385] specifically designed for oxy-fuel atmospheres.

Rieth et al. [18,352] independently transferred a non-premixed flamelet model to pulverized coal combustion. They first used the scalar dissipation rate [17,18], and later the progress variable in the FPV framework [352]. The performance of the flamelet model they developed was first evaluated in a semi-industrial pulverized coal furnace for which comprehensive experimental data is available [17]. The predicted averaged values for the velocities, species concentrations and temperature were found to agree with the experimental data, validating the suitability of the flamelet model developed. Rieth et al. [18] further extended the flamelet model to couple it with the CPD devolatilization model [50] for predicting the devolatilization rate. The performance of the extended flamelet model was evaluated in a laboratory-scale pulverized coal jet flame, and the simulation results were compared to the experimental data and the results predicted with the fitted simplified devolatilization models based on the single first-order reaction (SFOR) [63] and two competing rates (CRM) [65]. The results showed that the direct CPD model has a direct effect on the individual particle level, but a well-fitted SFOR model can yield similar predictions. Due to the other effects compensating for the under-predicted devolatilization rate by the CRM model (error compensation), the simulation results predicted by the CRM model showed improved agreement with the experimental data. Recently, Rieth et al. [352] extended the flamelet model to include the context of the FPV approach, and the extended flamelet model was evaluated in a turbulent pulverized coal flame stabilized in a mixing layer by means of both *a priori* and *a posteriori* analyses. The results showed that the flamelet model performs well in the lower flame (of the DNS studied), where the non-premixed combustion mode is dominant, while there are significant discrepancies in the upper flame, where the premixing and highly unsteady extinction and re-ignition effects are important. These are expected to be difficult to predict using the non-premixed flamelet model.

Luo et al. [386] evaluated the performance of the FPV approach in predicting NO formation in a pulverized coal flame based on a 2D laminar counterflow flame. In the first step, only the thermal NO_x was considered, while the fuel nitrogen was neglected, and the chemistry was described using GRI-Mech 3.0 for the assumed light gases in the volatile matter. Recently, the researchers further extended the flamelet model in the context of LES to simulate a laboratory-scale pulverized coal jet flame, in which the fuel NO_x, prompt NO_x and thermal NO_x were considered [387]. In this work, the NO_x formation mechanisms were not directly taken from the flamelet library described with the detailed chemistry mechanism, but were described with a separate mechanism specifically for different formation paths. Akaotsu et al. [388] evaluated the performance of the FPV approach in reproducing the thermo-chemical quantities in the pulverized coal flame stabilized in a laminar counterflow configuration. The computational setup is the same as that adopted by Wen et al. [383]. The suitability of the flamelet model was evaluated by comparing it with the detailed chemistry solutions.

While the works above used non-premixed flamelet approaches, Knappstein et al. [389–392] extended a premixed flamelet model based on flamelet-generated manifolds (FGMs) [393] for coal combustion. The thermo-chemical quantities in the FGM table were parameterized as a function of the mixture fraction, a reaction progress variable and the

total enthalpy. The validity of the proposed FGM model was first evaluated in an electrically heated inert pyrolysis reactor and a premixed flat flame configuration, focusing on the ignition process of the single coal particle. Overall, good agreement was obtained between the numerical results and experimental findings [389]. The same FGM model was further evaluated in [390] by simulating a single coal particle, exposed to hot product gases. The assumptions of the premixed combustion mode and the species compositions in volatile matter were evaluated. In order to describe both the devolatilization and char surface reactions, Knappstein et al. [392] further extended the FGM model to include a four-dimensional manifold controlled by two mixture fractions for volatiles and char off-gases, the enthalpy and a reaction progress variable. The suitability of the extended FGM model was evaluated by comparing it against the detailed chemistry solutions, and good agreement was obtained with respect to the major species and gas temperature, while the intermediate species of OH and CO have deviations in certain regions. Similarly to the work of Knappstein et al. [390], Wan et al. [32] developed a premixed-flame-based flamelet model for predicting alkali metal emissions from a pulverized coal flame stabilized in a turbulent mixing layer. They evaluated the developed flamelet model's suitability for predicting sodium emissions by comparing it with the DNS data. Recently, Nicolai et al. [394] conducted the LES of a laboratory-scale gas-assisted pulverized coal combustion chamber in an oxy-fuel atmosphere using the FGM model, coupled with the artificially thickened flame (ATF) model to resolve the premixed flame structure in the LES mesh. The simulation results were compared to the available experimental data, including the velocity fields and the flame positions. Further, the ignition and coal particle group combustion were studied by Nicolai et al. [395] in a laminar flow reaction using the flamelet tabulation method. Two mixture fractions are introduced to describe the mixing among the fuel gases from the volatile matter, the methane for coal flame stabilization, and the oxidizer stream. The influences of particle groups on the ignition and combustion characteristics were investigated by successively increasing the densities of particle streams. The predicted ignition delay was compared to the available experimental data, and overall good agreement was achieved.

6.4. Turbulence-chemistry interaction for pollutant formation

The modeling of turbulence-chemistry interaction is expected to have a significant effect on the prediction of pollutant formation since the chemical timescales of pollutants can range from very small (on the order of the main chemical reactions) to large (slow processes such as for thermal NO). In recent years, a number of CFD simulations have been conducted to predict pollutant formation in pulverized coal flames. Unlike pure gas combustion, the fuel-bound nitrogen and sulfur in volatile matter and char should be considered in the numerical models. This subsection reviews CFD simulations focusing on the prediction of pollutant formation in pulverized coal flames, first with the simple TCI models followed by the advanced TCI models discussed above.

6.4.1. NO$_x$ formation

Kurose et al. [396] conducted a 3D numerical simulation of an advanced low-NO$_x$ burner based on the simplified coal combustion models in the framework of RANS. The NO$_x$ formation model was employed for post-processing, i.e., the NO$_x$ concentrations were calculated based on the distributions of the gas temperature and the concentrations of the major chemical species. Thermal NO was obtained with the extended Zeldovich mechanism based on the quasi-steady-state approximation for nitrogen species. Prompt and fuel NO were predicted using the models developed by De Soete [397]. Particularly, the reduction in NO due to char burning was considered in their simulations using Levy et al.'s [398] model, while the formation of char NO was also calculated using De Soete's model [397]. Based on the same NO$_x$ formation mechanisms as in the work of Kurose et al. [396], Muto et al. [399] went on to conduct a large-eddy simulation (LES) of a

laboratory-scale pulverized coal burner to investigate the effect of oxygen concentration on NO$_x$ formation in the oxy-fuel atmosphere. Hashimoto et al. [400] investigated the effects of fuel-NO formation models on the prediction of NO concentrations in a coal combustion model. A 760 kW test furnace was simulated with the RANS technique, coupled with the modified TDP model [401] for devolatilization and the Field model [402] for char combustion. While the mechanisms leading to the formation of the thermal, prompt and fuel NO originating from char are the same as those in refs. [396] and [399], three different fuel-NO models, i.e., De Soete [397], Chen et al. [403] and Mitchell et al. [166], were evaluated for NO originating from the volatile matter. Hashimoto et al. [400] found that the model proposed by Mitchell et al. could reproduce the tendency of the measurement results better than the models proposed by De Soete and Chen et al. Recently, Muto et al. [404] conducted a LES of pulverized coal combustion in a multi-burner system with three advanced low-NO$_x$ burners to investigate the effect of in-furnace blending method on NO emission. The NO$_x$ formation models and coal combustion submodels adopted, including the devolatilization model, the char surface reaction model, and the gas combustion model, are the same as those in their previous works [399,400]. Note that in all the above works [396,400,404,405], the NO prediction was conducted in post-processing, i.e., the NO production rate was calculated based on the major species mass fractions, which were obtained with the gas combustion models. The gas combustion model named SSFRRM (Scale Similarity Filtered Reaction Rate Model [362]) was adopted, with global or two-step reaction mechanisms. This cannot, however, consider finite-rate chemistry, which is important for NO formation.

In recent years, researchers have extended the advanced TCI gas phase combustion models to simulate NO$_x$ formation in pulverized coal flames. Luo et al. [386] first evaluated the flamelet model's ability to predict NO formation in a fuel-nitrogen-free pulverized coal flame by means of *a priori* analysis. To take into account the slow chemistry process of thermal NO, the trajectory variable of the reaction progress variable was redefined by including the NO mass fraction. The sensitivity of the reaction progress variable definition was studied by varying the amount of NO in the reaction progress variable. The results showed that the NO mass fraction in the fuel-nitrogen-free flame can be predicted well by the flamelet model with a redefined reaction progress variable. This finding applies to pulverized coal flames operated in different conditions, including different strain rates and initial gas temperatures. Recently, Zhao et al. [387] further extended the work by Luo et al. [386] to include LES, taking into account all three NO formation mechanisms. Unlike the work by Wen et al. [381], the NO mass fraction was not determined from the flamelet library, but from the corresponding sub-mechanisms for NO emission by assuming that NO did not have any significant effect on the reactions of the other major species. The model parameters for the kinetics of the NO formation were determined from the semi-empirical relations. This model was evaluated by simulating a laboratory-scale pulverized coal jet flame, and the
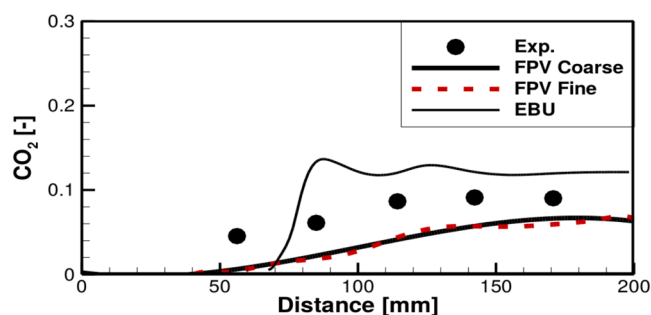

Fig. 25. CO$_2$ fraction comparison along the centreline. The simulation data for the flamelet approach (coarse and fine) and the EBU model refer to the gas phase, and the measurements relied on a gas sampling method. Reprinted with permission from [377]. Copyright 2017 Taylor & Francis Group.
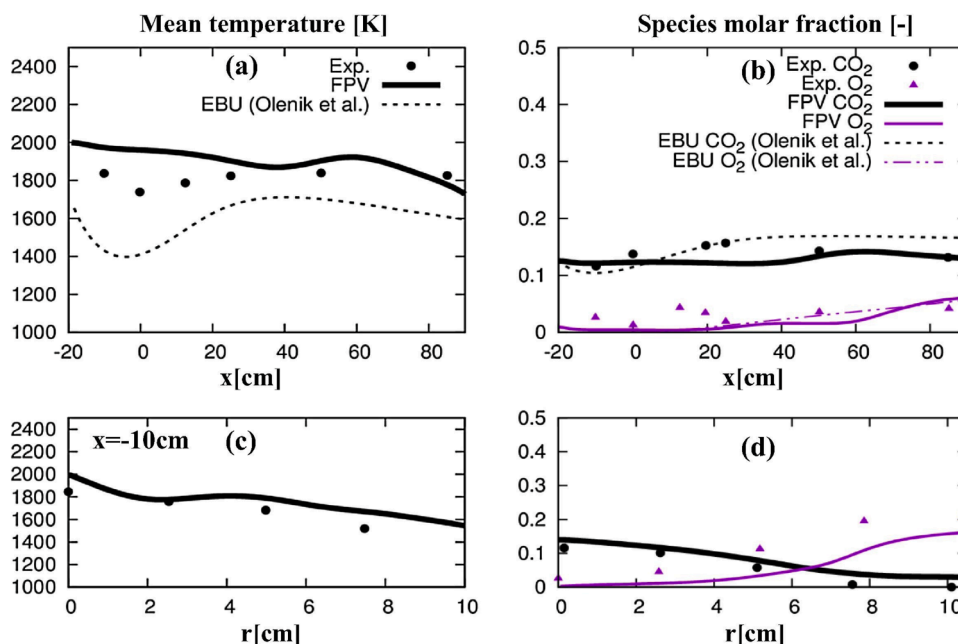
Fig. 26. Comparison of mean temperature (left) and species molar fraction (right): (a and b) along central axis, (c and d) x = −10 cm. The flamelet results are from [376], the EBU data is taken from [15]. Reprinted with permission from [376]. Copyright 2016 Elsevier Ltd.
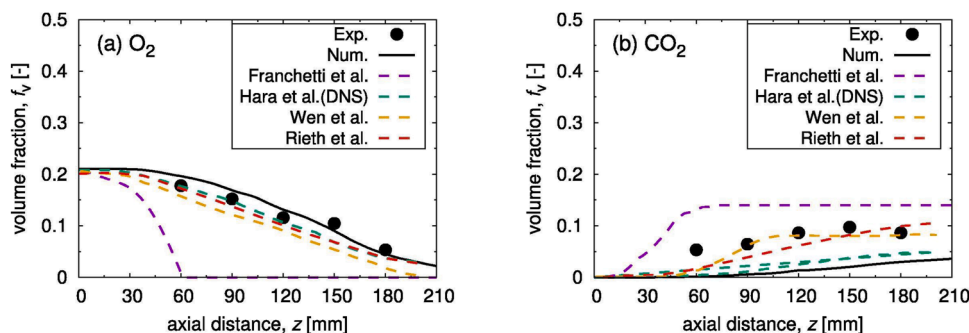

Fig. 27. Axial distributions of the measured [407] and calculated volume fractions of O_2 and CO_2. For validation, the numerical solutions in previous studies [18,19, 339,378] are also shown. Reprinted with permission from [409]. Copyright 2020 Elsevier B.V

flamelet predictions were compared to the experimental data. It was found that including fuel nitrogen can improve the prediction accuracy, indicating the importance of fuel nitrogen in NO formation. Wen et al. [381] evaluated different flamelet tabulation methods for predicting NO formation in fuel-nitrogen pulverized coal flames, in which all fuel NO, prompt NO and thermal NO were considered. The NO mass fraction was obtained either by taking it directly from the flamelet library or by solving the corresponding transport equation with the reaction source terms extracted from the flamelet library. The flamelet predictions were compared to the detailed chemistry solutions. The results showed that the NO mass fraction extracted from the flamelet library agrees well with the reference result of the detailed chemistry solution, and is comparable to the solution obtained from the transport equation. This finding is different from that obtained from the fuel-nitrogen-free pulverized coal flame. The reason for this is considered to be that fuel NO, with a fast chemistry, is dominant in the fuel-nitrogen pulverized coal flame in contrast to thermal NO, which has a slow chemistry. Recently, Wen et al. [406] investigated the NO_x formation mechanism in a turbulent pulverized coal flame with fuel-bound nitrogen stabilized in a mixing layer by carrying out detailed analyses of a DNS dataset, including the reaction path analysis, chemical timescale analysis, *a priori*

analysis and budget analysis. The reaction path analyses revealed that the principal thermal-NO reaction contributes to the net consumption of NO in fuel-nitrogen pulverized coal flames. The chemical timescale analysis showed that the production rate of NO species is faster than those of major species, which confirms the suitability of the flamelet tables generated based on the steady flamelet equations. The *a priori* analysis indicates that the gas temperature and major/intermediate species can be predicted well by the flamelet model, while the NO_x species show significant discrepancies in certain regions. The budget analyses of the generalized flamelet equations offered evidence that the discrepancies for NO_x species are due to multi-dimensional diffusion being neglected in the 1D flamelet model employed.

6.4.2. SO_x formation

Unlike studies on NO formation in pulverized coal flames, studies on SO_x formation using the advanced TCI model are rare. Wen et al. [382] first extended the flamelet model to predict SO_x formation in a fuel-sulfur pulverized coal flame stabilized in a 2D counterflow configuration. As was the case for NO prediction in [381], the SO_x species were either extracted from the flamelet library or by solving the corresponding transport equations with the reaction source terms taken from
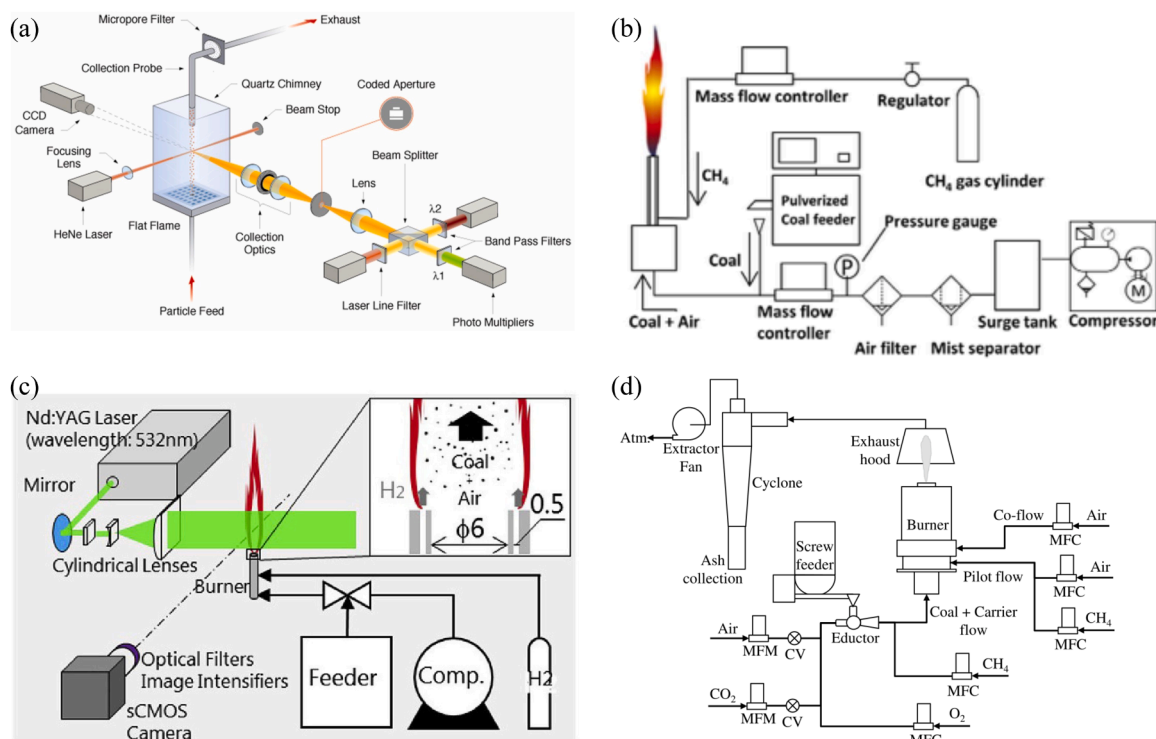
Fig. 28. Schematic of laboratory-scale pulverized coal flames. (a) Sandia single coal particle injection flame by Molina and Shaddix [411,412]; (b) CRIEPI piloted pulverized coal jet flame by Hwang et al. [407]; (c) CRIEPI piloted pulverized coal jet flame by Zhang et al. [413] and Ahn et al. [414]; and (d) Cambridge piloted swirl-stabilized pulverized coal flame by Balusamy et al. [415,416]. Reprinted with permission from Elsevier, American Chemical Society and Springer Nature, Copyright (2007, 2005, 2019 and 2015).

the flamelet library. The different methods' performance in predicting SO_x species was evaluated by comparing them against the corresponding values of the detailed chemistry solutions. The results showed that the SO_x species can be accurately predicted in most regions of the computational domain, while non-negligible discrepancies can be obtained in certain regions where the premixed combustion mode is dominant. The chemical timescale analysis indicates that in the fuel-bound sulfur flame studied, the production rates of the SO_x species can be faster than/-comparable to those of the major species, which supports the suitability of the flamelet model based on the steady flamelet equations. This also explains why the SO_x species extracted from the flamelet library agree with those obtained from the transport equations with the reaction source terms extracted from the flamelet library, and the detailed chemistry solutions.

Based on the previous works on NO and SO_x formations in laminar counterflow flames, Wen et al. [384] recently conducted LES for laboratory-scale swirl-stabilized multi-stream pulverized coal flames using the flamelet model, in which both NO and SO_x emissions were considered. They further investigated how the oxidizer atmosphere, including air and oxy-fuel, affected pollutant formation. This work is the state-of-the-art in flamelet modeling of pollutant formation in pulverized coal flames. The flamelet predictions were compared to the available experimental data, including the flame structure and the particle temperature. In the simulation, volatile N, char N and volatile S were considered, and the chemistry was described with a newly developed oxy-fuel mechanism containing 129 species and 911 elementary reactions. The results showed that in the oxy-fuel atmosphere, NO is mainly formed in the upstream region, while in the air atmosphere, a large amount of NO is formed in the far-downstream region, which is taken into account due to the existence of thermal NO. For both air and oxy-fuel atmospheres, the distributions of SO, SO_2 and SO_3 are similar overall, with SO and SO_2 mainly in the upstream region and SO_3 in the downstream region, although the amounts of SO_x formed in different

atmospheres are quantitatively different.

6.5. Selected comparisons of TCI models and their application in CFD

In the following, selected examples from the literature are presented where the applications of the different TCI models in CFD are compared.

Wen et al. [377] compared the performance of the flamelet model with the EBU model on a piloted pulverized coal jet flame [407]. Their focus was on investigating whether the thermo-chemical quantities in a pulverized coal flame can be predicted better with a finite-rate chemistry model (flamelet) compared to the infinitely fast chemistry model (EBU) [341]. They found that the prediction accuracy of the species mass fractions can be significantly improved when using a flamelet model, as illustrated in Fig. 25. In a latter paper from the same group [376], they confirmed this trend by simulating the large-scale IFRF (International Flame Research Foundation) furnace No. 1 [408] using a so-called three-stream flamelet model. The comparisons between the flamelet model and the EBU model are shown in Fig. 26. It can be observed that for both the temperature and the species, the proposed flamelet model performs better than the EBU model [15].

Recently, Akaotsu et al. [409] compared the simulation results for the CRIEPI jet flame [407] from different groups using different combustion models, including different flamelet models, EBU and reference DNS data. As shown in Fig. 27, it was found that, with the exception of the infinitely fast chemistry EBU model, which has larger discrepancies, all flamelet models perform well and are comparable to the DNS in predicting species volume fractions, although different numerical setups are used in the different groups. Despite the good agreement, we note that the results from different flamelet models might not be directly comparable, since all groups use different platforms for their simulations. Smaller differences in the prediction accuracy should not be attributed purely to the formulation of the flamelet model.

7. Reference burners for pulverized coal combustion and gasification

A crucial point for the development and validation of high-fidelity models is the availability of experimental reference data. This section reviews experimental reference burners for combustion and gasification. The systems range from single-particle laboratory-scale combustors (Section 7.1) to medium-/large-scale combustors (Section 7.2) and industrial-scale furnaces (Section 7.3). Gasification reactors are then discussed in Section 7.4. The systems discussed were selected as they have been used extensively for model validation; most of them are so-called target systems in the CBC (Coal and Biomass Combustion) workshop [410]. In general, only the most recent studies are discussed, since they usually provide the latest data, which is particularly interesting for model validation. References to earlier experimental investigations can be found in the bibliographies of the cited studies.

7.1. Laboratory-scale burners for combustion

To date, several laboratory-scale burners have been studied both experimentally and numerically. A series of experimental works have been conducted by Molina and Shaddix [411,412] to study single coal particle ignition in both air and oxy-fuel atmospheres under various operating conditions. The experimental setup is shown in Fig. 28(a). The experiments were conducted in the laminar, optical entrained-flow reactor operated at 1 atm and used a non-premixed-flamelet Hencken burner to provide combustion product gases. Coal particles were injected at the furnace centerline at different feeding rates to initiate the ignition of single particles or particle clusters. The single-particle experiments have been investigated by four research groups: TU Freiberg/TU Darmstadt [41,371], University of Stuttgart [309,351], Sydney University [417] and the University of Utah [300]. Vascellari et al. [41, 371] studied the ignition of the single coal particle by conducting a resolved particle simulation, in which the transient boundary conditions were directly taken from an Eulerian-Lagrangian simulation *a priori*. The results obtained with the resolved particle simulation were used to evaluate the performance of the unsteady flamelet model. Tufano et al. [309,351] particularly focused on implementing the Robin boundary condition on the particle surface, which accounts for both convective and diffusive phenomena during devolatilization. The influences of kinetic mechanisms, transport properties and particle boundary conditions on the particle ignition process were investigated. In the above studies, the single first-order reaction devolatilization model was used to describe the devolatilization rate. Cleary et al. [417] adopted a new approach to describe the processes of evaporation, devolatilization and char conversion. This approach is based on the conservation equations for passive scalar variables, and is derived from the analytical solution of the mixture fraction and standard enthalpy transport equations in the particle boundary layer. Goshayeshi and Sutherland [300] adopted advanced submodels to describe the devolatilization process based on one-dimensional balance equations in the direction transversal to the jet flow. The evaluated devolatilization model includes the two-step competing model [65] and the network-based CPD model [50], while the evaluated gas combustion model includes the detailed chemistry based on GRI-Mech 3.0 [418] and the infinitely fast chemistry flame-sheet approach. With a similar experimental setup as in ref. [411, 412], Schiemann et al. [419] conducted experiments using coal particles with size fractions relevant for pulverized coal combustion. The influence of atmospheres on particle ignition, char burning and alkali release were investigated for different coal types. For single particle and group coal particle combustion, TU Darmstadt conducted a series of experimental works based on a fully premixed flat flame burner with well-defined boundary conditions. Well-documented experimental data has been achieved for this burner, which is valuable for the purpose of model evaluation, and it will be the target flame in the CBC workshop. Köser et al. [420,421] employed non-intrusive simultaneous

multi-parameter techniques to study the volatile combustion of single coal particles. High-speed luminescence imaging combined with high-resolution high-speed OH-PLIF was employed to visualize the flame. A stereoscopic high-resolution backlight-illumination system was set up to measure the particle size. Knappstein et al. [389] applied a flamelet model coupled with a one-step devolatilization model to simulate the flame. They found that this modeling approach can offer reasonable predictions of the ignition height and the overall flame shape. For particle group combustion, Liu et al. [422] conducted experiments to study the effect of particle number density (PND) on the ignition delay time. They found that it decreases as the coal particle feeding rate increases, until a minimum value is reached, corresponding to a particle number density of around $4 \times 10^9 \, \text{m}^{-3}$. At an even higher coal feeding rate, the ignition delay increases again. Nicolai et al. [395] numerically investigated pulverized coal particle group combustion with a flamelet model. They obtained similar findings as in the experiment [423], namely that the ignition delay time is increased significantly at higher particle densities. Further, it was found that the shape of the volatile flame is strongly influenced by the particle number density. A transition from spherical flames around single particles to a conical flame around the particle cloud was found in both the numerical simulations and experiments. It is important to note that the above works focus mainly on homogeneous ignition in the gas phase. There are comparatively few studies on heterogeneous ignition and the potential competition between the two ignition modes (i.e. heterogeneous and homogeneous). Heterogeneous ignition in particular is discussed in [424–426].

Hwang et al. [407] at the Central Research Institute of Electric Power Industry (CRIEPI) experimentally studied a laboratory-scale piloted pulverized coal jet flame. The measured data included the particle velocities, particle temperature, species concentrations of O_2, N_2, CO_2, CO and NO, and 2D and radial distributions of Mie scattering and OH-LIF. Due to the well-documented experimental data, a substantial number of groups have simulated this configuration using different numerical models; some of the results are summarized below. Stein et al. [343] compared the simulation results from three different research groups: TU Freiberg/TU Darmstadt, University of Stuttgart and University of Duisburg-Essen/Imperial College London. In these different simulations, the devolatilization was described by one- or two-step kinetics, while turbulence-chemistry interaction was modeled by EBU fast chemistry approaches. Franchetti et al. [339] at Imperial College London conducted an additional LES of the CRIEPI burner using the same coal submodels, but with a Lagrangian method to track the coal particles, which is different from the approach taken in [343]. Wen et al. [341, 377,378,380] independently performed several simulations for the CRIEPI flame using different gas combustion models in the context of LES and DNS. The devolatilization and char surface reaction are the same in these simulations, and correspond to the Badzioch and Hawksley model [63], Baum and Street model [368] and P1 model [16], respectively. At first, to simulate the CRIEPI flame, Wen et al. [341] adopted a simplified EBU model in which the sub-grid scale fluctuations on the particles were considered. To overcome the disadvantage of the infinitely fast chemistry EBU model, a finite-rate chemistry flamelet model was developed to simulate the CRIEPI burner in [377]. Wen et al. [380] developed a three-mixture-fraction (pilot CH_4, volatiles and char off-gases) flamelet model to adapt to the multi-fuel streams in the CRIEPI flame. Rieth et al. [18] conducted a LES using the CPD model, while Zhao and Haworth [12] performed RANS simulations adopting a transported PDF technique with standard simplified coal combustion submodels. Cai et al. [358] conducted a LES using an Eulerian–Eulerian multi-fluid method, in which the EDC model was used to describe the reaction rate; the two-competing-reaction-rate model was used for devolatilization, and char surface reactions were modeled in line with Hamor et al. [156]. Hashimoto et al. [318] conducted a RANS for the CRIEPI flame using different devolatilization models. The performance of the newly proposed tabulated-devolatilization-process model (TDP
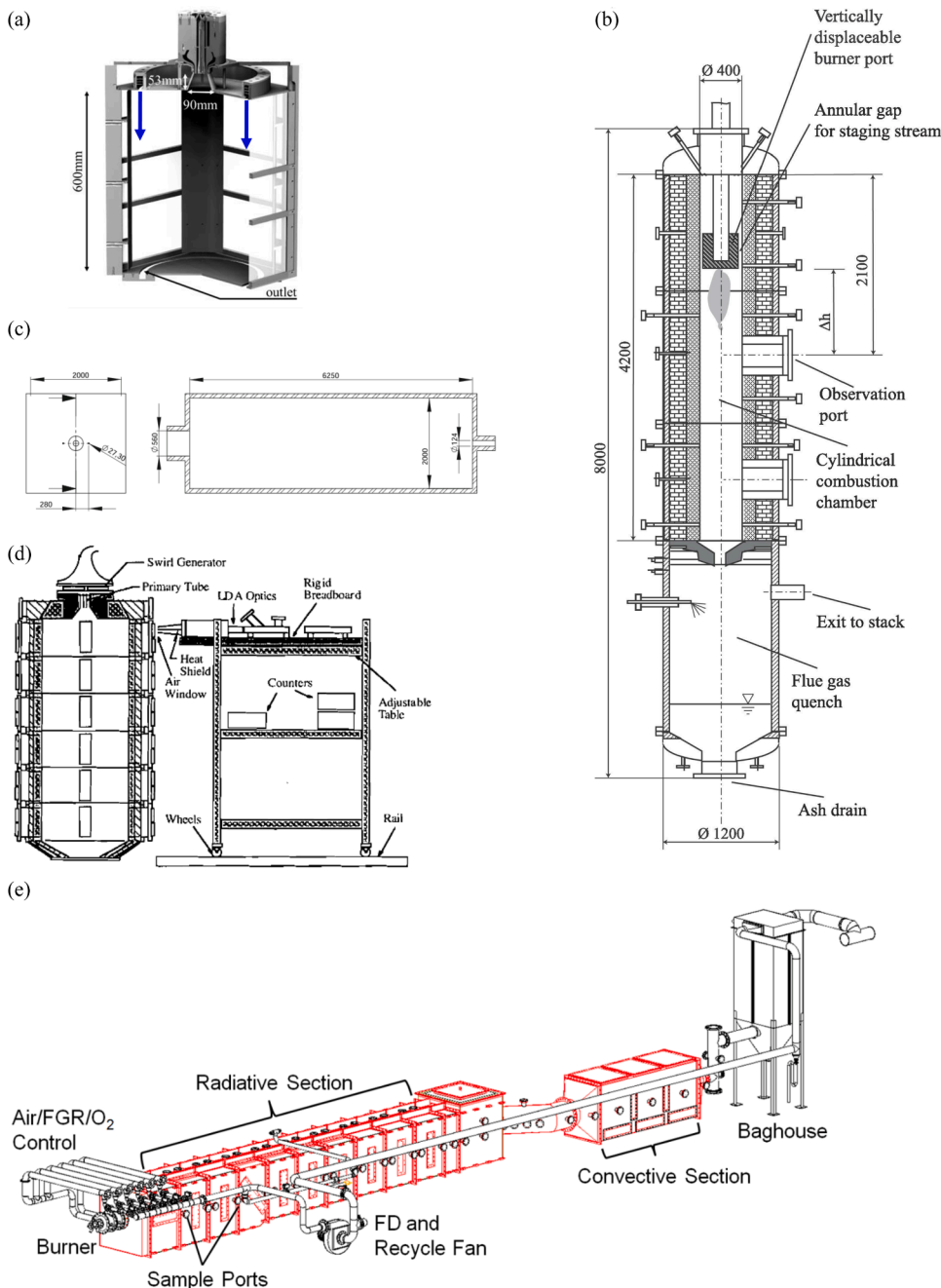
(a)

(c)

(d)

(b)

(e)

model, see Section 5.3) was compared to the widely used conventional devolatilization models including the Badzioch and Hawksley [63] and the Kobayashi models [65]. The char burning rate was calculated using the Field model [402]. Ahn et al. [357] conducted a LES for the CRIEPI flame using a simple gas combustion model based on two-step global kinetic mechanism. Again, the Badzioch and Hawksley [63] and the Kobayashi [65] models were used. Zhao et al. [330] adopted a two-phase MMC-LES model to simulate the target flame following both the Badzioch and Hawksley [63] and the Kobayashi models [65]. Wan et al. [359] conducted a LES of the CRIEPI burner using CPD, the PaSR model to describe the chemical reaction rate, and the kinetic/diffusion surface reaction model to characterize the char surface reaction rate. Recently, Hara et al. [19] conducted a DNS using a global volatile matter reaction scheme to describe the devolatilization rate, which is calculated based on the detailed reaction mechanism. Zhao et al. [387] conducted a LES using a flamelet model for gas combustion and the conventional coal

submodels for the devolatilization and char surface reactions. The focus of that work was on investigating the NO formation characteristics taking into account the three NO formation mechanisms.

For the same CRIEPI burner, additional experimental data was gathered for the same operating conditions. Hayashi et al. [427] measured the spatial distributions of the soot volume fraction and pulverized coal particles using laser-induced incandescence (LII) and Mie scattering imaging, respectively. The radial distributions of the soot volume fraction were compared with the OH radical planar laser induced fluorescence (OH-PLIF) signal intensity obtained from the experiment by Hwang et al. [407]. Xu et al. [428] and Takahashi et al. [322] conducted numerical simulations to predict soot formation in the CRIEPI burner and compared their findings against the experimental data. The simulation conducted by Xu et al. [428] was based on RANS coupled with the EDC model, while Takahashi et al. [322] used LES coupled with the SSFRRM model [362]. In both simulations, advanced

devolatilization models were used, i.e., the CPD model was used in [428] while the TDP model was employed in [322]. In both simulations, the coal-derived soot formation model proposed by Brown and Fletcher [429] was employed to calculate the soot number density.

Recently, Zhang et al. [413] and Ahn et al. [414] conducted new experiments for the CRIEPI burner, focusing on the non-reacting flow and reaction flow, respectively. In contrast with the operating conditions studied by Hwang et al. [407] and Hayashi et al. [427], where the pilot fuel is CH_4, in the new experiments the pilot fuel is H_2, while the other operating conditions are the same, as shown in Fig. 28(c). The gas temperature was measured using a sheathed thermocouple, while the gas composition was examined using a gas analyzer with a sampling probe. The particle dispersion characteristics and velocity were measured by Mie scattering and PIV techniques, using an optical measurement system. Zhang et al. [413] conducted a LES to analyze the particle dispersion. To investigate the effect of particle shape, spherical and spheroidal motion models were incorporated to characterize the particle's movement. Ahn et al. [414] conducted a LES for the piloted pulverized coal flame using the simplified coal combustion submodels. Particularly, the predicted gas temperature and major species concentrations were compared to the experimental data, while NO_x formation in the pulverized coal flame was analyzed in detail.

The laboratory-scale Cambridge flame was studied experimentally by Balusamy et al. [415,416], as shown in Fig. 28(d). Two experiments have been studied, with and without a central stabilizing bluff body. The available experimental data for this flame include the particle velocity and the simultaneous Mie scatter and OH-PLIF [415,416]. Muto et al. [399] conducted a LES for the Cambridge flame without the central bluff body, studying the effect of the oxygen concentration on NO_x formation in the oxy-fuel atmosphere. The simplified coal combustion submodel was employed, coupled with the SSFRRM gas combustion model, while all three NO_x formation mechanisms, including thermal NO_x, prompt NO_x and fuel NO_x, were considered in the simulations. Recently, Chen et al. [430] conducted a LES using an extended FPV approach in an Euler-Lagrange framework. A single-kinetic-rate model was applied for devolatilization, and char surface reactions were neglected since they only had a negligible effect in the near-burner zone. Reasonable agreement was achieved between the flamelet predictions and the experimental data. Further analysis reveals that different combustion modes exist in the Cambridge flame, with a typical premixed flame in the region furthest upstream, a double flame in the middle stream and a typical non-premixed flame in the downstream region.

7.2. Medium- to large-scale combustors

In this section, medium- to large-scale pulverized coal flames are reviewed. Their combustion characteristics are expected to be closer to the industrial applications.

Fig. 29 (a) and (b) depict schematics of the Darmstadt and Aachen swirl-stabilized pulverized coal burners which were experimentally studied by Toporov et al. [302] and Becker et al. [385]. Both target flames are generated by similar swirl burners mounted in combustion chambers with similar characteristics, and can be stabilized under a wide range of operating conditions. These burners are designed particularly for pulverized coal combustion in oxy-fuel atmospheres. While the Aachen burner enables the aerodynamic stabilization of a pulverized coal flame, the Darmstadt flame is gas-assisted. The Darmstadt burner is derived from the Aachen burner, and is generated by a burner optimized for simulations and experiments in well-controlled boundary conditions. The Aachen burner is composed of two annular concentric nozzles, with the central annular nozzle providing a mixture of solid fuel and oxidizer, and the adjacent annular orifice providing a swirled oxidizer stream. Three different operating conditions have been studied experimentally: one reference case with conventional air firing and two cases using oxy-fuel, respectively. A comprehensive experimental data set has been generated, including gas velocities, species concentrations of CO_2, CO,

H_2O and light hydrocarbons as well as the internal wall temperature. The Darmstadt burner provides excellent optical access to the flame. Since the internal chamber walls and the burner quarl are made of quartz glass, optical flame diagnostic techniques can be applied. At present, three operating conditions have been investigated, including a reference air case and two oxy-fuel cases. The initially available experimental data included the OH-PLIF and particle velocities. Becker et al. [435] recently investigated the particle dynamics in the Darmstadt burner using advanced laser diagnostics. The small and large coal particle velocities were measured using two-phase particle image velocimetry and particle tracking velocimetry (PIV/PTV), respectively, and the spatial distributions of pyrolysis products were recorded via laser-induced fluorescence (LIF). The results showed that the coal type has only a minor effect on the gas phase velocities, and the profiles of the mean axial velocity of the large particles have flatter gradients than those of the gas phase velocity. Sadiki et al. [436] conducted both LES and RANS simulations for the Aachen burner to analyze the effects of turbulence and multiphase treatments on the oxy-coal combustion process using simplified coal combustion submodels coupled with the EDC gas combustion model. For the Darmstadt burner, Doost et al. [437] conducted a LES for the Darmstadt burner to study the fluid residence times in the non-reacting case, and the predicted gas velocities were compared to the experimental data. Knappstein et al. [391] conducted a LES for the Darmstadt burner for the reacting cases using a flamelet-based model coupled with the simplified devolatilization and char surface reaction models. In the first step, only the air cases were studied, and the predicted results, including the gas velocities and the OH-PLIF, were compared to the experimental data. Nicolai et al. [394] conducted a LES of the Darmstadt burner operated under an oxy-fuel atmosphere, using the premixed flamelet model coupled with an artificially thickened model (ATF). The simulation results were compared to the experimental data, including axial and tangential velocities, and very good agreements were achieved. Recently, Wen et al. [384] conducted a LES of the Darmstadt burner operated in different conditions using a multi-stream flamelet model. That work focuses on investigating the influence of the atmosphere on pollutant formation. The simulation results were compared to the available experimental data, including the globally observed flame structure and the particle temperature, and reasonable agreement was obtained. It is important to mention that all of the above described simulations for the Darmstadt burner focused particularly on the turbulent gas phase combustion part and TCI. Thus, they employed conventional models for the solid phase, i.e., single-kinetic rates for devolatilization and a diffusion-kinetic-controlled model for char oxidation.

For the Aachen burner, Massmeyer et al. [438] carried out an experimental study examining how the fuel type and oxidizer composition influence the flame structure and combustion behavior. Four pulverized coal flames with different coal types and different atmospheres were studied with a constant thermal output and stoichiometry. A combination of flame-intrusive and non-intrusive measurement techniques was employed to provide detailed in-flame measurements, including the flow field, major product species and radiative heat transfer. The main findings of the experiment are that the flame length is predominately controlled by the effective swirl intensity, and the location of the peak combustion intensity is determined by the flow inlet conditions at the burner. Nicolai et al. [22,385] employed a LES coupled with the premixed flamelet model for the air and oxy-fuel atmospheres using the same coal combustion submodels as in their previous work [394] to simulate the Darmstadt burner. The simulation results were compared to the available experimental data for both air and oxy-fuel atmospheres, including the velocities, the particle temperature and major species mass fractions in the near-burner region. Reasonable agreement was achieved between numerical and experimental data for both atmospheres. Further, the influence of the different atmospheres on the interaction of coal particles and the gas phase was investigated.

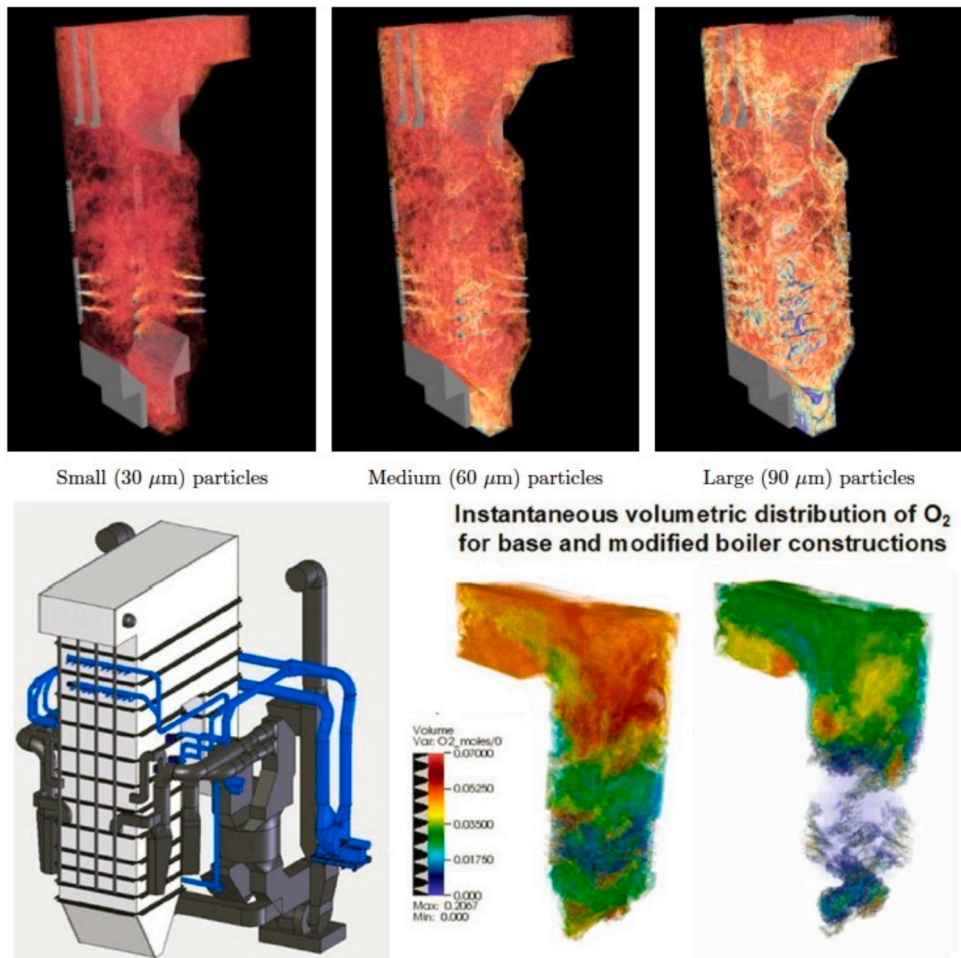Another important reference configuration is the IFRF (International

Small (30 μm) particles   Medium (60 μm) particles   Large (90 μm) particles

Fig. 30. LES of the Alstom industrial-scale furnaces operated at 15 MW (top) [451] and 342 MW (bottom) [452]. Bottom figure: reprinted with permission from Elsevier, Copyright (2018).
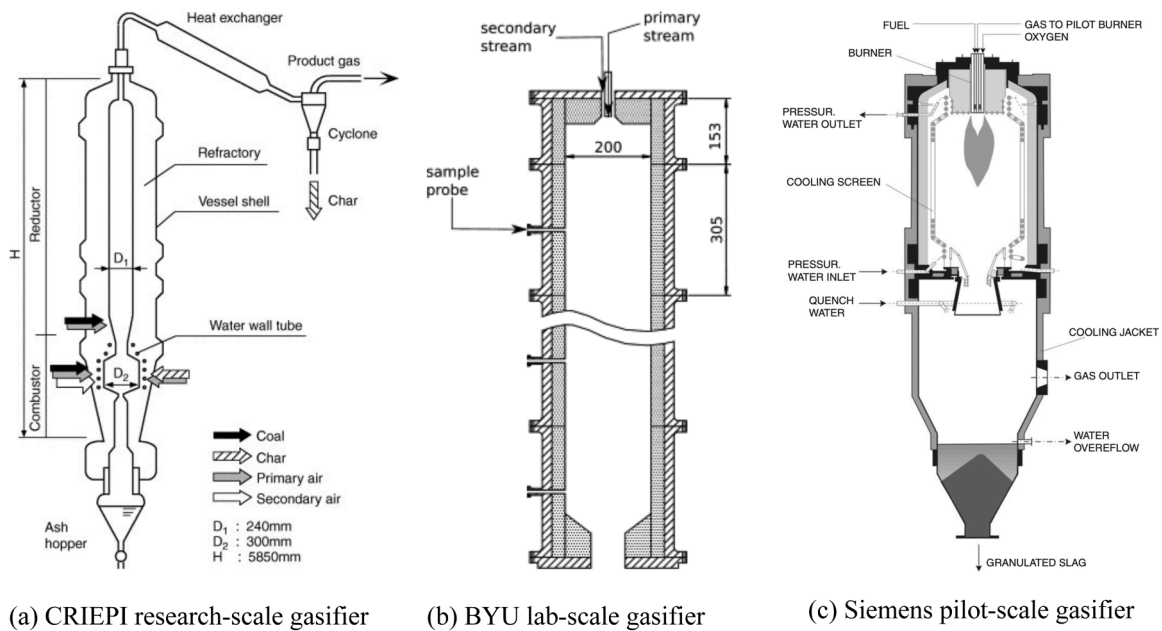

(a) CRIEPI research-scale gasifier   (b) BYU lab-scale gasifier   (c) Siemens pilot-scale gasifier

Fig. 31. Schematic of the gasifiers on different scales. (a) CRIEPI 2 tons/day (T/D) research-scale coal gasifier [455]; (b) Brigham Young University (BYU) experimental-scale entrained-flow gasifier [327,332]; (c) Siemens 5 MW pilot-scale gasifier [457,458]. Reprinted with permission from Elsevier and Taylor & Francis Ltd., Copyright (2006, 2014 and 2008).

Flame Research Foundation) No. 1 furnace, sketched in Fig. 29 (c). This includes both the long flame configuration [432] and the swirl-stabilized configuration [408]. The furnace has a 2×2 m^2 rectangular cross section and is about 6 m long. It can generate 2–3 MW of thermal power and has similar combustion characteristics to industrial furnaces where the radiative heat transfer is dominant compared to the convective heat transfer. For both configurations, the available experimental data include the radial and axial profiles of the mean gas velocity, mean temperature and mean species concentrations in the near-quarl region. For the long flame configuration, Stöllinger et al. [21] conducted a RANS simulation using an extended transported PDF model, coupled with simplified coal combustion submodels. For the swirl-stabilized configuration, Weber et al. [439] conducted a RANS simulation using simplified coal combustion submodels coupled with the EBU model. One limitation of the RANS approach is that the vortex breakdown in the recirculation zone cannot be predicted. Thus, Olenik et al. [15] conducted an initial LES of the IFRF No. 1 furnace using the EBU model coupled with simplified coal combustion submodels. To overcome the limitations of the EBU model, Wen et al. [376] extended a three-stream FPV model for LES to simulate the furnace with standard conventional coal combustion submodels. The simulation results obtained by Wen et al. [376] were compared to those obtained by Olenik et al. [15]. The flamelet model was found to outperform the EBU model in predicting the gas temperature and species concentrations. Rieth et al. [17,440] also conducted two LESs for the IFRF No. 1 furnace using a two-mixture-fraction flamelet model coupled with simplified coal combustion submodels. In contrast to previous works [15,376], a significantly finer mesh was used. Overall, these LES studies offered satisfactory agreement with the experimental results and demonstrated that LES could be used to compute large-scale pulverized coal flames.

Pickett et al. [433] conducted experiments at Brigham Young University (BYU) with a practical pulverized coal reactor, shown schematically in Fig. 29 (d), to investigate the effects of swirl level, velocity profile and mass flow rates on NO formation. The available experimental data includes the axial and tangential gas velocities, gas temperature and NO$_x$ species concentrations. Xu et al. [441] conducted a RANS simulation of the BYU swirl-stabilized flame to predict NO destruction due to advanced reburning. A four-step, eight-species reduced mechanism was integrated into their comprehensive CFD code PCGC-3 [442]. The integrated model for advanced reburning was evaluated by comparing the findings against experimental data on the NO concentrations and gas temperature. It was found that most of the NO reduction is caused by chemical reactions, while only a small part of the NO reduction is due to the dilution of the strong swirling flow. The PCGC code developed at BYU used basic approaches for modeling gas phase combustion, such as the fast-chemistry or chemical equilibrium assumption, combined with a mixture fraction-based and presumed PDF approach [443]. Solid fuel kinetics were initially modeled using simplified empirical approaches, such as the two-step pyrolysis model [65] and the single-film char model. The CPD and the FG-DVC models were later coupled in more recent versions of the PCGC code [11,327]. The PCGC code was also used to investigate coal gasification [327].

The 1.5 MW pilot-scale combustor (L1500) at the University of Utah [434] is a horizontally fired test furnace that is designed to simulate pulverized coal combustion with low NO$_x$ emissions. The test rig has a 1 m^2 cross-section and a total length of 12 m, which is divided into 10 sections with various sampling and injection ports. As shown in Fig. 29 (e), the L1500 combustor is equipped with stainless steel flue gas recycle lines, in-line fans and an associated control system to allow the recycling of the flue gas, which facilitates oxy-fuel combustion experiments. The test rig has four oxidizer streams. The primary stream entrains the pulverized coal into the variable-swirl burner through a gravimetric feeder. The secondary and tertiary oxidizer streams are pre-heated to temperatures up to 600 K, while the over-fire oxidizer stream is located down the furnace and can be plumbed into the furnace at any section. Eddings et al. [444] conducted experiments on the 1.5 MW pilot-scale

combustor (L1500) to evaluate the performance of co-firing pulverized coal with either raw wood, torrefied wood or bio-char. They found that the pollutant emissions (NO$_x$, CO and SO$_2$) are similar between the baseline coal firing and biomass co-firing for any of the forms of the biomass. Fry et al. [445] conducted experiments in the 1.5 MW combustor to investigate the differences between air- and oxy-fired flame behaviors, including video images of the flames and the radiation intensity along the flame length. The experimental data confirm that an air-like flame can be established by burning pulverized coal with a mixture of oxygen and flue-gas recirculation (FGR). The ignition delay, flame shape and intensity in oxy-coal flames can be modified by adjusting the mixing of O$_2$ and FGR.

7.3. Industrial-scale combustion furnaces

As computational power has become widely available, in recent years simulations of industrial-scale furnaces have been conducted. As a substantial body of work employing RANS with low mesh resolutions has been conducted for industrial-scale furnaces over long periods [337, 446–450], in this section we only focus on recent progress on LES for large-scale furnaces.

The Carbon-Capture Multidisciplinary Simulation Center (CCMSC) at the University of Utah conducted LESs of Alstom industrial-scale furnaces operated at 15 MW [451] and 342 MW [452], as shown in Fig. 30. The simulations were conducted on the platform of the Uintah software [453,454] using the Arches module. Uintah is a massively parallel code that solves conserved quantities spatially and temporally in a turbulent flow field. The particle phase is represented in an Eulerian framework using the direct quadrature method of moments (DQMOM), in which the physical coal-particle processes include devolatilization, char oxidation, swelling, shrinkage and body forces. The DQMOM method can predict the particle size distribution (see the top row of Fig. 30), particle velocities and other particle properties. Recently, Adamczyk et al. [452] conducted LESs to study the air-staging process (ROFA) of an industrial-scale, pulverized-coal boiler (OP-430, 100% load: 342 MW). Two configurations have been studied, the original one consisting in the standard configuration of OFA nozzles (one level of OFA ports) and the modified one involving air staging by distributing air over the upper part of the combustion chamber (four levels of the ROFA ports). The obtained instantaneous distribution of the O$_2$ volume fraction are shown in the bottom panel of Fig. 30. The simulation results for the original configuration were compared to the experimental data, and the differences between the simulation results for the original and modified configurations were analyzed. It was found that the difference between the simulation results and experimental data varies between 2% and 20% depending on the value of interest (O$_2$, NO$_x$, temperature).

7.4. Reference coal gasification systems

Compared to pulverized coal combustion, only a few studies have investigated entrained-flow gasification. In this section, we focus on three different scales of representative coal gasifiers to illustrate how advances in coal gasification submodel development have been introduced in CFD simulations.

The first is the research-scale coal gasifier developed at CRIEPI, operated at 2 metric tons/day (T/D) [455], shown schematically in Fig. 31 (a). The gasifier has a combustor and a reductor. In the combustor, coal and char are burnt with secondary air, while the burnt products such as ash are discharged as molten slag. The flue gas introduced from the combustor is introduced to the reductor and mixed with the pulverized coal from the reductor, whereupon the devolatilization and the gasification reaction occur. Unburnt char at the gasifier is collected by a cyclone and is reintroduced to the combustor. Watanabe and Otaka [455] conducted a RANS simulation for the CRIEPI gasifier taking into account pyrolysis, char gasification and gas phase reactions. The devolatilization rate was calculated with a primary reaction model,

while the gasification rate of char particles was calculated using the model parameters obtained by Kajitani et al. [456], who employed the random pore model [225]. For the gas phase reactions, a simple five-step global reaction scheme was used. The gas temperature and species concentrations predicted by the adopted numerical model were found to agree with the experimental data under different operating conditions (air ratio).

Another widely used reference configuration is the laboratory-scale entrained-flow gasifier at Brigham Young University (BYU) [327] shown in Fig. 31 (b). The diameter of the reactor is 20 cm and its total vertical length 2 m. The pulverized coal is entrained into the gasifier by the primary gas stream composed of Ar, O_2 and H_2O. A secondary stream of steam is introduced into the chamber through a concentric annular duct. Brown et al. [327] conducted the first simulation of this gasifier using their CFD code PCGC-2 (pulverized coal gasification and combustion, two-dimensional) [334] employing RANS turbulence modeling and a two-mixture fraction-based approach for TCI. Particularly, heat losses due to radiation and convection were considered in the energy equation by introducing a heat loss factor. Kumar and Ghoniem [306] conducted a RANS simulation of this gasifier using the EBU model coupled with the simplified char surface reaction model. The devolatilization rate was characterized with the advanced CPD model. Abani and Ghoniem [344] then conducted a LES for the same gasifier in order to capture some of the unsteady structures that affect mixing, turbulent-chemistry interactions, turbulence dispersion of particles, etc. The devolatilization rate was calculated using the Badzioch and Hawksley model [63], the char surface reaction rate was characterized using the Field model [402] and the effect of turbulence on homogeneous combustion was described employing a partially stirred reactor (PaSR) approach [459]. The simulation results obtained with the LES were compared to those from RANS with the same coal combustion submodels and the experimental data. It was found that, compared to the RANS simulations, LES can offer better predictions since the unsteady flow structures can be captured. To overcome the limitation of the conventional devolatilization approaches, Vascellari et al. adopted an advanced coal devolatilization model [41] and later advanced char models [332]. Single particle trajectories were extracted to study the reactive boundary layer around the particles under oxidizing and reducing atmospheres [316]. The turbulence-chemistry interactions were characterized with the EDC model, while the char surface reaction rate was calculated with the Field model. The devolatilization and char conversion model was developed by calibrating simple empirical models using results either from experiments or advanced models. This has been described in detail in the previous sections.

The Siemens 5 MW pilot-scale gasifier, shown schematically in Fig. 31 (c), is equipped with water-cooled membrane walls and a partial water quench. Pulverized coal and oxidizer are fed to the burner at the top of the gasifier, while products and slag leave the gasifier at the bottom. Vascellari et al. [41] adopted the same numerical models as for the BYU coal gasifier to simulate the Siemens gasifier. The kinetic models were adjusted based on available experimental data and simulations using detailed pyrolysis and char conversion models. It was found that the simulations adequately predict the measured syngas species concentrations and the carbon conversion at the exit of the reactor. Halama and Spliethoff [457] conducted a RANS simulation for this gasifier using the EDC model to describe the chemical reaction rate. The two-competing-rates model was used to describe the devolatilization rate, while an advanced char surface reaction model was adopted to describe the gasification rate from the char particles. An n-th order effectiveness factor approach with intrinsic reaction kinetics was adopted to take into account the pore diffusion and boundary layer diffusion, and the influence of thermal deactivation on the reactivity of the char surface was also included in the char surface reaction model. Overall, very good results were obtained given the experimental uncertainties that are unavoidable for systems on that scale.

8. Summary and future challenges

The present article reviewed advanced models for the simulation of coal combustion and gasification. Three particularly important and relevant areas were identified:

- Solid phase kinetics and their integration in CFD,
- The turbulent flow and mixing field,
- Turbulence – gas-phase chemistry interaction (TCI),

all of which are strongly coupled in combustion chambers and gasification reactors.

The main results in these three areas are briefly summarized below, and the need for further research and the associated challenges are also presented. Finally, an outlook is given and suggestions made as to how the results in the three areas should be combined in the next generation of CFD simulations of coal combustion and gasification and how the coupling can be systematically validated on the basis of reference configurations.

8.1. Solid phase kinetics and their integration in CFD

Detailed network-based models for pyrolysis are very advanced. Even without experimental data, volatile release can be reliably described for a wide range of coals. For some models there is still potential, especially in the release of pollutant precursors.

For the description of char conversion, there are a number of models which differ greatly in terms of their complexity and the number of subprocesses considered. Compared to the pyrolysis models, there is an overall greater need for experimental data to determine the heterogeneous kinetics. A major reason for this, besides the influence of the parent coal, is the strong dependence of the char structure (and thus the reactivity) on the preceding pyrolysis. For higher temperatures, not only the heterogeneous surface kinetics, but also pore or film diffusion in the particle boundary layer become rate-determining. Since oxidation reactions are much faster than gasification reactions, transport limitations occur much earlier in oxidizing than in reducing atmospheres. Therefore, the determination of the heterogeneous kinetics for gasification is particularly important in order to predict overall char conversion for such conditions. This is also relevant for oxyfuel atmospheres, where the contribution of gasification reactions increases significantly compared to combustion in air.

Pyrolysis and char conversion models have been developed separately. When the entire thermo-chemical conversion process is simulated, they must be coupled in a suitable way; whereby the processes are often assumed to be purely consecutive for the sake of simplification. This problem is avoided in the semi-empirical framework developed by the CRECK group. All individual steps are represented in one kinetic model. This builds on four reference monomeric structures that are bonded repeatedly in the polymeric macrostructure of coal. All fuels are represented as mixtures of these reference structures. The kinetic parameters are calibrated on the basis of measurements. Each of the four reference structures has its own mechanism.

Integrating these detailed models into the CFD is a particular challenge. The detailed models, especially, have only been used comparatively rarely in 3D-CFD, either because of the computational time required or because an interface was lacking. Instead, a number of methods have been developed to calibrate simplified kinetic models, such as one- or two-step models for pyrolysis, with the detailed models for a wide range of operating conditions. Recently published work suggests that methods based on machine learning are also promising to reduce the models.

There are **two main challenges and corresponding research needs** for the future. Firstly, kinetic models must be continuously developed further. Important aspects here include char reactivity, the release of pollutant precursors and catalytic effects of minerals.

Secondly, the detailed kinetic information must be more intensively used than today in 3D-CFD. Many current studies still use highly simplified and not sufficiently calibrated models. For this, the coupling strategies in particular have to be improved, including their numerical efficiency with respect to scale-resolving methods.

8.2. Turbulent flow and mixing field

While the vast majority of CFD simulations of coal combustion and gasification are RANS-based, scale-resolving methods such as LESs, and in some cases even DNSs, are used, particularly in more recent studies. These approaches allow complex features to be captured, such as unsteadiness, ignition and combustion instabilities. A similar transition from RANS to LES was observed some time ago for turbulent gas phase combustion. In academia, especially for laboratory configurations, LES has almost completely replaced standard RANS approaches. Especially for complex systems such as gas turbines or engines, both approaches are used equally today, both in university and industrial environments.

Furthermore, some DNS studies of simplified configurations have been published. These data are particularly suitable for a detailed analysis of certain physical effects such as ignition in turbulent flows or TCI in general or the release of precursors and the subsequent formation of pollutants. Based on this data, models can be developed and validated using the DNS data.

Future research should focus on the further establishment of LESs. Operating conditions should be analyzed where effects such as stability are relevant; this can only be investigated to a limited extent with RANS methods. An essential point here is that advanced models for solid fuel kinetics and TCI are also used fully coupled in LES. This is also discussed in the outlook below.

So far, only a few turbulent DNS studies are available, but these are very valuable for developing models and thus for improving a comprehensive, LES-based simulation methodology. Future DNSs should in particular integrate detailed models for solid- and gas-phase kinetics. The two mechanisms must be compatible and, for example, make the same assumptions for tar species. The interesting scientific topics which then emerge include ignition, stability and pollutant formation, in particular. The local conditions for the DNS should be extracted from LES studies of combustion chambers or gasification reactors.

8.3. Turbulence – gas phase chemistry interaction (TCI)

Turbulent combustion is characterized by a strong interaction of turbulent mixing and chemical reactions. TCI has been a very active field of research for many years. For gas-phase combustion in particular, a number of models for premixed and non-premixed combustion have been developed and successfully applied in LES. Here, too, one key factor was close cooperation with the experiments, leading to corresponding reference burners being developed and extensive data sets provided for the validation.

Turbulent coal flames pose two particular challenges compared to single-phase gaseous combustion. First, a complex mixture of light gases and tars is released from the solid fuel. The reactions of this large number of species have to be described by a suitable chemical mechanism that has to cover not only oxidizing but also reducing conditions. Due to the very different molecular sizes of the released species, the possibility cannot be excluded of the species' different molecular diffusivities influencing the structure of the reaction zone. Secondly, a number of studies have shown that the release of the gases from the coal or char particle leads to very complex flame structures. Non-premixed and premixed reaction zones can occur in close proximity and interact with each other. These complex structures are highly dependent on local conditions and may differ from case to case. TCI models for coal combustion should therefore be applicable for different combustion regimes and should be able to adapt locally to the regime.

In recent years, a number of studies have been published on the development of advanced TCI models for coal combustion. Without exception, these have built on the experience gained for turbulent gasphase combustion and have systematically further developed the models for coal, e.g. to consider multiple fuel streams/mixture fractions. A number of configurations such as particle-laden counterflow or stagnation point flames, jet flames or mixing layers have been investigated. For some configurations turbulent DNS data were also available. The majority of the studies are based on the flamelet concept. One advantage is that flamelet manifolds can be generated and tabulated in advance, which permits the efficient use of large chemical reaction mechanisms. Research has not yet determined the multi-regime data characteristics or the probability/filtered density functions (PDFs/FDFs), as investigated, for example, in transported PDF approaches.

In these studies, a number of differences to gas-phase combustion have been identified, which have to be considered in the models. One example is the formation of NO_x in the near-burner region. While thermal NO formation in gas flames, in particular, is characterized by slow time scales, in coal flames it is shown that the NO_x formation is similarly fast to the combustion reactions, due to the release of precursors and their subsequent reactions.

The development of advanced TCI models for coal combustion and gasification is still at a quite early stage and there are many open scientific questions. **Future research** should focus, among other things, on the consistent coupling of gas- and solid-phase chemistry. Due to the large number of gases released, the reaction mechanisms must be compatible. This also includes the precursors and the formation of pollutants, e.g. the release of tars from coal; and their further reactions, either decomposition into smaller species or further growth into soot, should be represented by both the chemistry and the TCI model. Another focus should be the multi-regime character of coal flames. For this purpose, the models have to be systematically evaluated, developed and validated. This should take into account extremely unsteady processes such as ignition or flames at the stability limit. It is crucial to further couple these TCI models for use in LESs.

8.4. Outlook on future comprehensive 3D-CFD simulations of coal combustion and gasification

The relevant physical and chemical processes as well as their numerical modeling were discussed on the basis of the three areas above. Significant progress has been made in all three areas in recent years. A number of LES studies from the last years have shown that the rapid increase in computer resources is offering detailed insights into local processes which determine the global behavior (stability, carbon consumption, etc.) in combustion chambers; this was previously unthinkable.

A goal for the future should therefore be to integrate the respective advances into CFD simulations and to investigate the interactions. Initial published work describes the coupling of two of the three areas, e.g. LES-flamelet or LES with detailed multi-step/multi-species solid fuel kinetics. However, to the best of the authors' knowledge there are no comprehensive CFD studies to date that have coupled the most advanced approaches from all three areas and systematically investigated their interaction and relevance for combustion chambers of different sizes (from laboratory to pilot scale) and their complexity. Suitable reference configurations for this purpose have been presented in a separate section of this article. Extensive numerical studies of this kind, always in comparison with experimental data, are absolutely necessary to quantitatively evaluate the predictive power of current approaches and to define the need for future research on further developing models in the three areas, and on coupling them.

Declaration of Competing Interest

The authors declare that they have no known competing financial interests or personal relationships that could have appeared to influence

the work reported in this paper.

Acknowledgements

References

[1] British Petroleum BP. Economics BP energy. BP Energy Outlook; 2020. 2020.
[2] IEA IEA. Global Energy Review 2020. Paris: 2020.
[3] British Petroleum BP. Economics BP energy. Stat Rev World Energy 2020. 2020.
[4] Council WE. World Energy Scenarios 2019 - Exploring innovation pathways to 2040. n.d.
[5] EIA USEIA. International Energy Outlook 2019. IEO 2019; 2019.
[6] IEA IEA. Key World Energy Statistics 2020. Paris: 2020.
[7] You CF, Xu XC. Coal combustion and its pollution control in China. Energy 2010; 35:4467–72. https://doi.org/10.1016/j.energy.2009.04.019.
[8] Council WE. World Energy Scenarios 2016 - The Grand Transition. World Energy Council; 2016.
[9] British Petroleum BP. economics BP energy. BP Energy Outlook. 2018th ed. BP energy economics; 2019. 2019.
[10] Chen L, Yong SZ, Ghoniem AF. Oxy-fuel combustion of pulverized coal: Characterization, fundamentals, stabilization and CFD modeling. Prog Energy Combust Sci 2012;38:156–214.
[11] Eaton AM, Smoot LD, Hill SC, Eatough CN. Components, formulations, solutions, evaluation, and application of comprehensive combustion models. Prog Energy Combust Sci 1999;25:387–436. https://doi.org/10.1016/S0360-1285(99)00008-8.
[12] Zhao X-Y, Haworth DC. Transported PDF modeling of pulverized coal jet flames. Combust Flame 2014;161:1866–82. https://doi.org/10.1016/j.combustflame.2013.12.024.
[13] Wen X, Luo K, Wang H, Luo Y, Fan J. Analysis of pulverized coal flame stabilized in a 3D laminar counterflow. Combust Flame 2018;189:106–25. https://doi.org/10.1016/j.combustflame.2017.10.021.
[14] Wen X, Fan J. Flamelet modeling of laminar pulverized coal combustion with different particle sizes. Adv Powder Technol 2019;30:2964–79. https://doi.org/10.1016/j.apt.2019.09.004.
[15] Olenik G, Stein OT, Kronenburg A. LES of swirl-stabilised pulverised coal combustion in IFRF furnace No. 1. Proc Combust Inst 2015;35:2819–28. https://doi.org/10.1016/j.proci.2014.06.149.
[16] Cheng P. Two-Dimensional Radiating Gas Flow by a Moment Method. AIAA J 1964;2:1662–4. https://doi.org/10.2514/3.2645.
[17] Rieth M, Proch F, Rabaçal M, Franchetti BM, Cavallo Marincola F, Kempf AM. Flamelet LES of a semi-industrial pulverized coal furnace. Combust Flame 2016; 173:39–56. https://doi.org/10.1016/j.combustflame.2016.07.013.
[18] Rieth M, Clements AG, Rabaçal M, Proch F, Stein OT, Kempf AM. Flamelet LES modeling of coal combustion with detailed devolatilization by directly coupled CPD. Proc Combust Inst 2017;36:2181–9. https://doi.org/10.1016/j.proci.2016.06.077.
[19] Hara T, Muto M, Kitano T, Kurose R, Komori S. Direct numerical simulation of a pulverized coal jet flame employing a global volatile matter reaction scheme based on detailed reaction mechanism. Combust Flame 2015;162:4391–407. https://doi.org/10.1016/j.combustflame.2015.07.027.
[20] Stöllinger M, Naud B, Roekaerts D, Beishuizen N, Heinz S. PDF modeling and simulations of pulverized coal combustion – Part 1: Theory and modeling. Combust Flame 2013;160:384–95. https://doi.org/10.1016/j.combustflame.2012.10.010.
[21] Stöllinger M, Naud B, Roekaerts D, Beishuizen N, Heinz S. PDF modeling and simulations of pulverized coal combustion – Part 2: Application. Combust Flame 2013;160:396–410. https://doi.org/10.1016/j.combustflame.2012.10.011.
[22] Nicolai H, Wen X, Miranda FCFC, Zabrodiec D, Massmeyer A, Mare F di, et al. Numerical investigation of swirl-stabilized pulverized coal flames in air and oxy-fuel atmospheres by means of Large Eddy simulation coupled with tabulated chemistry. Fuel 2020;119429. https://doi.org/10.1016/j.fuel.2020.119429.
[23] Truelove JS. Discrete-Ordinate Solutions of the Radiation Transport Equation. J Heat Transfer 1987;109:1048–51. https://doi.org/10.1115/1.3248182.
[24] Smith TF, Shen ZF, Friedman JN. Evaluation of Coefficients for the Weighted Sum of Gray Gases Model. J Heat Transfer 1982;104:602–8. https://doi.org/10.1115/1.3245174.
[25] Wu B, Roy SP, Zhao X, Modest MF. Effect of multiphase radiation on coal combustion in a pulverized coal jet flame. J Quant Spectrosc Radiat Transf 2017; 197:154–65. https://doi.org/10.1016/j.jqsrt.2017.03.017.
[26] Zhu C, Tu H, Bai Y, Ma D, Zhao Y. Evaluation of slagging and fouling characteristics during Zhundong coal co-firing with a Si/Al dominated low rank coal. Fuel 2019;254:115730. https://doi.org/10.1016/j.fuel.2019.115730.
[27] Zhao Y, Huang Q, Yao Q, Li S. Prediction and validation of ash sticking probability under fouling conditions in pulverized coal combustion. Proc Combust Inst 2020. https://doi.org/10.1016/j.proci.2020.06.053. Accepted.
[28] Niu Y, Tan H, Hui S. Ash-related issues during biomass combustion: Alkali-induced slagging, silicate melt-induced slagging (ash fusion), agglomeration, corrosion, ash utilization, and related countermeasures. Prog Energy Combust Sci 2016;52:1–61. https://doi.org/10.1016/j.pecs.2015.09.003.
[29] Chen L, Yong SZ, Ghoniem AF. Oxy-fuel combustion of pulverized coal: Characterization, fundamentals, stabilization and CFD modeling. Prog Energy Combust Sci 2012;38:156–214. https://doi.org/10.1016/j.pecs.2011.09.003.
[30] Fan Y, Lyu Q, Zhu Z, Zhang H. The impact of additives upon the slagging and fouling during Zhundong coal gasification. J Energy Inst 2020;93:1651–65. https://doi.org/10.1016/j.joei.2020.02.003.
[31] Li S, Xu Y, Gao Q. Measurements and modelling of oxy-fuel coal combustion. Proc Combust Inst 2019;37:2643–61. https://doi.org/10.1016/j.proci.2018.08.054.
[32] Wan K, Vervisch L, Xia J, Domingo P, Wang Z, Liu Y, et al. Alkali metal emissions in an early-stage pulverized-coal flame: DNS analysis of reacting layers and chemistry tabulation. Proc Combust Inst 2019;37:2791–9. https://doi.org/10.1016/j.proci.2018.06.119.
[33] Kerstein AR, Niksa S. Fragmentation during carbon conversion: Predictions and measurements. Symp Combust 1985;20:941–9. https://doi.org/10.1016/S0082-0784(85)80583-X.
[34] Kerstein AR, Edwards BF. Percolation model for simulation of char oxidation and fragmentation time-histories. Chem Eng Sci 1987;42:1629–34. https://doi.org/10.1016/0009-2509(87)80167-7.
[35] Salatino P, Miccio F, Massimilla L. Combustion and percolative fragmentation of carbons. Combust Flame 1993;95:342–50. https://doi.org/10.1016/0010-2180(93)90002-K.
[36] Gao Q, Li S, Zhao Y, Yao Q. Mechanism on the contribution of coal/char fragmentation to fly ash formation during pulverized coal combustion. Proc Combust Inst 2019;37:2831–9. https://doi.org/10.1016/j.proci.2018.05.092.
[37] Senneca O, Bareschino P, Urciuolo M, Chirone R. Prediction of structure evolution and fragmentation phenomena during combustion of coal: Effects of heating rate. Fuel Process Technol 2017;166:228–36. https://doi.org/10.1016/j.fuproc.2017.06.010.
[38] Senneca O, Heuer S, Bareschino P, Urciuolo M, Pepe F, Schiemann M, et al. Fragmentation of pulverized coal in a laminar drop tube reactor: Experiments and model. Proc Combust Inst 2019;37:2849–55. https://doi.org/10.1016/j.proci.2018.08.057.
[39] Kreutzkam B, Wieland C, Spliethoff H. Improved numerical prediction of ash formation and deposition using a novel developed char fragmentation model. Fuel 2012;98:103–10. https://doi.org/10.1016/j.fuel.2012.02.056.
[40] Anthony DB, Howard JB. Coal devolatilization and hydrogastification. AIChE J 1976;22:625–56. https://doi.org/10.1002/aic.690220403.
[41] Vascellari M, Arora R, Pollack M, Hasse C. Simulation of entrained flow gasification with advanced coal conversion submodels. Part 1: Pyrolysis. Fuel 2013;113:654–69. https://doi.org/10.1016/j.fuel.2013.06.014.
[42] Niksa S. Process Chemistry of Coal Utilization: Impacts of coal quality and operating conditions. London: Woodhead Publishing, Elsevier; 2019. https://doi.org/10.1016/C2018-0-04246-2.
[43] Gavalas GR. Coal pyrolysis, 4. New York: Elsevier; 1982.
[44] Grant DM, Pugmire RJ, Fletcher TH, Kerstein AR. Chemical Model of Coal Devolatilization Using Percolation Lattice Statistics. Energy Fuels 1989;3:175–86. https://doi.org/10.1021/ef00014a011.
[45] Smith KL, Smoot LD, Fletcher TH, Pugmire RJ. The structure and reaction processes of coal. Springer Science & Business Media. 1st ed. 1994.
[46] Solomon PR. Chemistry of coal conversion. New York: Plenum Press; 1985.
[47] Fletcher TH. Review of 30 Years of Research Using the Chemical Percolation Devolatilization Model. Energy Fuels 2019;33:12123–53. https://doi.org/10.1021/acs.energyfuels.9b02826.
[48] Richards AP, Fletcher TH. A comparison of simple global kinetic models for coal devolatilization with the CPD model. Fuel 2016;185:171–80. https://doi.org/10.1016/j.fuel.2016.07.095.
[49] Maffei T. Kinetic Model of Coal Combustion. Technical University Milan; 2013.
[50] Fletcher TH, Kerstein AR, Pugmire RJ, Solum MS, Grant DM. A chemical percolation model for devolatilization: Summary. Combustion Research Facility. Sandia National Laboratories; 1992.
[51] Davidson RM. Molecular Structure of Coal. Coal Sci. 1982:83–160. https://doi.org/10.1016/B978-0-12-150701-5.50009-7.
[52] Fletcher TH, Kerstein AR, Pugmire RJ, Grant DM. Chemical percolation model for devolatilization. 2. Temperature and heating rate effects on product yields. Energy Fuels 1990;4:54–60. https://doi.org/10.1021/ef00019a010.
[53] Solomon PR. Relation Between Coal Structure and Thermal Decomposition Products. Coal Struct., vol. 192. AMERICAN CHEMICAL SOCIETY; 1981. p. 95–112. https://doi.org/10.1021/ba-1981-0192.ch007.10.1021/ba-1981-0192.ch007.
[54] Fletcher TH, Ma J, Rigby JR, Brown AL, Webb BW. Soot in coal combustion systems. Prog Energy Combust Sci 1997;23:283–301.
[55] Josephson AJ, Linn RR, Lignell DO. Modeling soot formation from solid complex fuels. Combust Flame 2018;196:265–83. https://doi.org/10.1016/j.combustflame.2018.06.020.
[56] Oberlin A, Oberlin M. Graphitizability of carbonaceous materials as studied by TEM and X-ray diffraction. J Microsc 1983;132:353–63.

[57] Debiagi P, Gentile G, Cuoci A, Frassoldati A, Ranzi E, Faravelli T. A predictive model of biochar formation and characterization. J Anal Appl Pyrolysis 2018;134: 326–35. https://doi.org/10.1016/j.jaap.2018.06.022.

[58] Oberlin A. Carbonization and graphitization. Carbon N Y 1984;22:521–41. https://doi.org/10.1016/0008-6223(84)90086-1.

[59] Rouzaud JN, Oberlin A. Structure, microtexture, and optical properties of anthracene and saccharose-based carbons. Carbon N Y 1989;27:517–29.

[60] Holland T, Fletcher TH, Senneca O. Review of Carbonaceous Annealing Effects on O$_2$ and CO$_2$ Coal Reactivity. Energy Fuels 2019;33:10415–34. https://doi.org/10.1021/acs.energyfuels.9b02698.

[62] Gürüz GA, Üçtepe Ü, Durusoy T. Mathematical modeling of thermal decomposition of coal. J Anal Appl Pyrolysis 2004;71:537–51. https://doi.org/10.1016/j.jaap.2003.08.007.

[63] Badzioch S, Hawksley PGW. Kinetics of Thermal Decomposition of Pulverized Coal Particles. Ind Eng Chem Process Des Dev 1970;9:521–30. https://doi.org/10.1021/i260036a005.

[64] Anthony DB, Howard JB, Hottel HC, Meissner HP. Rapid devolatilization of pulverized coal. Symp. Combust. 1975;15:1303–17.

[65] Kobayashi H, Howard JB, Sarofim AF. Coal devolatilization at high temperatures. Symp Combust 1977;16:411–25. https://doi.org/10.1016/S0082-0784(77)80341-X.

[66] Solomon PR, Colket MB. Coal devolatilization. Symp. Combust. 1979;17:131–43.

[67] Yu J, Lucas JA, Wall TF. Formation of the structure of chars during devolatilization of pulverized coal and its thermoproperties: A review. Prog Energy Combust Sci 2007;33:135–70. https://doi.org/10.1016/j.pecs.2006.07.003.

[68] Pitt GJ. The kinetics of the evolution of volatile products from coal. Fuel 1962;41: 267–74.

[69] Sun Q, Li W, Chen H, Li B, Sun Q. Devolatilization Characteristics of Shenmu Coal Macerals and Kinetic Analysis. Energy Sources Part A Recover Util Environ Eff 2006;28:865–74. https://doi.org/10.1080/009083190910361.

[70] Miura K. A New and Simple Method to Estimate f(E) and k$_0$(E) in the Distributed Activation Energy Model from Three Sets of Experimental Data. Energy Fuels 1995;9:302–7. https://doi.org/10.1021/ef00050a014.

[71] Miura K, Maki T. A Simple Method for Estimating f(E) and k$_0$(E) in the Distributed Activation Energy Model. Energy Fuels 1998;12:864–9. https://doi.org/10.1021/ef970212q.

[72] Cai J, Liu R. New distributed activation energy model: Numerical solution and application to pyrolysis kinetics of some types of biomass. Bioresour Technol 2008;99:2795–9. https://doi.org/10.1016/j.biortech.2007.06.033.

[73] Cai J, Jin C, Yang S, Chen Y. Logistic distributed activation energy model – Part 1: Derivation and numerical parametric study. Bioresour Technol 2011;102: 1556–61. https://doi.org/10.1016/j.biortech.2010.08.079.

[74] Cai J, Yang S, Li T. Logistic distributed activation energy model – Part 2: Application to cellulose pyrolysis. Bioresour Technol 2011;102:3642–4. https://doi.org/10.1016/j.biortech.2010.11.073.

[75] Donskoi E, McElwain DLS. Optimization of coal pyrolysis modeling. Combust Flame 2000;122:359–67.

[76] Abramowitz M, Stegun IA. Handbook of mathematical functions: with formulas, graphs, and mathematical tables, 55. Courier Corporation; 1965.

[77] Niksa S, Kerstein AR. FLASHCHAIN theory for rapid coal devolatilization kinetics. 1. Formulation. Energy Fuels 1991;5:647–65. https://doi.org/10.1021/ef00029a006.

[78] Solomon PR, Hamblen DG, Carangelo RM, Serio MA, Deshpande G V. General model of coal devolatilization. Energy Fuels 1988;2:405–22. https://doi.org/10.1021/ef00010a006.

[79] Fletcher TH, Kerstein AR, Pugmire RJ, Solum MS, Grant DM. Chemical percolation model for devolatilization. 3. Direct use of ^{13}C NMR data to predict effects of coal type. Energy Fuels 1992;6:414–31. https://doi.org/10.1021/ef00034a011.

[80] Fletcher TH, Pugmire RJ. Chemical Percolation Model for Coal Devolatilization 2011;2015. http://www.et.byu.edu/~tom/cpd/cpdcodes.html.

[81] Solum MS, Pugmire RJ, Grant DM. ^{13}C Solid-State NMR of Argonne Premium Coals. Energy Fuels 1989;3:187–93. https://doi.org/10.1021/ef00014a012.

[82] Genetti D, Fletcher TH, Pugmire RJ. Development and Application of a Correlation of ^{13}C NMR Chemical Structural Analyses of Coal Based on Elemental Composition and Volatile Matter Content. Energy Fuels 1999;13:60–8. https://doi.org/10.1021/ef980074k.

[83] Solomon PR, Serio MA, Carangelo RM, Bassilakis R, Gravel D, Baillargeon M, et al. Analysis of the Argonne premium coal samples by thermogravimetric Fourier transform infrared spectroscopy. Energy Fuels 1990;4:319–33. https://doi.org/10.1021/ef00021a017.

[84] Chen JC, Niksa S. Coal devolatilization during rapid transient heating. 1. Primary devolatilization. Energy Fuels 1992;6:254–64. https://doi.org/10.1021/ef00033a004.

[85] Jupudi RS, Zamansky V, Fletcher TH. Prediction of Light Gas Composition in Coal Devolatilization. Energy Fuels 2009;23:3063–7. https://doi.org/10.1021/ef9001346.

[86] Umemoto S, Kajitani S, Miura K, Watanabe H, Kawase M. Extension of the chemical percolation devolatilization model for predicting formation of tar compounds as soot precursor in coal gasification. Fuel Process Technol 2017;159: 256–65. https://doi.org/10.1016/j.fuproc.2017.01.037.

[87] Umemoto S, Kajitani S, Hara S, Kawase M. Proposal of a new soot quantification method and investigation of soot formation behavior in coal gasification. Fuel 2016;167:280–7. https://doi.org/10.1016/j.fuel.2015.11.074.

[88] Yu LE, Hildemann LM, Niksa S. Trends in Aromatic Ring Number Distributions of Coal Tars during Secondary Pyrolysis. Energy Fuels 1998;12:450–6. https://doi.org/10.1021/ef9700590.

[89] Niksa S. The distributed-energy chain model for rapid coal devolatilization kinetics. Part II: Transient weight loss correlations. Combust Flame 1986;66: 111–9. https://doi.org/10.1016/0010-2180(86)90083-0.

[90] Niksa S, Kerstein AR. The distributed-energy chain model for rapid coal devolatilization kinetics. Part I: Formulation. Combust Flame 1986;66:95–109. https://doi.org/10.1016/0010-2180(86)90082-9.

[91] Niksa S, Kerstein AR. On the role of macromolecular configuration in rapid coal devolatilization. Fuel 1987;66:1389–99. https://doi.org/10.1016/0016-2361(87)90186-4.

[92] Kerstein AR, Niksa S. Polymer Scission with Irreversible Reattachment: A Kinetic Model of Pyrolysis with Char Formation. Macromolecules 1987;20:1811–8. https://doi.org/10.1021/ma00174a019.

[93] Genetti DB. An Advanced Model of Coal Devolatilization Based on Chemical Structure. Brigham Young University; 1999.

[94] Genetti D, Fletcher TH. Modeling Nitrogen Release during Devolatilization on the Basis of Chemical Structure of Coal. Energy Fuels 1999;13:1082–91. https://doi.org/10.1021/ef990056i.

[95] Perry ST, Fletcher TH, Solum MS, Pugmire RJ. Modeling nitrogen evolution during coal pyrolysis based on a global free-radical mechanism. Energy Fuels 2000;14:1094–102. https://doi.org/10.1021/ef000061i.

[96] Perry ST, Fletcher TH. A global free-radical mechanism for nitrogen release during coal devolatilization based on chemical structure. Brigham Young University; 1999.

[97] Niksa S. FLASHCHAIN theory for rapid coal devolatilization kinetics. 2. Impact of operating conditions. Energy Fuels 1991;5:665–73. https://doi.org/10.1021/ef00029a007.

[98] Niksa S. FLASHCHAIN theory for rapid coal devolatilization kinetics. 3. Modeling the behavior of various coals. Energy Fuels 1991;5:673–83. https://doi.org/10.1021/ef00029a008.

[99] Niksa S. FLASHCHAIN Theory for Rapid Coal Devolatilization Kinetics. 4. Predicting Ultimate Yields from Ultimate Analyses Alone. Energy Fuels 1994;8: 659–70. https://doi.org/10.1021/ef00045a022.

[100] Niksa S. FLASHCHAIN Theory for Rapid Coal Devolatilization Kinetics. 5. Interpreting Rates of Devolatilization for Various Coal Types and Operating Conditions. Energy Fuels 1994;8:671–9. https://doi.org/10.1021/ef00045a023.

[101] Niksa S. FLASHCHAIN Theory for Rapid Coal Devolatilization Kinetics. 6. Predicting the Evolution of Fuel Nitrogen from Various Coals. Energy Fuels 1995; 9:467–78. https://doi.org/10.1021/ef0051a011.

[102] Niksa S. FLASHCHAIN Theory for Rapid Coal Devolatilization Kinetics. 7. Predicting the Release of Oxygen Species from Various Coals. Energy Fuels 1996; 10:173–87. https://doi.org/10.1021/ef950067l.

[103] Niksa S. FLASHCHAIN Theory for Rapid Coal Devolatilization Kinetics. 8. Modeling the Release of Sulfur Species from Various Coals. Energy Fuels 2017;31: 4925–38. https://doi.org/10.1021/acs.energyfuels.7b00278.

[104] Niksa S. FLASHCHAIN Theory for Rapid Coal Devolatilization Kinetics. 9. Decomposition Mechanism for Tars from Various Coals Energy Fuels 2017;31: 9080–93. https://doi.org/10.1021/acs.energyfuels.7b01349.

[105] Niksa S. FLASHCHAIN Theory for Rapid Coal Devolatilization Kinetics. 10. Extents of Conversion for Hydropyrolysis and Hydrogasification of Any Coal. Energy Fuels 2018;32:384–95. https://doi.org/10.1021/acs.energyfuels.7b03064.

[106] Niksa S. FLASHCHAIN Theory for Rapid Coal Devolatilization Kinetics. 11. Tar Hydroconversion during Hydrogasification of Any Coal. Energy Fuels 2018;32: 7569–84. https://doi.org/10.1021/acs.energyfuels.8b01614.

[107] Niksa S. Rapid Coal Devolatilization As an Equilibrium Flash Distillation. AIChE J 1988;34:790–802. https://doi.org/10.1002/aic.690340509.

[108] Niksa S. PC Coal Lab version 5.1: User guide and tutorial 2020.

[109] Strugała A. Empirical formulae for calculation of real density and total pore volume of hard coals. Fuel 1994;73:1781–5. https://doi.org/10.1016/0016-2361(94)90168-6.

[110] Niksa S. Predicting the rapid devolatilization of diverse forms of biomass with bio-flashchain. Proc Combust Inst 2000;28:2727–33. https://doi.org/10.1016/S0082-0784(00)80693-1.

[111] Gavalas GR, Cheong PH-K, Jain R. Model of coal pyrolysis. 1. Qualitative development. Ind Eng Chem Fundam 1981;20:113–22. https://doi.org/10.1021/i100002a001.

[112] Gavalas GR, Jain R, Cheong PH-K. Model of coal pyrolysis. 2. Quantitative formulation and results. Ind Eng Chem Fundam 1981;20:122–32. https://doi.org/10.1021/i100002a002.

[113] Suuberg EM, Unger PE, Lilly WD. Experimental study on mass transfer from pyrolysing coal particles. Fuel 1985;64:956–62. https://doi.org/10.1016/0016-2361(85)90151-6.

[114] Unger PE, Suuberg EM. Modeling the devolatilization behavior of a softening bituminous coal. Symp Combust 1981;18:1203–11. https://doi.org/10.1016/S0082-0784(81)80124-5.

[115] Solomon PR, Serio MA, Suuberg EM. Coal pyrolysis: Experiments, kinetic rates and mechanisms. Prog Energy Combust Sci 1992;18:133–220. https://doi.org/10.1016/0360-1285(92)90021-R.

[116] Bassilakis R, Zhao Y, Solomon PR, Serio MA. Sulfur and nitrogen evolution in the Argonne coals. Experiment and modeling. Energy Fuels 1993;7:710–20. https://doi.org/10.1021/ef00042a004.

[117] Hurt RH, Sun J-K, Lunden MM. A Kinetic Model of Carbon Burnout in Pulverized Coal Combustion. Combust Flame 1998;113:181–97. https://doi.org/10.1016/s0010-2180(97)00240-x.

[118] Su S, Song Y, Wang Y, Li T, Hu S, Xiang J, et al. Effects of CO_2 and heating rate on the characteristics of chars prepared in CO_2 and N_2 atmospheres. Fuel 2015;142: 243–9.

[119] Laurendeau NM. Heterogeneous kinetics of coal char gasification and combustion. Prog Energy Combust Sci 1978;4:221–70. https://doi.org/10.1016/0360-1285(78)90008-4.

[120] Hou J, Ma Y, Li S, Shang W. A comparative study on characteristics of sulfur and nitrogen transformation and gaseous emission for combustion of bituminous coal and char. Carbon Resour Convers 2018.

[121] Annamalai K, Ryan W. Interactive processes in gasification and combustion—II. Isolated carbon, coal and porous char particles. Prog Energy Combust Sci 1993; 19:383–446.

[122] Coetzee GH, Sakurovs R, Neomagus HWJP, Everson RC, Mathews JP, Bunt JR. Particle size influence on the pore development of nanopores in coal gasification chars: From micron to millimeter particles. Carbon N Y 2017;112:37–46.

[123] Walker PL, Rusinko F, Austin LG, Eley DD, Selwood PW, Weisz PB. Gas Reactions of Carbon. Adv. Catal. 1959;11:133–221. https://doi.org/10.1016/S0360-0564 (08)60418-6.

[124] Gray D, Cogoli JG, Essenhigh RH. Problems in Pulverized Coal and Char Combustion. In: Massey LG, editor. Coal Gasif., vol. 131. editor. American Chemical Society; 1974. p. 72–91. https://doi.org/10.1021/ba-1974-0131. ch006.

[125] Smoot LD, Smith PJ. Coal combustion and gasification. 1st ed. New York: Plenum Press; 1985.

[126] Liu G-S, Niksa S. Coal conversion submodels for design applications at elevated pressures. Part II. Char gasification. Prog Energy Combust Sci 2004;30:679–717. https://doi.org/10.1016/j.pecs.2004.08.001.

[127] Sun J-K, Hurt RH. Mechanisms of extinction and near-extinction in pulverized solid fuel combustion. Proc Combust Inst 2000;28:2205–13. https://doi.org/10.1016/S0082-0784(00)80630-X.

[128] Vascellari M, Roberts DG, Hla SS, Harris DJ, Hasse C. From laboratory-scale experiments to industrial-scale CFD simulations of entrained flow coal gasification. Fuel 2015;152:58–73. https://doi.org/10.1016/j.fuel.2015.01.038.

[129] Geier M, Shaddix CR, Davis KA, Shim H-S. On the use of single-film models to describe the oxy-fuel combustion of pulverized coal char. Appl Energy 2012;93: 675–9. https://doi.org/10.1016/j.apenergy.2011.12.097.

[130] Hecht ES, Shaddix CR, Molina A, Haynes BS. Effect of CO_2 gasification reaction on oxy-combustion of pulverized coal char. Proc Combust Inst 2011;33:1699–706. https://doi.org/10.1016/j.proci.2010.07.087.

[131] Hecht ES, Shaddix CR, Geier M, Molina A, Haynes BS. Effect of CO_2 and steam gasification reactions on the oxy-combustion of pulverized coal char. Combust Flame 2012;159:3437–47. https://doi.org/10.1016/j. combustflame.2012.06.009.

[132] Hong J. Modeling char oxidation as a function of pressure using an intrinsic Langmuir rate equation. Brigham Young University; 2000.

[133] Niksa S, Liu G, Hurt RH. Coal conversion submodels for design applications at elevated pressures. Part I. devolatilization and char oxidation. Prog Energy Combust Sci 2003;29:425–77. https://doi.org/10.1016/S0360-1285(03)00033-9.

[134] Arthur JR. Reactions between carbon and oxygen. Trans Faraday Soc 1951;47: 164–78.

[135] Yi L, Feng J, Qin Y-H, Li W-Y. Prediction of elemental composition of coal using proximate analysis. Fuel 2017;193:315–21. https://doi.org/10.1016/j. fuel.2016.12.044.

[136] Kilpinen P, Kallio S, Konttinen J, Barišić V. Char-nitrogen oxidation under fluidised bed combustion conditions: single particle studies. Fuel 2002;81: 2349–62. https://doi.org/10.1016/S0016-2361(02)00176-X.

[137] Nikolopoulos A, Malgarinos I, Nikolopoulos N, Grammelis P, Karrelas S, Kakaras E. A decoupled approach for NOx–N2O 3-D CFD modeling in CFB plants. Fuel 2014;115:401–15. https://doi.org/10.1016/j.fuel.2013.06.036.

[138] Debiagi P, Yildiz C, Ströhle J, Epple B, Faravelli T, Hasse C. Systematic evaluation and kinetic modeling of low heating rate sulfur release in various atmospheres. Fuel 2021;289:119739. https://doi.org/10.1016/j.fuel.2020.119739.

[139] Molina A, Murphy JJ, Winter F, Haynes BS, Blevins LG, Shaddix CR. Pathways for conversion of char nitrogen to nitric oxide during pulverized coal combustion. Combust Flame 2009;156:574–87. https://doi.org/10.1016/j. combustflame.2008.11.012.

[140] Tian F-J, Yu J, McKenzie LJ, Hayashi J, Li C-Z. Conversion of Fuel-N into HCN and NH3 During the Pyrolysis and Gasification in Steam: A Comparative Study of Coal and Biomass †. Energy Fuels 2007;21:517–21. https://doi.org/10.1021/ ef060415r.

[141] Molina A, Sarofim AF, Ren W, Lu J, Yue G, Beér JM, et al. Effect of boundary layer reactions on the conversion of CHAR-N to NO, N2O, and HCN at fluidized-bed combustion conditions. Combust Sci Technol 2002;174:43–71. https://doi.org/ 10.1080/713712945.

[142] Bläsing M, Müller M. Influence of pressure on the release of inorganic species during high temperature gasification of coal. Fuel 2011;90:2326–33. https://doi. org/10.1016/j.fuel.2011.02.013.

[143] Wang X, Guo H, Liu F, Hu R, Wang M. Effects of CO_2 on sulfur removal and its release behavior during coal pyrolysis. Fuel 2016;165:484–9. https://doi.org/ 10.1016/j.fuel.2015.10.047.

[144] Guo F, Wu R, Baxter LL, Hecker WC. Models To Predict Kinetics of NOx Reduction by Chars as a Function of Coal Rank. Energy Fuels 2019;33:5498–504. https:// doi.org/10.1021/acs.energyfuels.8b03655.

[145] Smith IW. The combustion rates of coal chars: A review. Symp Combust 1982;19: 1045–65. https://doi.org/10.1016/S0082-0784(82)80281-6.

[146] Monson CR, Germane GJ, Blackham AU, Smoot LD. Char oxidation at elevated pressures. Combust Flame 1995;100:669–83. https://doi.org/10.1016/0010-2180(94)00178-U.

[147] Hurt RH, Mitchell RE. Unified high-temperature char combustion kinetics for a suite of coals of various rank. Symp Combust 1992;24:1243–50. https://doi.org/ 10.1016/s0082-0784(06)80146-3.

[148] Hurt RH, Calo JM. Semi-Global Intrinsic Kinetics for Char Combustion Modeling. Combust Flame 2001;125:1138–49. https://doi.org/10.1016/s0010-2180(01) 00234-6.

[149] Langmuir I, Part II. Heterogeneous reactions". Chemical reactions on surfaces. Trans Faraday Soc 1922;17:607–20.

[150] Brown TC, Lear AE, Haynes BS. Oxygen chemisorption on carbon. Symp. Combust. 1992;24:1199–206.

[151] Du Z, Sarofim AF, Longwell JP. Activation energy distribution in temperature-programmed desorption: modeling and application to the soot oxygen system. Energy Fuels 1990;4:296–302.

[152] Elliott MA. Chemistry of coal utilization. Second supplementary volume 1981.

[153] Haynes BS, Newbury TG. Oxyreactivity of carbon surface oxides. Proc Combust Inst 2000;28:2197–203.

[154] Ranish JM, Walker Jr PL. High pressure studies of the carbon-oxygen reaction. Carbon N Y 1993;31:135–41. https://doi.org/10.1016/0008-6223(93)90166-8.

[155] Field MA. Measurements of the effect of rank on combustion rates of pulverized coal. Combust Flame 1970;14:237–48.

[156] Hamor RJ, Smith IW, Tyler RJ. Kinetics of combustion of a pulverized brown coal char between 630 and 2200°K. Combust Flame 1973;21:153–62. https://doi.org/ 10.1016/S0010-2180(73)80020-3.

[157] Lin S-Y, Suzuki Y, Hatano H, Tsuchiya K. Pressure effect on char combustion in different rate-control zones:: initial rate expression. Chem Eng Sci 2000;55:43–50.

[158] Smith IW. Kinetics of combustion of size-graded pulverized fuels in the temperature range 1200–2270 K. Combust Flame 1971;17:303–14.

[159] Smith IW, Tyler RJ. The reactivity of a porous brown coal char to oxygen between 630 and 1812 K. Combust Sci Technol 1974;9:87–94.

[160] Sørensen LH, Gjernes E, Jessen T, Fjellerup J. Determination of reactivity parameters of model carbons, cokes and flame-chars. Fuel 1996;75:31–8.

[161] Hong J, Hecker WC, Fletcher TH. Modeling high-pressure char oxidation using langmuir kinetics with an effectiveness factor. Proc Combust Inst 2000;28: 2215–23. https://doi.org/10.1016/S0082-0784(00)80631-1.

[162] Hecker WC, McDonald KM, Reade W, Swensen MR, Cope RF. Effects of burnout on char oxidation kinetics. Symp. Combust., vol. 24. Elsevier; 1992. p. 1225–31.

[163] Essenhigh RH, Mescher AM. Influence of pressure on the combustion rate of carbon. Symp. Combust., vol. 26. Elsevier; 1996. p. 3085–94.

[164] Suuberg EM, Wójtowicz M, Calo JM. Reaction order for low temperature oxidation of carbons. Symp. Combust., vol. 22. Elsevier; 1989. p. 79–87.

[165] Croiset E, Mallet C, Rouan J-P, Richard J-R. The influence of pressure on char combustion kinetics. Symp. Combust., vol. 26. Elsevier; 1996. p. 3095–102.

[166] Mitchell RE, McLean WJ. On the temperature and reaction rate of burning pulverized fuels. Symp Combust 1982;19:1113–22. https://doi.org/10.1016/ S0082-0784(82)80287-7.

[167] Kurylko L, Essenhigh RH. Steady and unsteady combustion of carbon. Symp. Combust., vol. 14. Elsevier; 1973. p. 1375–86.

[168] Young BC, Smith IW. The kinetics of combustion of petroleum coke particles at 1000 to 1800 K: The reaction order. Symp. Combust., vol. 18. Elsevier; 1981. p. 1249–55.

[169] Harris DJ, Smith IW. Intrinsic reactivity of petroleum coke and brown coal char to carbon dioxide, steam and oxygen. Symp. Combust., vol. 23. Elsevier; 1991. p. 1185–90.

[170] Gadsby J, Long FJ, Sleightholm P, Sykes KW. The mechanism of the carbon dioxide-carbon reaction. Proc R Soc London Ser A Math Phys Sci 1948;193: 357–76.

[171] Roberts DG, Harris DJ. Char gasification in mixtures of CO_2 and H_2O: Competition and inhibition. Fuel 2007;86:2672–8. https://doi.org/10.1016/j. fuel.2007.03.019.

[172] Roberts DG, Harris DJ. High-Pressure Char Gasification Kinetics: CO Inhibition of the C–CO 2 Reaction. Energy Fuels 2012;26:176–84. https://doi.org/10.1021/ ef201174k.

[173] Huang Z, Zhang J, Zhao Y, Zhang H, Yue G, Suda T, et al. Kinetic studies of char gasification by steam and CO_2 in the presence of H_2 and CO. Fuel Process Technol 2010;91:843–7. https://doi.org/10.1016/j.fuproc.2009.12.020.

[174] Everson RC, Neomagus HWJP, Kasaini H, Njapha D. Reaction kinetics of pulverized coal-chars derived from inertinite-rich coal discards: Characterisation and combustion. Fuel 2006;85:1067–75. https://doi.org/10.1016/j. fuel.2005.10.025.

[175] Umemoto S, Kajitani S, Hara S. Modeling of coal char gasification in coexistence of CO_2 and H_2O considering sharing of active sites. Fuel 2013;103:14–21.

[176] Montoya A, Mondragón F, Truong TN. Formation of CO precursors during char gasification with O_2, CO_2 and H_2O. Fuel Process Technol 2002;77:125–30.

[177] Jiang W, Nadeau G, Zaghib K, Kinoshita K. Thermal analysis of the oxidation of natural graphite - Effect of particle size. Thermochim Acta 2000;351:85–93. https://doi.org/10.1016/S0040-6031(00)00416-0.

[178] Rouquerol J, Avnir D, Fairbridge CW, Everett DH, Haynes JM, Pernicone N, et al. Recommendations for the characterization of porous solids (Technical Report). Pure Appl Chem 1994;66:1739–58. https://doi.org/10.1351/pac199466081739.

[179] Benfell KE, Liu G-S, Roberts DG, Harris DJ, Lucas JA, Bailey JG, et al. Modeling char combustion: The influence of parent coal petrography and pyrolysis pressure

on the structure and intrinsic reactivity of its char. Proc Combust Inst 2000;28: 2233–41. https://doi.org/10.1016/S0082-0784(00)80633-5.

[180] Bailey JG, Tate A, Diessel CFK, Wall TF. A char morphology system with applications to coal combustion. Fuel 1990;69:225–39. https://doi.org/10.1016/0016-2361(90)90179-T.

[181] Lightman P, Street PJ. Microscopical examination of heat treated pulverised coal particles. Fuel 1968;47:7–28.

[182] Wu H, Bryant G, Benfell K, Wall T. An Experimental Study on the Effect of System Pressure on Char Structure of an Australian Bituminous Coal. Energy Fuels 2000; 14:282–90. https://doi.org/10.1021/ef990066j.

[183] Thiele EW. Relation between Catalytic Activity and Size of Particle. Ind Eng Chem 1939;31:916–20. https://doi.org/10.1021/ie50355a027.

[184] Reade WC. An Improved Method for Predicting High-Temperature Char Oxidation Rates. Brigham Young University; 1996.

[185] Bischoff KB. Effectiveness Factors for General Reaction Rate Forms. AIChE J 1965; 11:351–5. https://doi.org/10.1002/aic.690110229.

[186] Aris R. The mathematical theory of diffusion and reaction in permeable catalysts: The theory of the steady state. Oxford: Oxford University Press; 1975.

[187] Roberts DG, Harris DJ. Char Gasification with O_2, CO_2, and H_2O: Effects of Pressure on Intrinsic Reaction Kinetics. Energy Fuels 2000;14:483–9. https://doi.org/10.1021/ef9901894.

[188] Campbell PA, Mitchell RE, Ma L. Characterization of coal char and biomass char reactivities to oxygen. Proc Combust Inst 2002;29:519–26. https://doi.org/10.1016/S1540-7489(02)80067-0.

[189] Hurt RH, Sarofim AF, Longwell JP. Role of microporous surface area in uncatalyzed carbon gasification. Energy Fuels 1991;5:290–9.

[190] Hurt RH, Sarofim AF, Longwell JP. The role of microporous surface area in the gasification of chars from a sub-bituminous coal. Fuel 1991;70:1079–82.

[191] Su J, Perlmutter DD. Effect of pore structure on char oxidation kinetics. AIChE J 1985;31:973–81.

[192] Ballal G, Zygourakis K. Evolution of pore surface area during noncatalytic gas-solid reactions. 1. Model development. Ind Eng Chem Res 1987;26:911–21.

[193] Beath AC. Mathematical Modelling of Entrained Flow Coal Gasification. Australia: University of Newcastle; 1996.

[194] Balci S, Dogu G, Dogu T. Structural variations and a deactivation model for gasification of coal. Ind Eng Chem Res 1987;26:1454–8.

[195] Smith IW, Tyler RJ. Internal burning of pulverized semi-anthracite: the relation between particle structure and reactivity. Fuel 1972;51:312–21.

[196] Wheeler A. Reaction rates and selectivity in catalyst pores. In: Frankenburg WG, Komarewsky VI, Rideal EK, Emmett PH, Taylor HS, editors. Adv. Catal., vol. 3. editors. Elsevier; 1951. p. 249–327. https://doi.org/10.1016/S0360-0564(08)60109-1.

[197] Georgakis C, Chang CW, Szekely J. A changing grain size model for gas—solid reactions. Chem Eng Sci 1979;34:1072–5.

[198] Szekely J, Evans JW. A structural model for gas-solid reactions with a moving boundary-II: The effect of grain size, porosity and temperature on the reaction of porous pellets. Chem Eng Sci 1971;26:1901–13.

[199] Szekely J, Propster M. A structural model for gas solid reactions with a moving boundary—VI: The effect of grain size distribution on the conversion of porous solids. Chem Eng Sci 1975;30:1049–55.

[200] Gavalas GR. A random capillary model with application to char gasification at chemically controlled rates. AIChE J 1980;26:577–85.

[201] Chin G, Kimura S, Tone S, Otake T. Gasification of coal char with steam. Part 1. Analysis of reaction rate. Int Chem Eng;(United States) 1983:23.

[202] Chin G, Kimura S, Tone S, Otake T. Gasification of coal char with steam. Part 2. Pore structure and reactivity. Int Chem Eng;(United States) 1983:23.

[203] Su J, Perlmutter DD. Evolution of pore volume distribution during gasification. AIChE J 1984;30:967–73.

[204] Bliek A, Lont JC, van Swaaij WPM. Gasification of coal-derived chars in synthesis gas mixtures under intraparticle mass-transfer-controlled conditions. Chem Eng Sci 1986;41:1895–909.

[205] Chi W, Perlmutter DD. The effect of pore structure on the char-steam reaction. AIChE J 1989;35:1791–802.

[206] Ballal G, Zygourakis K. Evolution of pore surface area during noncatalytic gas-solid reactions. 2. Experimental results and model validation. Ind Eng Chem Res 1987;26:1787–96.

[207] Charpenay S, Serio MA, Solomon PR. The prediction of coal char reactivity under combustion conditions. Symp. Combust. 1992;24:1189–97.

[208] Simons GA, ML FINSON. The structure of coal char: Part I—pore branching. Combust Sci Technol 1979;19:217–25.

[209] Simons GA. The Structure of Coal Char: Part II.—Pore Combination. Combust Sci Technol 1979;19:227–35.

[210] Foster MD, Jensen KF. Small angle X-ray scattering investigations of pore structure changes during coal gasification. Fuel 1990;69:88–96.

[211] Miccio F, Monte-Carlo Salatino P. Simulation of combustion-induced percolative fragmentation of carbons. Symp. Combust., 24. Elsevier; 1992. p. 1145–51.

[212] Sandmann Jr CW, Zygourakis K. Evolution of pore structure during gas-solid reactions: discrete models. Chem Eng Sci 1986;41:733–9.

[213] Reyes S, Jensen KF. Percolation concepts in modelling of gas-solid reactions—I. Application to char gasification in the kinetic regime. Chem Eng Sci 1986;41: 333–43.

[214] Reyes S, Jensen KF. Percolation concepts in modelling of gas-solid reactions—II. Application to char gasification in the diffusion regime. Chem Eng Sci 1986;41: 345–54.

[215] Mann R, Almeida JJ, Mugerwa MN. A random pattern extension to the stochastic network pore model. Chem Eng Sci 1986;41:2663–71.

[216] Shah N, Ottino JM. Transport and reaction in evolving, disordered composites-I. Gasification of porous solids. Chem Eng Sci 1987;42:63–72.

[217] Adanez J, Miranda JL. Gasificación del carbón: reactividad de carbones. Ing Química 1986:129–34.

[218] Raghunathan K, Yang RYK. Unification of coal gasification data and its applications. Ind Eng Chem Res 1989;28:518–23.

[219] Liliedahl T, Sjöström K. Modelling of char-gas reaction kinetics. Fuel 1997;76: 29–37.

[220] Adschiri T, Shiraha T, Kojima T, Furusawa T. Prediction of CO_2 gasification rate of char in fluidized bed gasifier. Fuel 1986;65:1688–93.

[221] Goyal A, Zabransky RF, Rehmat A. Gasification kinetics of Western Kentucky bituminous coal char. Ind Eng Chem Res 1989;28:1767–78.

[222] Yang Y, Watkinson AP. Gasification reactivity of some Western Canadian coals. Fuel 1994;73:1786–91.

[223] Lee WJ, Kim SD. Catalytic activity of alkali and transition metal salt mixtures for steam-char gasification. Fuel 1995;74:1387–93.

[224] Dutta S, Wen CY, Belt RJ. Reactivity of Coal and Char. 1. In Carbon Dioxide Atmosphere. Ind Eng Chem Process Des Dev 1977;16:20–30. https://doi.org/10.1021/i260061a004.

[225] Bhatia SK, Perlmutter DD. A Random Pore Model for Fluid-Solid Reactions: I. Isothermal, Kinetic Control. AIChE J 1980;26:379–86. https://doi.org/10.1002/aic.690260308.

[226] Bhatia SK, Perlmutter DD. A Random Pore Model for Fluid-Solid Reactions: II. Diffusion and Transport Effects. AIChE J 1981;27:247–54. https://doi.org/10.1002/aic.690270211.

[227] Carberry JJ. The Micro-Macro Effectiveness Factor for the Reversible Catalytic Reaction. AIChE J 1962;8:557–8. https://doi.org/10.1002/aic.690080428.

[228] Hurt RH. Structure, properties, and reactivity of solid fuels. Symp Combust 1998; 27:2887–904. https://doi.org/10.1016/s0082-0784(98)80148-3.

[229] Mitchell R, Hurt R, Baxter L, Hardesty D. Compilation of Sandia coal char combustion data and kinetic analyses. Albuquerque, NM, and Livermore, CA (United States): Sandia National Laboratories; 1992. https://doi.org/10.2172/7045508.

[230] Haugen NEL, Tilghman MB, Mitchell RE. The conversion mode of a porous carbon particle during oxidation and gasification. Combust Flame 2014;161:612–9. https://doi.org/10.1016/j.combustflame.2013.09.012.

[231] Haugen NEL, Mitchell RE, Tilghman MB. A comprehensive model for char particle conversion in environments containing O_2 and CO_2. Combust Flame 2015;162: 1455–63. https://doi.org/10.1016/j.combustflame.2014.11.015.

[232] Haynes BS. A turnover model for carbon reactivity I. development. Combust Flame 2001;126:1421–32.

[233] Turns SR. An Introduction to Combustion: Concepts and Applications. 3rd ed. New York: McGraw-Hill; 2012.

[234] Hecht ES, Shaddix CR, Lighty JS. Analysis of the errors associated with typical pulverized coal char combustion modeling assumptions for oxy-fuel combustion. Combust Flame 2013;160:1499–509. https://doi.org/10.1016/j.combustflame.2013.02.015.

[235] Ashman P, Haynes B, Nelson PF, Nancarrow PC, Bus J, Nicholls PM, et al. Improved techniqued for the prediction of NOx formation from char nitrogen. Australia: North Ryde NSW; 1999.

[236] Matalon M. Complete Burning and Extinction of a Carbon Particle in an Pxidizing Atmosphere. Combust Sci Technol 1980;24:115–27.

[237] Field MA, Gill DW, Morgan BB, Hawksley PGW. British Coal Utilisation Research A, Essenhigh RH. Combustion of pulverized coal. Leatherhead (Sy.): B.C.U.R.A.; 1967.

[238] Caram HS, Amundson NR. Diffusion and reaction in a stagnant boundary layer about a carbon particle. Ind Eng Chem Fundam 1977;16:171–81.

[239] Frankcombe TJ, Bhatia SK, Smith SC. Ab initio modelling of basal plane oxidation of graphenes and implications for modelling char combustion. Carbon N Y 2002; 40:2341–9. https://doi.org/10.1016/S0008-6223(02)00147-1.

[240] Shi T, Wang X, Deng J, Wen Z. The mechanism at the initial stage of the room-temperature oxidation of coal. Combust Flame 2005;140:332–45. https://doi.org/10.1016/j.combustflame.2004.10.012.

[241] Singh RI, Mebel AM, Frenklach M. Oxidation of Graphene-Edge Six- and Five-Member Rings by Molecular Oxygen. J Phys Chem A 2015;119:7528–47. https://doi.org/10.1021/acs.jpca.5b00868.

[242] Semenikhin AS, Savchenkova AS, Chechet IV, Matveev SG, Liu Z, Frenklach M, et al. Rate constants for H abstraction from benzo(a)pyrene and chrysene: a theoretical study. Phys Chem Chem Phys 2017;19:25401–13. https://doi.org/10.1039/C7CP05560A.

[243] Pykal M, Jurečka P, Karlický F, Otyepka M. Modelling of graphene functionalization. Phys Chem Chem Phys 2016;18:6351–72. https://doi.org/10.1039/C5CP03599F.

[244] Hurt RH, Lunden MM, Brehob EG, Maloney DJ. Statistical kinetics for pulverized coal combustion. Symp Combust 1996;26:3169–77. https://doi.org/10.1016/s0082-0784(96)80162-7.

[245] Benfell KE. Assessment of char morphology in high pressure pyrolysis and combustion. Australia: University of Newcastle; 2001.

[246] Shurtz RC. Effects of Pressure on the Properties of Coal Char Under Gasification Conditions at High Initial Heating Rates. Brigham Young University; 2011.

[247] Shurtz RC, Fletcher TH. Coal Char-CO_2 Gasification Measurements and Modeling in a Pressurized Flat-Flame Burner. Energy Fuels 2013;27:3022–38. https://doi.org/10.1021/ef400253c.

[248] Holland T, Fletcher TH. Global Sensitivity Analysis for a Comprehensive Char Conversion Model in Oxy-fuel Conditions. Energy Fuels 2016;30:9339–50. https://doi.org/10.1021/acs.energyfuels.6b02190.

[249] Holland TM. A Comprehensive Coal Conversion Model Extended to Oxy-Coal Conditionse. Brigham Young University; 2017.

[250] Holland T, Fletcher TH. Comprehensive Model of Single Particle Pulverized Coal Combustion Extended to Oxy-Coal Conditions. Energy Fuels 2017;31:2722–39. https://doi.org/10.1021/acs.energyfuels.6b03387.

[251] Holland T, Bhat S, Marcy P, Gattiker J, Kress JD, Fletcher TH. Modeling Effects of Annealing on Coal Char Reactivity to O_2 and CO_2, Based on Preparation Conditions. Energy Fuels 2017;31:10727–44. https://doi.org/10.1021/acs.energyfuels.7b01888.

[252] Tremel A, Haselsteiner T, Kunze C, Spliethoff H. Experimental investigation of high temperature and high pressure coal gasification. Appl Energy 2012;92:279–85. https://doi.org/10.1016/j.apenergy.2011.11.009.

[253] Tremel A, Haselsteiner T, Nakonz M, Spliethoff H. Coal and char properties in high temperature entrained flow gasification. Energy 2012;45:176–82. https://doi.org/10.1016/j.energy.2012.02.028.

[254] Tremel A. Reaction Kinetics of Solid Fuels during Entrained Flow Gasification. Technische Universität München; 2012.

[255] Tremel A, Spliethoff H. Gasification kinetics during entrained flow gasification – Part I: Devolatilisation and char deactivation. Fuel 2013;103:663–71. https://doi.org/10.1016/j.fuel.2012.09.014.

[256] Tremel A, Spliethoff H. Gasification kinetics during entrained flow gasification – Part II: Intrinsic char reaction rate and surface area development. Fuel 2013;107:653–61. https://doi.org/10.1016/j.fuel.2012.10.053.

[257] Tremel A, Spliethoff H. Gasification kinetics during entrained flow gasification – Part III: Modelling and optimisation of entrained flow gasifiers. Fuel 2013;107:170–82. https://doi.org/10.1016/j.fuel.2013.01.062.

[258] Harris DJ, Roberts DG, Henderson DG. Gasification behaviour of Australian coals at high temperature and pressure. Fuel 2006;85:134–42. https://doi.org/10.1016/j.fuel.2005.07.022.

[259] Hodge EM. The Coal Char-CO_2 Reaction at high Temperature and high Pressure. Australia: University of New South Wales; 2009.

[260] Hurt RH, Mitchell RE. On the combustion kinetics of heterogeneous char particle populations. Symp. Combust. 1992;24:1233–41.

[261] Campbell PA. Investigation into the Roles of Surface Oxide Complexes and their Distributions in the Carbon-Oxygen Heterogeneous Reaction Mechanism. Stanford, CA: Stanford University; 2005.

[262] Ma L. Combustion and Gasification of Chars in Oxygen and Carbon Dioxide at Elevated Pressures. Stanford, CA: Stanford University; 2006.

[263] Ma L, Mitchell RE. Modeling char oxidation behavior under Zone II burning conditions at elevated pressures. Combust Flame 2009;156:37–50. https://doi.org/10.1016/j.combustflame.2008.06.015.

[264] Campbell PA, Mitchell RE. The impact of the distributions of surface oxides and their migration on characterization of the heterogeneous carbon–oxygen reaction. Combust Flame 2008;154:47–66. https://doi.org/10.1016/j.combustflame.2007.11.002.

[265] Tilghman MB, Mitchell RE. Coal and biomass char reactivities in gasification and combustion environments. Combust Flame 2015;162:3220–35. https://doi.org/10.1016/j.combustflame.2015.05.009.

[266] Tilghman MB, Haugen NEL, Mitchell RE. Comprehensive Char Particle Gasification Model Adequate for Entrained-Flow and Fluidized-Bed Gasifiers. Energy Fuels 2017;31:2164–74. https://doi.org/10.1021/acs.energyfuels.6b02148.

[267] Louw E. Structure and combustion reactivity of inertinite-rich and vitrinite rich South African coal chars: quantification of the structural factors contributing to reactivity differences 2012.

[268] Wang C, Watson JK, Louw E, Mathews JP. Construction Strategy for Atomistic Models of Coal Chars Capturing Stacking Diversity and Pore Size Distribution. Energy Fuels 2015;29:4814–26. https://doi.org/10.1021/acs.energyfuels.5b00816.

[269] Xin H, Wang C, Louw E, Wang D, Mathews JP. Atomistic simulation of coal char isothermal oxy-fuel combustion: Char reactivity and behavior. Fuel 2016;182:935–43. https://doi.org/10.1016/j.fuel.2016.05.103.

[270] Louw EB, Mitchell GD, Wang J, Winans RE, Mathews JP. Constitution of Drop-Tube-Generated Coal Chars from Vitrinite- and Inertinite-Rich South African Coals. Energy Fuels 2016;30:112–20. https://doi.org/10.1021/acs.energyfuels.5b01517.

[271] Zhong Q, Mao Q, Xiao J, van Duin ACT, Mathews JP. ReaxFF simulations of petroleum coke sulfur removal mechanisms during pyrolysis and combustion. Combust Flame 2018;198:146–57. https://doi.org/10.1016/j.combustflame.2018.09.005.

[272] Zhong Q, Zhang Y, Shabnam S, Xiao J, Van Duin ACT, Mathews JP. Reductive Gaseous (H2/NH3) Desulfurization and Gasification of High-Sulfur Petroleum Coke via Reactive Force Field Molecular Dynamics Simulations. Energy Fuels 2019;33:8065–75. https://doi.org/10.1021/acs.energyfuels.9b01425.

[273] Migliavacca G, Parodi E, Bonfanti L, Faravelli T, Pierucci S, Ranzi E. A general mathematical model of solid fuels pyrolysis. Energy 2005;30:1453–68. https://doi.org/10.1016/j.energy.2004.02.011.

[274] Sommariva S, Maffei T, Migliavacca G, Faravelli T, Ranzi E. A predictive multi-step kinetic model of coal devolatilization. Fuel 2010;89:318–28. https://doi.org/10.1016/j.fuel.2009.07.023.

[275] Maffei T, Sommariva S, Ranzi E, Faravelli T. A predictive kinetic model of sulfur release from coal. Fuel 2012;91:213–23. https://doi.org/10.1016/j.fuel.2011.08.017.

[276] Maffei T, Frassoldati A, Cuoci A, Ranzi E, Faravelli T. Predictive one step kinetic model of coal pyrolysis for CFD applications. Proc Combust Inst 2013;34:2401–10. https://doi.org/10.1016/j.proci.2012.08.006.

[277] Debiagi P, Ranzi E, Faravelli T, Hasse C. Coal Combustion: Integrating Nitrogen and Sulfur Fraction in a Single Kinetic Mechanism. 1st Int. In: Conf. smart energy carriers; 2019.

[278] Maffei T, Khatami R, Pierucci S, Faravelli T, Ranzi E, Levendis YA. Experimental and modeling study of single coal particle combustion in O_2/N_2 and Oxy-fuel (O_2/CO_2) atmospheres. Combust Flame 2013;160:2559–72. https://doi.org/10.1016/j.combustflame.2013.06.002.

[279] Ranzi E, Faravelli T, Manenti F. Chapter One - Pyrolysis, Gasification, and Combustion of Solid Fuels. In: Geem KM Van, editor. Thermochem. Process Eng., vol. 49, Academic Press; 2016, p. 1–94. https://doi.org/https://doi.org/10.1016/bs.ache.2016.09.001.

[280] Debiagi PEA, Pecchi C, Gentile G, Frassoldati A, Cuoci A, Faravelli T, et al. Extractives Extend the Applicability of Multistep Kinetic Scheme of Biomass Pyrolysis. Energy Fuels 2015;29:6544–55. https://doi.org/10.1021/acs.energyfuels.5b01753.

[281] Ranzi E, Debiagi PEA, Frassoldati A. Mathematical Modeling of Fast Biomass Pyrolysis and Bio-Oil Formation. Note I: Kinetic Mechanism of Biomass Pyrolysis. ACS Sustain Chem Eng 2017;5:2867–81. https://doi.org/10.1021/acssuschemeng.6b03096.

[282] Ranzi E, Debiagi PEA, Frassoldati A. Mathematical Modeling of Fast Biomass Pyrolysis and Bio-Oil Formation. Note II: Secondary Gas-Phase Reactions and Bio-Oil Formation. ACS Sustain Chem Eng 2017;5:2882–96. https://doi.org/10.1021/acssuschemeng.6b03098.

[283] Debiagi PEA, Gentile G, Cuoci A, Frassoldati A, Ranzi E, Faravelli T. Yield, composition and active surface area of char from biomass pyrolysis. Chem Eng Trans 2018;65:97–102. https://doi.org/10.3303/CET1865017.

[284] Debiagi PEA, Trinchera M, Frassoldati A, Faravelli T, Vinu R, Ranzi E. Algae characterization and multistep pyrolysis mechanism. J Anal Appl Pyrolysis 2017;128:423–36. https://doi.org/10.1016/j.jaap.2017.08.007.

[285] Özer B, Debiagi PEA, Hasse C, Faravelli T, Kazanç F. An experimental and numerical study on the combustion of lignites from different geographic origins. Fuel 2020;278:118320. https://doi.org/10.1016/j.fuel.2020.118320.

[286] Heuer S, Schiemann M, Scherer V. Determination of devolatilization kinetics in inert and CO_2-enriched atmospheres in a plug flow reactor. In: 32nd Annu. Int. Pittsburgh Coal Conf. Coal - Energy, Environ. Sustain. Dev. IPCC; 2015. p. 2015. https://doi.org/10.13140/RG.2.1.1603.2726.

[287] Lopez-Peinado AJ, Tromp PJJ, Moulijn JA. Quantitative heat effects associated with pyrolysis of coals, ranging from anthracite to lignite. Fuel 1989;68:999–1004. https://doi.org/10.1016/0016-2361(89)90065-3.

[288] Senneca O, Cortese L. Kinetics of coal oxy-combustion by means of different experimental techniques. Fuel 2012;102:751–9.

[289] Tognotti L, Longwell JP, Sarofim AF. The products of the high temperature oxidation of a single char particle in an electrodynamic balance. Symp. Combust. 1991;23:1207–13.

[290] Skokova KA. Selectivity in the carbon-oxygen reaction. The Pennsylvania State University; 1997.

[291] Debiagi P, Yildiz C, Richter M, Ströhle J, Epple B, Faravelli T, et al. Experimental and modeling assessment of sulfur release from coal under low and high heating rates. Proc Combust Inst 2021;38:4053–61. https://doi.org/10.1016/j.proci.2020.06.121.

[292] Shamooni A, Debiagi P, Wang B, Luu TD, Stein OT, Kronenburg A, et al. Carrier-phase DNS of detailed NOx formation in early-stage pulverized coal combustion with fuel-bound nitrogen. Fuel 2021;291:119998. https://doi.org/10.1016/j.fuel.2020.119998.

[293] Frigge L, Elserafi G, Ströhle J, Epple B. Sulfur and Chlorine Gas Species Formation during Coal Pyrolysis in Nitrogen and Carbon Dioxide Atmosphere. Energy Fuels 2016;30:7713–20. https://doi.org/10.1021/acs.energyfuels.6b01080.

[294] Glarborg P, Jensen AD, Johnsson JE. Fuel nitrogen conversion in solid fuel fired systems. Prog Energy Combust Sci 2003;29:89–113.

[295] Glarborg P. Fuel nitrogen conversion in solid fuel fired systems. Prog Energy Combust Sci 2003;29:89–113. https://doi.org/10.1016/S0360-1285(02)00031-X.

[296] Wu Z, Ohtsuka Y. Key Factors for Formation of N_2 from Low-Rank Coals during Fixed Bed Pyrolysis: Pyrolysis Conditions and Inherent Minerals. Energy Fuels 1997;11:902–8. https://doi.org/10.1021/ef9700238.

[297] Wu Z, Sugimoto Y, Kawashima H. Formation of N_2 from Pyrrolic and Pyridinic Nitrogen during Pyrolysis of Nitrogen-Containing Model Coals. Energy Fuels 2003;17:694–8. https://doi.org/10.1021/ef020184y.

[298] Debiagi P, Ontyd C, Pielsticker S, Schiemann M, Faravelli T, Kneer R, et al. Calibration and validation of a comprehensive kinetic model of coal conversion in inert, air and oxy-fuel conditions using data from multiple test rigs. Fuel 2020. https://doi.org/10.1016/j.fuel.2020.119682. Under revi:119682.

[299] Wan K, Xia J, Wang Z, Wrobel LC, Cen K. Online-CPD-Coupled Large-Eddy Simulation of Pulverized-Coal Pyrolysis in a Hot Turbulent Nitrogen Jet. Combust Sci Technol 2017;189:103–31. https://doi.org/10.1080/00102202.2016.1193498.

[300] Goshayeshi B, Sutherland JC. A comparison of various models in predicting ignition delay in single-particle coal combustion. Combust Flame 2014;161:1900–10. https://doi.org/10.1016/j.combustflame.2014.01.010.

[301] Jovanovic R, Milewska A, Swiatkowski B, Goanta A, Spliethoff H. Sensitivity analysis of different devolatilisation models on predicting ignition point position during pulverized coal combustion in O_2/N_2 and O_2/CO_2 atmospheres. Fuel 2012;101:23–37. https://doi.org/10.1016/j.fuel.2011.02.024.

[302] Toporov D, Bocian P, Heil P, Kellermann A, Stadler H, Tschunko S, et al. Detailed investigation of a pulverized fuel swirl flame in CO_2/O_2 atmosphere. Combust Flame 2008;155:605–18. https://doi.org/10.1016/j.combustflame.2008.05.008.

[303] Farazi S, Hinrichs J, Davidovic M, Falkenstein T, Bode M, Kang S, et al. Numerical investigation of coal particle stream ignition in oxy-atmosphere. Fuel 2019;241: 477–87. https://doi.org/10.1016/j.fuel.2018.11.108.

[304] Farazi S, Attili A, Kang S, Pitsch H. Numerical study of coal particle ignition in air and oxy-atmosphere. Proc Combust Inst 2019;37:2867–74. https://doi.org/10.1016/j.proci.2018.07.002.

[305] Wan K, Wang Z, Xia J, Vervisch L, Domingo P, Lv Y, et al. Numerical study of HCl and SO_2 impact on sodium emissions in pulverized-coal flames. Fuel 2019;250: 315–26. https://doi.org/10.1016/j.fuel.2019.04.019.

[306] Kumar M, Ghoniem AF. Multiphysics Simulations of Entrained Flow Gasification. Part II: Constructing and Validating the Overall Model. Energy Fuels 2012;26: 464–79. https://doi.org/10.1021/ef2008858.

[307] Kumar M, Ghoniem AF. Multiphysics Simulations of Entrained Flow Gasification. Part I: Validating the Nonreacting Flow Solver and the Particle Turbulent Dispersion Model. Energy Fuels 2012;26:451–63. https://doi.org/10.1021/ef200884j.

[308] Zhang C. Numerical Modeling of Coal Gasification in an Entrained-Flow Gasifier. Vol. 6 Energy, Parts A B. American Society of Mechanical Engineers; 2012. p. 1193–203. https://doi.org/10.1115/IMECE2012-88481.

[309] Tufano GL, Stein OT, Kronenburg A, Gentile G, Stagni A, Frassoldati A, et al. Fully-resolved simulations of coal particle combustion using a detailed multi-step approach for heterogeneous kinetics. Fuel 2019;240:75–83. https://doi.org/10.1016/j.fuel.2018.11.139.

[310] Smith PJ, Smoot LD, Hill SC, Eaton AM. Detailed model for practical pulverized coal furnaces and gasifiers. Volume II. United States: 1991.

[311] Niksa S, Lau C. Global rates of devolatilization for various coal types. Combust Flame 1993;94:293–307. https://doi.org/10.1016/0010-2180(93)90075-E.

[312] Rabaçal M, Franchetti BM, Marincola FC, Proch F, Costa M, Hasse C, et al. Large Eddy Simulation of coal combustion in a large-scale laboratory furnace. Proc Combust Inst 2015;35:3609–17. https://doi.org/10.1016/j.proci.2014.06.023.

[313] Messig D, Vascellari M, Hasse C. Flame structure analysis and flamelet progress variable modelling of strained coal flames. Combust Theory Model 2017;21: 700–21. https://doi.org/10.1080/13647830.2017.1290279.

[314] Tufano GL, Stein OT, Wang B, Kronenburg A, Rieth M, Kempf AM. Coal particle volatile combustion and flame interaction. Part II: Effects of particle Reynolds number and turbulence. Fuel 2018;234:723–31. https://doi.org/10.1016/j.fuel.2018.07.054.

[315] Tufano GL, Stein OT, Wang B, Kronenburg A, Rieth M, Kempf AM. Coal particle volatile combustion and flame interaction. Part I: Characterization of transient and group effects. Fuel 2018;229:262–9. https://doi.org/10.1016/j.fuel.2018.02.105.

[316] Richter A, Vascellari M, Nikrityuk PA, Hasse C. Detailed analysis of reacting particles in an entrained-flow gasifier. Fuel Process Technol 2016;144:95–108. https://doi.org/10.1016/j.fuproc.2015.12.014.

[317] Perone CS. Pyevolve: a Python Open-source Framework for Genetic Algorithms. SIGEVOlution 2009;4:12–20. https://doi.org/10.1145/1656395.1656397.

[318] Hashimoto N, Kurose R, Shirai H. Numerical simulation of pulverized coal jet flame employing the TDP model. Fuel 2012;97:277–87. https://doi.org/10.1016/j.fuel.2012.03.005.

[319] Van Essendelft D, Li T, Nicoletti P, Jordan T. Advanced Chemistry Surrogate Model Development within C3M for CFD Modeling, Part 1: Methodology Development for Coal Pyrolysis. Ind Eng Chem Res 2014;53:7780–96. https://doi.org/10.1021/ie402678f.

[320] Li T, Chaudhari K, Vanessendelft D, Turton R, Nicoletti P, Shahnam M, et al. Computational fluid dynamic simulations of a pilot-scale transport coal gasifier: Evaluation of reaction kinetics. Energy Fuels 2013;27:7896–904. https://doi.org/10.1021/ef401887r.

[321] Hashimoto N, Kurose R, Hwang S-M, Tsuji H, Shirai H. A numerical simulation of pulverized coal combustion employing a tabulated-devolatilization-process model (TDP model). Combust Flame 2012;159:353–66. https://doi.org/10.1016/j.combustflame.2011.05.024.

[322] Takahashi H, Hashimoto N, Watanabe H, Kurose R, Fujita O. Prediction of soot formation characteristics in a pulverized-coal combustion field by large eddy simulations with the TDP model. Proc Combust Inst 2019;37:2883–91. https://doi.org/10.1016/j.proci.2018.09.019.

[323] Abbas T, Awais MM, Lockwood FC. An artificial intelligence treatment of devolatilization for pulverized coal and biomass in co-fired flames. Combust Flame 2003;132:305–18. https://doi.org/10.1016/S0010-2180(02)00482-0.

[324] Xing J, Luo K, Pitsch H, Wang H, Bai Y, Zhao C, et al. Predicting kinetic parameters for coal devolatilization by means of Artificial Neural Networks. Proc Combust Inst 2019;37:2943–50. https://doi.org/10.1016/j.proci.2018.05.148.

[325] Debiagi P, Nicolai H, Han W, Janicka J, Hasse C. Machine learning for predictive coal combustion CFD simulations—From detailed kinetics to HDMR Reduced-Order models. Fuel 2020;274:117720. https://doi.org/10.1016/j.fuel.2020.117720.

[326] Rabitz H, Aliş ÖF, Shorter J, Shim K. Efficient input-output model representations. Comput Phys Commun 1999;117:11–20. https://doi.org/10.1016/S0010-4655(98)00152-0.

[327] Brown BW, Smoot LD, Smith PJ, Hedman PO. Measurement and Prediction of Entrained-Flow Gasification Processes. AIChE J 1988;34:435–46. https://doi.org/10.1002/aic.690340311.

[328] Mularski J, Pawlak-Kruczek H, Modlinski N. A review of recent studies of the CFD modelling of coal gasification in entrained flow gasifiers, covering devolatilization, gas-phase reactions, surface reactions, models and kinetics. Fuel 2020;271:117620. https://doi.org/10.1016/j.fuel.2020.117620.

[329] Shamooni A, Debiagi P, Wang B, Luu TD, Stein OT, Kronenburg A, et al. Carrier-phase DNS of detailed NOx formation in early-stage pulverized coal combustion with fuel-bound nitrogen. Fuel 2021;291:119998. https://doi.org/10.1016/j.fuel.2020.119998.

[330] Zhao L, Cleary MJ, Stein OT, Kronenburg A. A two-phase MMC-LES model for pyrolysing solid particles in a turbulent flame. Combust Flame 2019;209:322–36. https://doi.org/10.1016/j.combustflame.2019.08.005.

[331] Cai R, Luo K, Watanabe H, Kurose R, Fan J. Recent advances in high-fidelity simulations of pulverized coal combustion. Adv Powder Technol 2020;31: 3062–79. https://doi.org/10.1016/j.apt.2020.05.001.

[332] Vascellari M, Arora R, Hasse C. Simulation of entrained flow gasification with advanced coal conversion submodels. Part 2: Char conversion. Fuel 2014;118: 369–84. https://doi.org/10.1016/j.fuel.2013.11.004.

[333] Vascellari M, Xu H, Hartl S, Hunger F, Hasse C. Flamelet/progress variable modeling of partial oxidation systems: From laboratory flames to pilot-scale reactors. Chem Eng Sci 2015;134:694–707. https://doi.org/10.1016/j.ces.2015.05.042.

[334] Smith PJ, Fletcher TH, Smoot LD. Model for pulverized coal-fired reactors. Symp Combust 1981;18:1285–93. https://doi.org/10.1016/S0082-0784(81)80132-4.

[335] Kurose R, Makino H. Large eddy simulation of a solid-fuel jet flame. Combust Flame 2003;135:1–16. https://doi.org/10.1016/S0010-2180(03)00141-X.

[336] Watanabe H, Kurose R, Komori S. Large-Eddy Simulation of Swirling Flows in a Pulverized Coal Combustion Furnace with a Complex Burner. J Environ Eng 2009; 4:1–11. https://doi.org/10.1299/jee.4.1.

[337] Kurose R, Watanabe H, Makino H. Numerical Simulations of Pulverized Coal Combustion. KONA Powder Part J 2009;27:144–56. https://doi.org/10.14356/kona.2009014.

[338] Yamamoto K, Murota T, Okazaki T, Taniguchi M. Large eddy simulation of a pulverized coal jet flame ignited by a preheated gas flow. Proc Combust Inst 2011; 33:1771–8. https://doi.org/10.1016/j.proci.2010.05.113.

[339] Franchetti BM, Cavallo Marincola F, Navarro-Martinez S, Kempf AM. Large Eddy simulation of a pulverised coal jet flame. Proc Combust Inst 2013;34:2419–26. https://doi.org/10.1016/j.proci.2012.07.056.

[340] Magnussen BF, Hjertager BH. On mathematical modeling of turbulent combustion with special emphasis on soot formation and combustion. Symp Combust 1977; 16:719–29. https://doi.org/10.1016/S0082-0784(77)80366-4.

[341] Wen X, Jin H, Stein OT, Fan J, Luo K. Large Eddy Simulation of piloted pulverized coal combustion using the velocity-scalar joint filtered density function model. Fuel 2015;158:494–502. https://doi.org/10.1016/j.fuel.2015.05.045.

[342] Wen X, Jin H, Sun K, Fan J. Numerical investigation of droplet evaporation and transport in a turbulent spray with LES/VSJFDF model. Chem Eng Sci 2014;119: 251–60. https://doi.org/10.1016/j.ces.2014.08.038.

[343] Stein OT, Olenik G, Kronenburg A, Cavallo Marincola F, Franchetti BM, Kempf AM, et al. Towards Comprehensive Coal Combustion Modelling for LES. Flow. Turbul Combust 2013;90:859–84. https://doi.org/10.1007/s10494-012-9423-y.

[344] Abani N, Ghoniem AF. Large eddy simulations of coal gasification in an entrained flow gasifier. Fuel 2013;104:664–80. https://doi.org/10.1016/j.fuel.2012.06.006.

[345] Zhang M, Yu J, Xu X. A new flame sheet model to reflect the influence of the oxidation of CO on the combustion of a carbon particle. Combust Flame 2005; 143:150–8. https://doi.org/10.1016/j.combustflame.2005.05.010.

[346] Smith IW. The intrinsic reactivity of carbons to oxygen. Fuel 1978;57:409–14. https://doi.org/10.1016/0016-2361(78)90055-8.

[347] Luo K, Wang H, Fan J, Yi F. Direct Numerical Simulation of Pulverized Coal Combustion in a Hot Vitiated Co-flow. Energy Fuels 2012;26:6128–36. https://doi.org/10.1021/ef301253y.

[348] Muto M, Tanno K, Kurose R. A DNS study on effect of coal particle swelling due to devolatilization on pulverized coal jet flame. Fuel 2016;184:749–52. https://doi.org/10.1016/j.fuel.2016.07.070.

[349] Rieth M, Kempf AM, Kronenburg A, Stein OT. Carrier-phase DNS of pulverized coal particle ignition and volatile burning in a turbulent mixing layer. Fuel 2018; 212:364–74. https://doi.org/10.1016/j.fuel.2017.09.096.

[350] Ranzi E, Frassoldati A, Granata S, Faravelli T. Wide-Range Kinetic Modeling Study of the Pyrolysis, Partial Oxidation, and Combustion of Heavy n-Alkanes. Ind Eng Chem Res 2005;44:5170–83. https://doi.org/10.1021/ie049318g.

[351] Tufano GL, Stein OT, Kronenburg A, Frassoldati A, Faravelli T, Deng L, et al. Resolved flow simulation of pulverized coal particle devolatilization and ignition in air- and O_2/CO_2-atmospheres. Fuel 2016;186:285–92. https://doi.org/10.1016/j.fuel.2016.08.073.

[352] Rieth M, Kempf AM, Stein OT, Kronenburg A, Hasse C, Vascellari M. Evaluation of a flamelet/progress variable approach for pulverized coal combustion in a turbulent mixing layer. Proc Combust Inst 2019;37:2927–34. https://doi.org/10.1016/j.proci.2018.05.150.

[353] Pierce CD, Moin P. Progress-variable approach for large-eddy simulation of non-premixed turbulent combustion. J Fluid Mech 2004;504:73–97. https://doi.org/10.1017/S0022112004008213.

[354] Wen X, Rieth M, Scholtissek A, Stein OT, Wang H, Luo K, et al. A comprehensive study of flamelet tabulation methods for pulverized coal combustion in a turbulent mixing layer — Part I: A priori and budget analyses. Combust Flame 2020;216:439–52. https://doi.org/10.1016/j.combustflame.2019.05.046.

[355] Wen X, Rieth M, Scholtissek A, Stein OT, Wang H, Luo K, et al. A comprehensive study of flamelet tabulation methods for pulverized coal combustion in a turbulent mixing layer—Part II: Strong heat losses and multi-mode combustion. Combust Flame 2020;216:453–67. https://doi.org/10.1016/j.combustflame.2019.12.028.

[356] Turbulent Non-premixed Flames (TNF) Workshop, International Workshop on Measurement and Computation of Turbulent Flames 2020. https://tnfworkshop.org (accessed April 9, 2021).

[357] Ahn S, Tanno K, Watanabe H. Numerical analysis of particle dispersion and combustion characteristics on a piloted coaxial pulverized coal jet flame. Appl Therm Eng 2017;124:1194–202. https://doi.org/10.1016/j.applthermaleng.2017.06.103.

[358] Cai J, Handa M, Modest MF. Eulerian–Eulerian multi-fluid methods for pulverized coal flames with nongray radiation. Combust Flame 2015;162:1550–65. https://doi.org/10.1016/j.combustflame.2014.11.023.

[359] Wan K, Xia J, Wang Z, Pourkashanian M, Cen K. Large-eddy Simulation of Pilot-assisted Pulverized-coal Combustion in a Weakly Turbulent Jet. Flow. Turbul Combust 2017;99:531–50. https://doi.org/10.1007/s10494-017-9817-y.

[360] Magnussen BF. The Eddy Dissipation Concept—A Bridge Between Science and Technology. ECCOMAS Themat. Conf. Comput. Combust. 2005;21:24.

[361] Berglund M, Fedina E, Fureby C, Tegnér J, Sabel'nikov V. Finite Rate Chemistry Large-Eddy Simulation of Self-Ignition in Supersonic Combustion Ramjet. AIAA J 2010;48:540–50. https://doi.org/10.2514/1.43746.

[362] DesJardin PE, Frankel SH. Large eddy simulation of a nonpremixed reacting jet: Application and assessment of subgrid-scale combustion models. Phys Fluids 1998;10:2298–314. https://doi.org/10.1063/1.869749.

[363] Pope SB. PDF methods for turbulent reactive flows. Prog Energy Combust Sci 1985;11:119–92. https://doi.org/10.1016/0360-1285(85)90002-4.

[364] Peters N. Laminar diffusion flamelet models in non-premixed turbulent combustion. Prog Energy Combust Sci 1984;10:319–39. https://doi.org/10.1016/0360-1285(84)90114-X.

[365] Klimenko AY, Bilger RW. Conditional moment closure for turbulent combustion. Prog Energy Combust Sci 1999;25:595–687. https://doi.org/10.1016/S0360-1285(99)00006-4.

[366] Zhou L, Hu L, Wang F. Large-eddy simulation of turbulent combustion using different combustion models. Fuel 2008;87:3123–31. https://doi.org/10.1016/j.fuel.2008.04.025.

[367] Hu LY, Zhou LX, Zhang J. Large-Eddy Simulation of a Swirling Diffusion Flame Using a SOM SGS Combustion Model. Numer Heat Transf Part B Fundam 2006;50:41–58. https://doi.org/10.1080/10407790500459395.

[368] Baum MM, Street PJ. Predicting the combustion behaviour of coal particles. Combust Sci Technol 1971;3:231–43. https://doi.org/10.1080/00102207108952290.

[369] Fores DV, Fletcher TH. The Use of Two Mixture Fractions to Treat Coal Combustion Products in Turbulent Pulverized-Coal Flames. Combust Sci Technol 2000;150:1–26. https://doi.org/10.1080/00102200008952115.

[370] Vascellari M, Xu H, Hasse C. Flamelet modeling of coal particle ignition. Proc Combust Inst 2013;34:2445–52. https://doi.org/10.1016/j.proci.2012.06.152.

[371] Vascellari M, Tufano GL, Stein OT, Kronenburg A, Kempf AM, Scholtissek A, et al. A flamelet/progress variable approach for modeling coal particle ignition. Fuel 2017;201:29–38. https://doi.org/10.1016/j.fuel.2016.09.005.

[372] Xia M, Zabrodiec D, Scouflaire P, Fiorina B, Darabiha N. Experimental and numerical studies of pulverized coal devolatilization and oxidation in strained methane/air flames. Proc Combust Inst 2017;36:2123–30. https://doi.org/10.1016/j.proci.2016.07.080.

[373] Vascellari M, Messig D, Scholtissek A, Hasse C, Xia M, Fiorina B, et al. Experimental and numerical investigation of a stagnation pulverised coal flame. Proc Combust Inst 2019;37:2857–66. https://doi.org/10.1016/j.proci.2018.05.141.

[374] Watanabe J, Yamamoto K. Flamelet model for pulverized coal combustion. Proc Combust Inst 2015;35:2315–22. https://doi.org/10.1016/j.proci.2014.07.065.

[375] Watanabe J, Okazaki T, Yamamoto K, Kuramashi K, Baba A. Large-eddy simulation of pulverized coal combustion using flamelet model. Proc Combust Inst 2017;36:2155–63. https://doi.org/10.1016/j.proci.2016.06.031.

[376] Wen X, Luo K, Luo Y, Kassem HI, Jin H, Fan J. Large eddy simulation of a semi-industrial scale coal furnace using non-adiabatic three-stream flamelet/progress variable model. Appl Energy 2016;183:1086–97. https://doi.org/10.1016/j.apenergy.2016.09.034.

[377] Wen X, Luo K, Jin H, Fan J. Large eddy simulation of piloted pulverised coal combustion using extended flamelet/progress variable model. Combust Theory Model 2017;21:925–53. https://doi.org/10.1080/13647830.2017.1314552.

[378] Wen X, Luo Y, Luo K, Jin H, Fan J. LES of pulverized coal combustion with a multi-regime flamelet model. Fuel 2017;188:661–71. https://doi.org/10.1016/j.fuel.2016.10.070.

[379] Wen X, Luo K, Luo Y, Wang H, Fan J. Large-eddy simulation of multiphase combustion jet in cross-flow using flamelet model. Int J Multiph Flow 2018;108:211–25. https://doi.org/10.1016/j.ijmultiphaseflow.2018.06.017.

[380] Wen X, Luo Y, Wang H, Luo K, Jin H, Fan J. A three mixture fraction flamelet model for multi-stream laminar pulverized coal combustion. Proc Combust Inst 2019;37:2901–10. https://doi.org/10.1016/j.proci.2018.05.147.

[381] Wen X, Debiagi P, Stein OT, Kronenburg A, Kempf AM, Hasse C. Flamelet tabulation methods for solid fuel combustion with fuel-bound nitrogen. Combust Flame 2019;209:155–66. https://doi.org/10.1016/j.combustflame.2019.07.039.

[382] Wen X, Debiagi P, Hasse C. Flamelet tabulation methods for SOx formation in pulverized solid fuel combustion. Combust Flame 2020;218:150–67. https://doi.org/10.1016/j.combustflame.2020.04.025.

[383] Wen X, Wang H, Luo Y, Luo K, Fan J. Evaluation of flamelet/progress variable model for laminar pulverized coal combustion. Phys Fluids 2017;29:083607. https://doi.org/10.1063/1.4999335.

[384] Wen X, Nicolai H, Schneider H, Cai L, Janicka J, Pitsch H, et al. Flamelet LES of a swirl-stabilized multi-stream pulverized coal burner in air and oxy-fuel

[385] Becker LG, Kosaka H, Böhm B, Doost S, Knappstein R, Habermehl M, et al. Experimental investigation of flame stabilization inside the quarl of an oxyfuel swirl burner. Fuel 2017;201:124–35. https://doi.org/10.1016/j.fuel.2016.09.002.

[386] Luo K, Zhao C, Wen X, Gao Z, Bai Y, Xing J, et al. A priori study of an extended flamelet/progress variable model for NO prediction in pulverized coal flames. Energy 2019;175:768–80. https://doi.org/10.1016/j.energy.2019.03.110.

[387] Zhao C, Luo K, Cai R, Xing J, Gao Z, Fan J. Large eddy simulations and analysis of NO emission characteristics in a laboratory pulverized coal flame. Fuel 2020;279:118316. https://doi.org/10.1016/j.fuel.2020.118316.

[388] Akaotsu S, Matsushita Y, Aoki H, Malalasekera W. Analysis of flame structure using detailed chemistry and applicability of flamelet/progress variable model in the laminar counter-flow diffusion flames of pulverized coals. Adv Powder Technol 2020;31:1302–22. https://doi.org/10.1016/j.apt.2019.12.019.

[389] Knappstein R, Kuenne G, Ketelheun A, Köser J, Becker L, Heuer S, et al. Devolatilization and volatiles reaction of individual coal particles in the context of FGM tabulated chemistry. Combust Flame 2016;169:72–84. https://doi.org/10.1016/j.combustflame.2016.04.014.

[390] Knappstein R, Kuenne G, Meier T, Sadiki A, Janicka J. Evaluation of coal particle volatiles reaction by using detailed kinetics and FGM tabulated chemistry. Fuel 2017;201:39–52. https://doi.org/10.1016/j.fuel.2016.10.033.

[391] Knappstein R, Kuenne G, Becker LG, di Mare F, Sadiki A, Dreizler A, et al. Large Eddy Simulation of a Novel Gas-Assisted Coal Combustion Chamber. Flow, Turbul Combust 2018;101:895–926. https://doi.org/10.1007/s10494-018-9910-x.

[392] Knappstein R, Kuenne G, Nicolai H, di Mare F, Sadiki A, Janicka J. Description of the char conversion process in coal combustion based on premixed FGM chemistry. Fuel 2019;236:124–34. https://doi.org/10.1016/j.fuel.2018.08.158.

[393] van Oijen JA, Donini A, Bastiaans RJM, ten Thije Boonkkamp JHM, de Goey LPH. State-of-the-art in premixed combustion modeling using flamelet generated manifolds. Prog Energy Combust Sci 2016;57:30–74. https://doi.org/10.1016/j.pecs.2016.07.001.

[394] Nicolai H, Kuenne G, Knappstein R, Schneider H, Becker LGG, Hasse C, et al. Large Eddy Simulation of a laboratory-scale gas-assisted pulverized coal combustion chamber under oxy-fuel atmospheres using tabulated chemistry. Fuel 2020;272:117683. https://doi.org/10.1016/j.fuel.2020.117683.

[395] Nicolai H, Li T, Geschwindner C, di Mare F, Hasse C, Boehm B, et al. Numerical investigation of pulverized coal particle group combustion using tabulated chemistry. Proc Combust Inst 2020. https://doi.org/10.1016/j.proci.2020.06.081.

[396] Kurose R, Makino H, Suzuki A. Numerical analysis of pulverized coal combustion characteristics using advanced low-NOx burner. Fuel 2004;83:693–703. https://doi.org/10.1016/j.fuel.2003.07.003.

[397] De Soete GG. Overall reaction rates of NO and N_2 formation from fuel nitrogen. Symp Combust 1975;15:1093–102. https://doi.org/10.1016/S0082-0784(75)80374-2.

[398] Levy JM, Chan LK, Sarofim AF, Beér JM. NO/char reactions at pulverized coal flame conditions. Symp Combust 1981;18:111–20. https://doi.org/10.1016/S0082-0784(81)80016-1.

[399] Muto M, Watanabe H, Kurose R, Komori S, Balusamy S, Hochgreb S. Large-eddy simulation of pulverized coal jet flame – Effect of oxygen concentration on NOx formation. Fuel 2015;142:152–63. https://doi.org/10.1016/j.fuel.2014.10.069.

[400] Hashimoto N, Watanabe H, Kurose R, Shirai H. Effect of different fuel NO models on the prediction of NO formation/reduction characteristics in a pulverized coal combustion field. Energy 2017;118:47–59. https://doi.org/10.1016/j.energy.2016.12.003.

[401] Hashimoto N, Shirai H. Numerical simulation of sub-bituminous coal and bituminous coal mixed combustion employing tabulated-devolatilization-process model. Energy 2014;71:399–413. https://doi.org/10.1016/j.energy.2014.04.091.

[402] Field MA. Rate of combustion of size-graded fractions of char from a low-rank coal between 1 200°K and 2 000°K. Combust Flame 1969;13:237–52. https://doi.org/10.1016/0010-2180(69)90002-9.

[403] Chen W, Smoot LD, Fletcher TH, Boardman RD. A Computational Method for Determining Global Fuel-NO Rate Expressions. Part 1. Energy Fuels 1996;10:1036–45. https://doi.org/10.1021/ef950169b.

[404] Muto M, Watanabe H, Kurose R. Large eddy simulation of pulverized coal combustion in multi-burner system–effect of in-furnace blending method on NO emission. Adv Powder Technol 2019;30:3153–62. https://doi.org/10.1016/j.apt.2019.09.024.

[405] Muto M, Yuasa K, Kurose R. Numerical simulation of ignition in pulverized coal combustion with detailed chemical reaction mechanism. Fuel 2017;190:136–44. https://doi.org/10.1016/j.fuel.2016.11.029.

[406] Wen X, Shamooni A, Stein OT, Cai L, Kronenburg A, Pitsch H, et al. Detailed analysis of early-stage NO formation in turbulent pulverized coal combustion with fuel-bound nitrogen. Proc Combust Inst 2020;38. https://doi.org/10.1016/j.proci.2020.06.317.

[407] min Hwang S, R Kurose, Akamatsu F, Tsuji H, Makino H, Katsuki M. Application of Optical Diagnostics Techniques to a Laboratory-Scale Turbulent Pulverized Coal Flame. Energy Fuels 2005;19:382–92. https://doi.org/10.1021/ef049867z.

[408] Weber R, Dugue J, Sayre A, Peters AAF, Visser BM. Measurements and computations of quarl zone flow field and chemistry in a swirling pulverized coal flame. IFRF Doc F 1992;36.

[409] Akaotsu S, Matsushita Y, Aoki H, Malalasekera W. Application of flamelet/progress-variable approach to the large eddy simulation of a turbulent jet flame of

pulverized coals. Adv Powder Technol 2020;31:4253–74. https://doi.org/10.1016/j.apt.2020.09.005.

[410] Coal and Biomass Conversion (CBC) Workshop 2020. http://www.cbc.uni-due.de/?file=workshop.

[411] Molina A, Shaddix CR. Ignition and devolatilization of pulverized bituminous coal particles during oxygen/carbon dioxide coal combustion. Proc Combust Inst 2007;31:1905–12. https://doi.org/10.1016/j.proci.2006.08.102.

[412] Shaddix CR, Molina A. Particle imaging of ignition and devolatilization of pulverized coal during oxy-fuel combustion. Proc Combust Inst 2009;32:2091–8. https://doi.org/10.1016/j.proci.2008.06.157.

[413] Zhang W, Tainaka K, Ahn S, Watanabe H, Kitagawa T. Experimental and numerical investigation of effects of particle shape and size distribution on particles' dispersion in a coaxial jet flow. Adv Powder Technol 2018;29:2322–30. https://doi.org/10.1016/j.apt.2018.06.008.

[414] Ahn S, Tainaka K, Watanabe H, Kitagawa T. Experimental and numerical analysis of turbulent pulverized coal flame in a coaxial burner. Energy 2019;179:727–35. https://doi.org/10.1016/j.energy.2019.04.190.

[415] Balusamy S, Schmidt A, Hochgreb S. Flow field measurements of pulverized coal combustion using optical diagnostic techniques. Exp Fluids 2013;54:1534. https://doi.org/10.1007/s00348-013-1534-2.

[416] Balusamy S, Kamal MM, Lowe SM, Tian B, Gao Y, Hochgreb S. Laser diagnostics of pulverized coal combustion in O_2/N_2 and O_2/CO_2 conditions: velocity and scalar field measurements. Exp Fluids 2015;56:108. https://doi.org/10.1007/s00348-015-1965-z.

[417] Cleary M, Stein O, Kronenburg A, Bilger B. Modeling of Sandia single particle case. 1st Work. Coal Biomass Convers 2015:58–62. Avignon, France.

[418] Smith GP, Golden DM, Frenklach M, Moriarty NW, Eiteneer B, Goldenberg M, et al. GRI-Mech 3.0 n.d. http://combustion.berkeley.edu/gri-mech/version30/text30.html (accessed August 13, 2020).

[419] Schiemann M, Wirtz S, Scherer V. Optical measurement of pulverized coal combustion in a laminar flow reactor: ignition, particle temperature, and alkali release. In: Proc. 10th ICCEU - Int. Conf. Combust. Energy Util.; 2010. p. 23–30.

[420] Köser J, Becker LG, Goßmann AK, Böhm B, Dreizler A. Investigation of ignition and volatile combustion of single coal particles within oxygen-enriched atmospheres using high-speed OH-PLIF. Proc Combust Inst 2017;36:2103–11. https://doi.org/10.1016/j.proci.2016.07.083.

[421] Köser J, Li T, Vorobiev N, Dreizler A, Schiemann M, Böhm B. Multi-parameter diagnostics for high-resolution in-situ measurements of single coal particle combustion. Proc Combust Inst 2019;37:2893–900. https://doi.org/10.1016/j.proci.2018.05.116.

[422] Liu Y, Geier M, Molina A, Shaddix CR. Pulverized coal stream ignition delay under conventional and oxy-fuel combustion conditions. Int J Greenh Gas Control 2011;5:S36–46. https://doi.org/10.1016/j.ijggc.2011.05.028.

[423] Li T, Geschwindner C, Köser J, Schiemann M, Dreizler A, Böhm B. Investigation of the transition from single to group coal particle combustion using high-speed scanning OH-LIF and diffuse backlight-illumination. Proc Combust Inst 2020;38:4101–9. https://doi.org/10.1016/j.proci.2020.06.314.

[424] Essenhigh RH, Misra MK, Shaw DW. Ignition of coal particles: A review. Combust Flame 1989;77:3–30. https://doi.org/10.1016/0010-2180(89)90101-6.

[425] Xu Y, Li S, Gao Q, Yao Q, Liu J. Characterization on Ignition and Volatile Combustion of Dispersed Coal Particle Streams: In Situ Diagnostics and Transient Modeling. Energy Fuels 2018;32:9850–8. https://doi.org/10.1021/acs.energyfuels.8b01322.

[426] Yuan Y, Li S, Li G, Wu N, Yao Q. The transition of heterogeneous–homogeneous ignitions of dispersed coal particle streams. Combust Flame 2014;161:2458–68. https://doi.org/10.1016/j.combustflame.2014.03.008.

[427] Hayashi J, Hashimoto N, Nakatsuka N, Tsuji H, Watanabe H, Makino H, et al. Soot formation characteristics in a lab-scale turbulent pulverized coal flame with simultaneous planar measurements of laser induced incandescence of soot and Mie scattering of pulverized coal. Proc Combust Inst 2013;34:2435–43. https://doi.org/10.1016/j.proci.2012.10.002.

[428] Xu K, Wu Y, Shen H, Zhang Q, Zhang H. Predictions of soot formation and its effect on the flame temperature of a pulverized coal-air turbulent jet. Fuel 2017;194:297–305. https://doi.org/10.1016/j.fuel.2017.01.032.

[429] Brown AL, Fletcher TH. Modeling Soot Derived from Pulverized Coal. Energy Fuels 1998;12:745–57. https://doi.org/10.1021/ef9702207.

[430] Chen Y, Stein OT, Kronenburg A, Xing J, Luo K, Luo KH, et al. Analysis of Gas-Assisted Pulverized Coal Combustion in Cambridge Coal Burner CCB1 Using FPV-LES. Energy Fuels 2020;34:7477–89. https://doi.org/10.1021/acs.energyfuels.0c00317.

[431] Vascellari M, Schulze S, Nikrityuk PA, Safronov D, Hasse C. Numerical Simulation of Pulverized Coal MILD Combustion Using a New Heterogeneous Combustion Submodel. Flow. Turbul Combust 2014;92:319–45. https://doi.org/10.1007/s10494-013-9467-7.

[432] Michel J-B, Payne R. Detailed measurement of long pulverized coal flames for the characterization of pollutant formation. International Flame Research Foundation; 1980.

[433] Pickett LM, Jackson RE, Tree DR. LDA Measurements in a Pulverized Coal Flame at Three Swirl Ratios. Combust Sci Technol 1999;143:79–107. https://doi.org/10.1080/00102209908924194.

[434] Ahn J, Okerlund R, Fry A, Eddings EG. Sulfur trioxide formation during oxy-coal combustion. Int J Greenh Gas Control 2011;5:S127–35. https://doi.org/10.1016/j.ijggc.2011.05.009.

[435] Becker LG, Pielsticker S, Böhm B, Kneer R, Dreizler A. Particle dynamics in a gas assisted coal combustion chamber using advanced laser diagnostics. Fuel 2020;269:117188. https://doi.org/10.1016/j.fuel.2020.117188.

[436] Sadiki A, Agrebi S, Chrigui M, Doost AS, Knappstein R, Di Mare F, et al. Analyzing the effects of turbulence and multiphase treatments on oxy-coal combustion process predictions using LES and RANS. Chem Eng Sci 2017;166:283–302. https://doi.org/10.1016/j.ces.2017.03.015.

[437] Doost AS, Ries F, Becker LG, Bürkle S, Wagner S, Ebert V, et al. Residence time calculations for complex swirling flow in a combustion chamber using large-eddy simulations. Chem Eng Sci 2016;156:97–114. https://doi.org/10.1016/j.ces.2016.09.001.

[438] Maßmeyer A, Zabrodiec D, Hees J, Kreitzberg T, Hatzfeld O, Kneer R. Flame pattern analysis for 60kWth flames under conventional air-fired and oxy-fuel conditions for two different types of coal. Fuel 2020;271:117457. https://doi.org/10.1016/j.fuel.2020.117457.

[439] Weber R, Dugué J, Sayre A, Visser BM. Quarl zone flow field and chemistry of swirling pulverized coal flames: Measurements and computation. Symp Combust 1992;24:1373–80. https://doi.org/10.1016/S0082-0784(06)80160-8.

[440] Rieth M, Proch F, Clements AG, Rabaçal M, Kempf AM. Highly resolved flamelet LES of a semi-industrial scale furnace. Proc Combust Inst 2017;36:3371–9. https://doi.org/10.1016/j.proci.2016.08.089.

[441] Xu H, Smoot LD, Tree DR, Hill SC. Prediction of Nitric Oxide Destruction by Advanced Reburning. Energy Fuels 2001;15:541–51. https://doi.org/10.1021/ef000120s.

[442] Hill SC, Smoot LD. A comprehensive three-dimensional model for simulation of combustion systems. PCGC-3. Energy & Fuels 1993;7:874–83. https://doi.org/10.1021/ef00042a025.

[443] Kent JH, Bilger RW. The prediction of turbulent diffusion flame fields and nitric oxide formation. Symp Combust 1977;16:1643–56. https://doi.org/10.1016/S0082-0784(77)80443-8.

[444] Eddings EG, McAvoy D, Coates RL. Co-firing of pulverized coal with Pinion Pine/Juniper wood in raw, torrefied and pyrolyzed forms. Fuel Process Technol 2017;161:273–82. https://doi.org/10.1016/j.fuproc.2015.11.020.

[445] Fry A, Adams B, Paschedag A, Kazalski P, Carney C, Oryshchyn D, et al. Principles for retrofitting coal burners for oxy-combustion. Int J Greenh Gas Control 2011;5:S151–8. https://doi.org/10.1016/j.ijggc.2011.05.004.

[446] Fan JR, Zha XD, Sun P, Cen KF. Simulation of ash deposit in a pulverized coal-fired boiler. Fuel 2001;80:645–54. https://doi.org/10.1016/S0016-2361(00)00134-4.

[447] Fan JR, Zha XD, Cen KF. Study on coal combustion characteristics in a W-shaped boiler furnace. Fuel 2001;80:373–81. https://doi.org/10.1016/S0016-2361(00)00098-3.

[448] Fan J, Qian L, Ma Y, Sun P, Cen K. Computational modeling of pulverized coal combustion processes in tangentially fired furnaces. Chem Eng J 2001;81:261–9. https://doi.org/10.1016/S1385-8947(00)00212-6.

[449] Asotani T, Yamashita T, Tominaga H, Uesugi Y, Itaya Y, Mori S. Prediction of ignition behavior in a tangentially fired pulverized coal boiler using CFD. Fuel 2008;87:482–90. https://doi.org/10.1016/j.fuel.2007.04.018.

[450] Hashimoto N, Watanabe H. Numerical analysis on effect of furnace scale on heat transfer mechanism of coal particles in pulverized coal combustion field. Fuel Process Technol 2016;145:20–30. https://doi.org/10.1016/j.fuproc.2016.01.024.

[451] The Carbon-Capture Multidisciplinary Simulation Center (CCMSC) at University of Utah 2019.

[452] Adamczyk WP, Isaac B, Parra-Alvarez J, Smith ST, Harris D, Thornock JN, et al. Application of LES-CFD for predicting pulverized-coal working conditions after installation of NOx control system. Energy 2018;160:693–709. https://doi.org/10.1016/j.energy.2018.07.031.

[453] Davison de St. Germain J, McCorquodale J, Parker SG, Johnson CR. Uintah: a massively parallel problem solving environment. In: Proc. Ninth Int. Symp. High-Performance Distrib. Comput., IEEE Comput. Soc; 2000. p. 33–41. https://doi.org/10.1109/HPDC.2000.868632.

[454] The Uintah software (2009) 2019.

[455] Watanabe H, Otaka M. Numerical simulation of coal gasification in entrained flow coal gasifier. Fuel 2006;85:1935–43. https://doi.org/10.1016/j.fuel.2006.02.002.

[456] Kajitani S, Hara S, Matsuda H. Gasification rate analysis of coal char with a pressurized drop tube furnace. Fuel 2002;81:539–46. https://doi.org/10.1016/S0016-2361(01)00149-1.

[457] Halama S, Spliethoff H. Reaction Kinetics of Pressurized Entrained Flow Coal Gasification: Computational Fluid Dynamics Simulation of a 5 MW Siemens Test Gasifier. J Energy Resour Technol 2016;138:42204–11. https://doi.org/10.1115/1.4032620.

[458] Higman C. Gasification. Combust. Eng. Issues Solid Fuel Syst.. Elsevier; 2008. p. 423–68. https://doi.org/10.1016/B978-0-12-373611-6.00011-2.

[459] Williams FA. Combustion theory. CRC Press; 2018.